



**HAL**  
open science

# A Large Area Micromegas TPC for Tracking at the ILC

Wenxin Wang

► **To cite this version:**

Wenxin Wang. A Large Area Micromegas TPC for Tracking at the ILC. Other [cond-mat.other].  
Université Paris Sud - Paris XI, 2013. English. NNT : 2013PA112099 . tel-00854414

**HAL Id: tel-00854414**

**<https://theses.hal.science/tel-00854414>**

Submitted on 27 Aug 2013

**HAL** is a multi-disciplinary open access archive for the deposit and dissemination of scientific research documents, whether they are published or not. The documents may come from teaching and research institutions in France or abroad, or from public or private research centers.

L'archive ouverte pluridisciplinaire **HAL**, est destinée au dépôt et à la diffusion de documents scientifiques de niveau recherche, publiés ou non, émanant des établissements d'enseignement et de recherche français ou étrangers, des laboratoires publics ou privés.

UNIVERSITE PARIS-SUD

ÉCOLE DOCTORALE : 534 MIPEGE  
Faculté des sciences d'Orsay

*DISCIPLINE : Physique des particules*

THÈSE DE DOCTORAT

soutenue le 24/06/2013

par

Wenxin WANG

<p>Etude d'un grand détecteur TPC Micromegas pour l'ILC</p>
---

**Directeur de thèse :**

Dr Paul COLAS

Chercheur, CEA-Saclay

**Composition du jury :**

*Président du jury :*

Prof. Patrick PUZO

Professeur, Université Paris Sud, Orsay

*Rapporteurs :*

Dr Didier CONTARDO

Chercheur, IPN Lyon, Université Claude Bernard

Dr Gilles DE LENTDECKER

Chercheur, Université Libre de Bruxelles

*Examineurs :*

Dr Jan TIMMERMANS

Chercheur, NIKHEF

Dr Didier VILANOVA

Chercheur, CEA-Saclay



University Paris-Sud  
*Graduate School 534 MIPEGE*  
Faculty of Sciences of Orsay

**THESIS** presented by :

**Wenxin WANG**

Defended on : **24 June 2013**

to obtain the degree of : **Doctor of the University Paris-Sud**

Specialty : Particle Physics

**A Large Area Micromegas TPC for  
Tracking at the ILC**

**SUPERVISOR :**

**Dr COLAS Paul**

Researcher, CEA-Saclay

**REVIEWERS :**

**Dr CONTARDO Didier**

Researcher, IPN Lyon, Université Claude Bernard

**Dr DE LENTDECKER Gilles**

Researcher, Université Libre de Bruxelles

---

**EXAMINERS :**

**Prof. PUZO Patrick**

Professor, Université Paris Sud, Orsay

**Dr TIMMERMANS Jan**

Researcher, NIKHEF

**Dr VILANOVA Didier**

Researcher, CEA-Saclay



To my parents

A mes parents

致我的父母



## Acknowledgements

It's hard to express how grateful I am just in a few words. These years in France will remain permanently in my memory. I have been so lucky to work in this wonderful group with so great people.

Firstly, I would like to thank my PhD supervisor, Dr Paul COLAS, who is always so kind and so patient to give me the guidance and advice, provide me so good chance to really see the world of experimental physics. I also would like to thank David ATTIE who provided me a lot of help during my research. He is so smart person. Each time, when I discussed with him, I made a big step in my work. Thanks to the electronics group, they did very beautiful job and provided very good electronics so that my experiment was going so smoothly. I also thank Marc RIALLOT and other people who work at SEDI. When I met problems and my colleagues of my group were not around, they always gave me unconditional help.

I also would like to thank Ursula BASSLER, leader of the Irfu particle physics division, for her welcome at SPP, and Georges VASSEUR, my godfather, for his support.

My thanks go also to Didier CONTARDO, Gilles DE LENTDECKER, Patrick PUZO, Jan TIMMERMANS, and Didier VILANOVA for accepting to judge this thesis.

Outside my institute, I thank all the people who are working in our collaboration: Madhu DIXIT, Keisuke FUJII, and the students who were working with them, as well as the DESY group.

Thanks very much to the people who gave me tremendous help for my French. I'm not good at learning foreign languages. They were so patient to speak with me. Also, I would like to thank my Chinese friends. They gave me a lot of help.

Without you all, it would have been hard for me to live in France, to complete my PhD work. I really appreciate all your help for the last years.





# Résumé

Une grande ‘Chambre à Projection Temporelle’ (TPC) est un candidat pour la détection et la mesure des traces chargées auprès de l’ILC, collisionneur linéaire d’électrons et de positons de 31 km permettant d’atteindre des énergies dans le centre de masse de 250 GeV à 1 TeV. Le travail de R&D décrit dans cette thèse porte sur un type nouveau de TPC, dont la lecture est assurée par des Micromégas à anode résistive. Ce dispositif permet de répartir le signal électrique sur plusieurs carreaux, même lorsque la charge est déposée sur un seul carreau. Il permet aussi de protéger l’électronique, ce qui est utilisé dans notre prototype pour miniaturiser les cartes de lecture.

Dans ce travail, des modules Micromégas ont été testés et caractérisés, dans un premier temps, en faisceau, un par un au centre de la chambre, puis 7 modules montés en même temps de façon à couvrir la surface. Egalement, des tests sur un banc équipé d’une source de  $^{55}\text{Fe}$  ont permis de caractériser les 7 modules utilisés. Une résolution en position de 60 microns par ligne de carreaux est obtenue à petite distance de dérive. L’uniformité est aussi évaluée, et des distorsions pouvant atteindre environ 500 microns sont observées.

L’ensemble des résultats démontre l’adéquation de ce type de lecture à la TPC pour l’ILC.

La fraction de retour des ions est également mesurée à l’aide d’un détecteur de même géométrie et avec le même gaz que ceux utilisés dans ces tests, et la loi en rapport inverse des champs est validée à nouveau dans ces conditions.

La même technique est appliquée à la réalisation d’un imageur neutron, consistant en une TPC Micromégas ‘plate’ précédée d’un film convertisseur de 1mm d’épaisseur. Les protons éjectés par les neutrons sont ‘suivis à la trace’ dans le volume gazeux, ce qui permet de reconstruire avec une précision meilleure que le millimètre le point d’origine du neutron.

*Mots-clés : trajectographie, lecture à anode résistive, Micromégas, Chambre à Projection Temporelle (TPC)*



# Résumé de thèse

L'étude des composants fondamentaux de la matière nécessite des accélérateurs toujours de plus en plus puissants. De nouvelles particules sont produites dans les collisions à haute énergie de protons ou d'électrons. Les produits de ces collisions sont détectés dans de grands appareillages entourant le point d'interaction. La particule de Higgs de 125 GeV découverte au LHC sera étudiée en détails au futur collisionneur  $e^+e^-$ . Le projet phare dans ce domaine est appelé ILC, pour 'Collisionneur Linéaire International'. L'équipe que j'ai rejointe à Saclay travaille depuis une douzaine d'années sur un projet de grande 'Chambre à Projection Temporelle' (TPC) pour détecter les traces chargées à l'aide de l'ionisation qu'elles laissent dans un volume de gaz. Cette TPC d'un type nouveau est adaptée à l'utilisation dans les conditions de l'ILC. Les électrons d'ionisation dérivent aux deux extrémités de la chambre sous l'action d'un champ électrique. Ils sont multipliés par un dispositif Micromegas, équipé d'une anode à étalement de charge faite d'un revêtement résistif-capacitif.

Le collisionneur ILC est une machine constituée de deux accélérateurs linéaires face-à-face, d'une longueur totale de 31 km. Les éléments accélérateurs sont des cavités supraconductrices. Un grand anneau d'amortissement situé au milieu est partagé entre les électrons et les positons.

Depuis la découverte d'une particule de 125 GeV au LHC, annoncée le 4 juillet dernier, et qui vérifie, à la précision actuelle des mesures, toutes les propriétés attendues d'un boson de Higgs, la nécessité de l'étudier d'une façon plus propre et plus indépendante du modèle se fait sentir. Le processus de Bjorken (aussi appelé Higgs-strahlung, voir Fig. 1-3 produira des Higgs avec une section efficace de 250 fb (Fig. 1.1). La signature du recul du Z, se désintégrant en paire de muons permettra de sélectionner les candidats Higgs quelque soit son mode de désintégration, et aussi de mesurer précisément sa masse et ses rapports d'embranchement, et ainsi de remonter à ses différents couplages. La TPC joue un rôle important dans cette analyse et permet de mesurer précisément les particules chargées et de les associer précisément avec des objets calorimétriques, ce qui est essentiel à la mise en œuvre de l'algorithme du « flux de particules », qui consiste à faire un bilan précis du contenu en énergie-impulsion des objets reconstruits dans le détecteur, en évitant tout double-comptage.

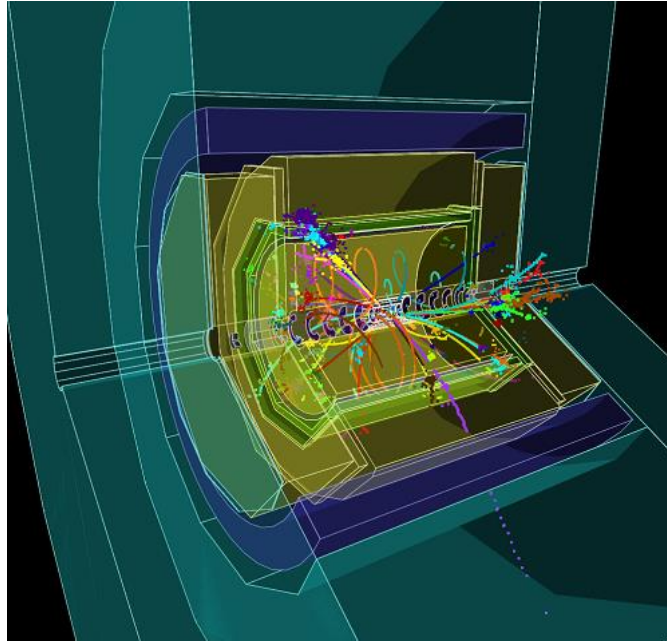
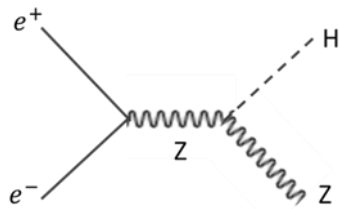


Figure R-1. A gauche, diagramme de Feynman du processus de Higgs-strahlung; à droite, événement simulé de top-antitop multijet.

Les principales propriétés des TPC sont rappelées dans le chapitre 2. Les processus de dérive et de diffusion des électrons sont étudiés, en présence d'un champ magnétique. L'amplification gazeuse et, en particulier, le cas de Micromégas sont traités. Le processus de production de la version 'bulk' (tout-en-un) de ce détecteur par méthode photo-lithographique est décrit. Une section est réservée à la présentation de la technique d'anode résistive, propre à notre application : la taille typique d'une avalanche n'excédant pas 15 à 20 microns, le signal n'est généralement pas partagé sur des damiers de 2 à 3 mm de large. L'ajout d'une couverture résistive au-dessus des pads, séparée de ceux-ci par une couche diélectrique, résulte en un réseau résistif-capacitif continu. Toute charge ponctuelle déposée sur la surface s'étale. La densité de charge suit l'équation de diffusion à deux dimensions (2-0-20), dont la solution est une gaussienne à deux dimension dont le rayon croît comme la racine carrée du temps. La valeur de la constante de temps RC par unité de surface doit être ajustée pour obtenir l'étalement optimum : deux ou trois pads sur la durée typique des signaux détectés.

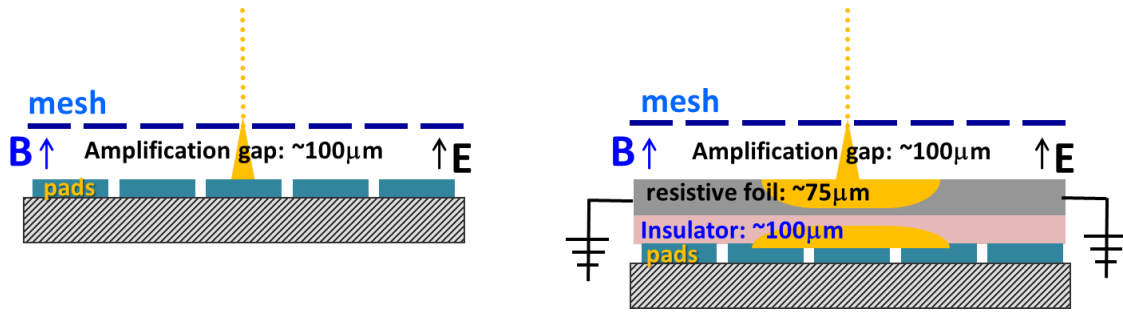


Figure R-2. A gauche, Micromegas à anode conventionnelle, le signal est sur un seul carreau; à droite, le revêtement résistif-capacitif étale la charge sur plusieurs carreaux.

Le chapitre 3 décrit l'appareillage utilisé lors des tests en faisceaux. Après une présentation de la collaboration LCTPC et du Grand Prototype construit par le consortium EUDET, je décris les modules mis au point dans notre groupe et l'électronique de lecture AFTER conçue à Saclay. Dans ce même chapitre la détermination des piédestaux et leur soustraction en ligne sont présentés. Les piédestaux et leur écart quadratique moyen sont calculés sur la base de quelques centaines d'événements déclenchés aléatoirement. Le piédestal est soustrait et seuls les signaux supérieurs à quatre écarts standard sont conservés (les autres sont mis à zéro). Ceci permet de diminuer notablement l'espace disque occupé par les données.

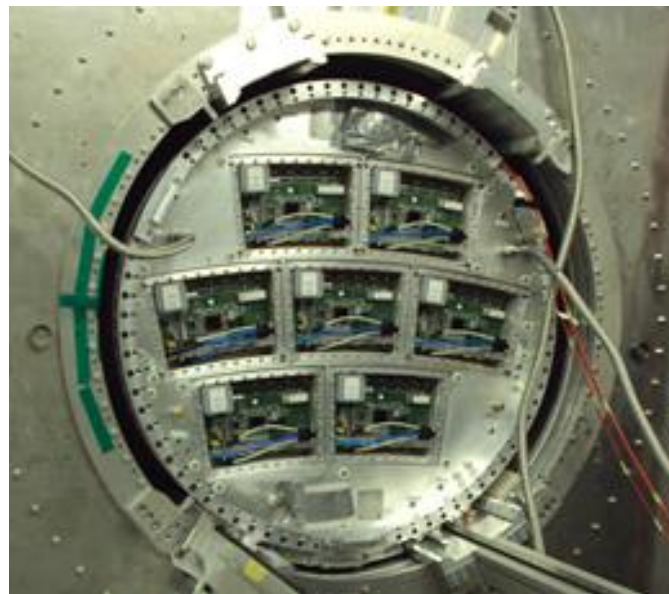


Figure R-3. Photographie du prototype 7 modules dans son aimant.

Pour rendre possible l'intégration du détecteur final, une miniaturisation de l'électronique s'est avérée nécessaire. Les puces AFTER ont été directement câblées sur des cartes reliées au détecteur par des connecteurs 300 points, et tous les composants visant à la protection de l'électronique ont été retirés, cette fonction étant assurée par la couche résistive. Pour terminer ce chapitre, le passage du prototype à la TPC finale est traité.

Dans le chapitre 4, le banc de test installé au CERN est décrit. Ce banc de test a été utilisé pour caractériser et tester tous les modules après fabrication. Des statistiques sur le gain et la résolution sont obtenues à partir de données obtenues avec source de  $^{55}\text{Fe}$  pour 7 modules. Pour cette mesure, le bruit électronique a été considérablement réduit par l'introduction d'un filtre en T (filtre passe-haut) sur l'alimentation de la grille.

La résolution (12 à 13% r.m.s.) et le gain (2640 avec un étalement de 15%) sont assez homogènes pour les 7 modules. Cette mesure de gain est en accord avec celle obtenue à l'aide des électrons du faisceau.

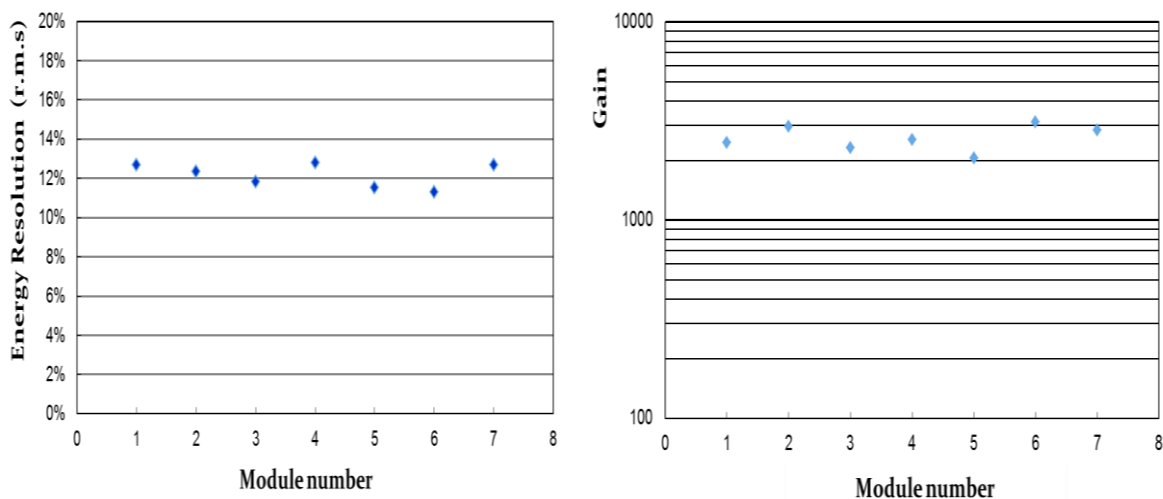


Figure R-4. Résolution en énergie et gain mesurés sur le banc de test pour chacun des 7 modules.

Le problème du retour des ions est récurrent dans les TPC. Dans les TPC conventionnelles, à fils, 20 à 30% des ions créés près des fils remontent en direction de l'espace de dérive. Les ions dérivant beaucoup plus lentement que les électrons et en sens inverse, il en résulte l'accumulation d'une charge d'espace dans la zone de dérive, susceptible de dévier les électrons d'ionisation au cours de leur dérive et donc d'introduire des distorsions. Des

mesures ont été effectuées il y a une dizaine d'années dans le groupe Micromégas, accompagnée d'une explication théorique du phénomène, et ces mesures concluaient à une suppression du retour des ions d'un facteur proportionnel au rapport des champs (amplification / dérive). Ces études avaient été faites avec des Micromegas standard (50 microns d'épaisseur de gaz) alimentées en mélange Ar+10% CH<sub>4</sub>. J'ai réitéré ces mesures avec des bulk standards de 128 microns et du gaz T2K, à l'aide d'un canon à rayons x. J'ai bien retrouvé la dépendance attendue en rapport inverse des champs. J'ai également mesuré l'efficacité de collection (signal en fonction du rapport des champs) et étudié la dépendance de la résolution sur l'énergie en fonction de ce rapport des champs à gain constant.

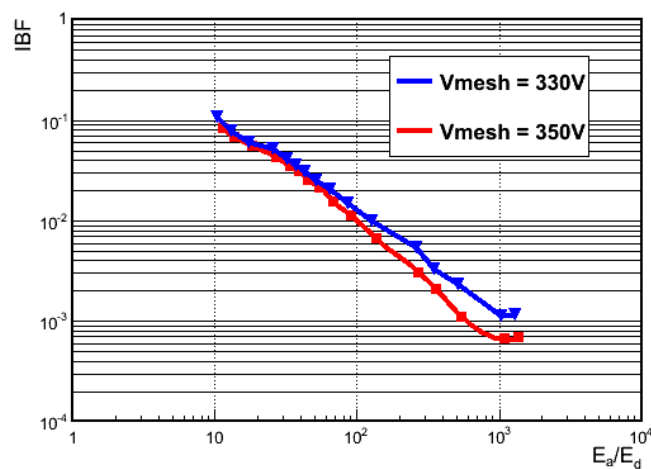


Figure R-5. La fraction de retour des ions en fonction du rapport du champ d'amplification au champ de dérive.

Dans le chapitre 6, le logiciel d'analyse est décrit en détails. La fonction de réponse des pads est définie: fraction du signal présente sur un carreau de lecture en fonction de la distance du centre de ce carreau de lecture à la trace. Cette distribution est paramétrée, puis ajustée sur des données dans un processus itératif (la trace s'améliore au cours des itérations). Principalement deux paramétrages ont été utilisés : une à quatre paramètres (rapport de deux polynômes d'ordre 4, et une à deux paramètres, combinaison d'une gaussienne et d'une lorentzienne. La deuxième permet une convergence beaucoup plus rapide de l'ajustement des paramètres. Pour déterminer la résolution et se débarrasser d'éventuels effets d'inhomogénéité de la couche résistive-capacitive, le biais (valeur moyenne des résidus) est corrigé au cours de ces itérations, et la trace ré-ajustée.



La géométrie du détecteur, très importante pour l'étude des distorsions, est décrite ainsi que son implémentation. Les carreaux d'une même rangée sont associés entre eux s'ils sont contigus, pour former un hit. La méthode de reconstruction, basée sur le filtre de Kalman, consiste à tenter d'associer des hits voisins en ensembles continus pour former des traces. Un critère de variation de  $\chi^2$  est utilisé pour accepter ou rejeter un nouveau hit dans une trace. L'association de nouveaux hits se fait d'abord de l'intérieur vers l'extérieur, puis un second passage, de l'extérieur vers l'intérieur, permet d'associer les hits non utilisés. La description détaillée de l'algorithme est effectuée en appendice. Dans l'état actuel de l'algorithme, toutes les rangées sont affectées de la même incertitude dans le calcul du  $\chi^2$ . Cependant, si un hit est très loin de la trace (c'est le cas pour les électrons delta, émis perpendiculairement à la trace, ou, plus rarement, pour les carreaux bruyants) ce point est affecté d'une grande erreur pour qu'il ne tire pas la trace vers lui. Ceci est illustré au chapitre 7 consacré à la présentation des résultats des tests en faisceaux.

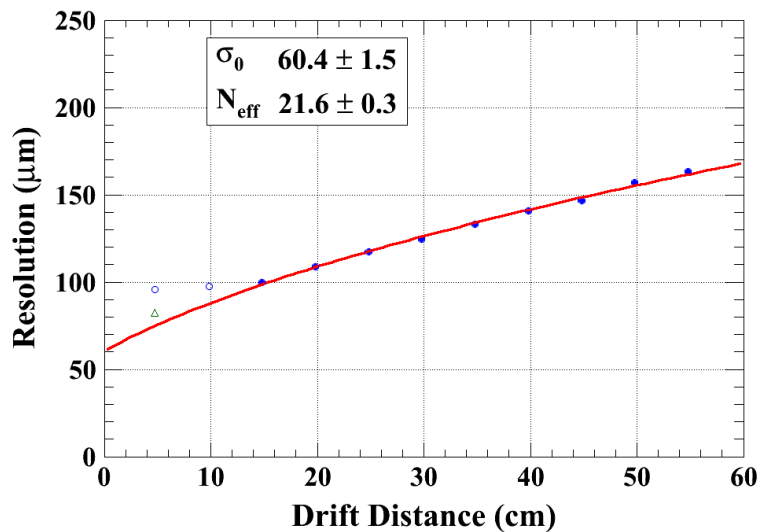


Figure R-6. Résolution moyenne des 22 lignes centrales en fonction de la distance de dérive. La courbe rouge est un ajustement de la fonction 7-0-2. Les points ouverts ne sont pas pris dans l'ajustement.

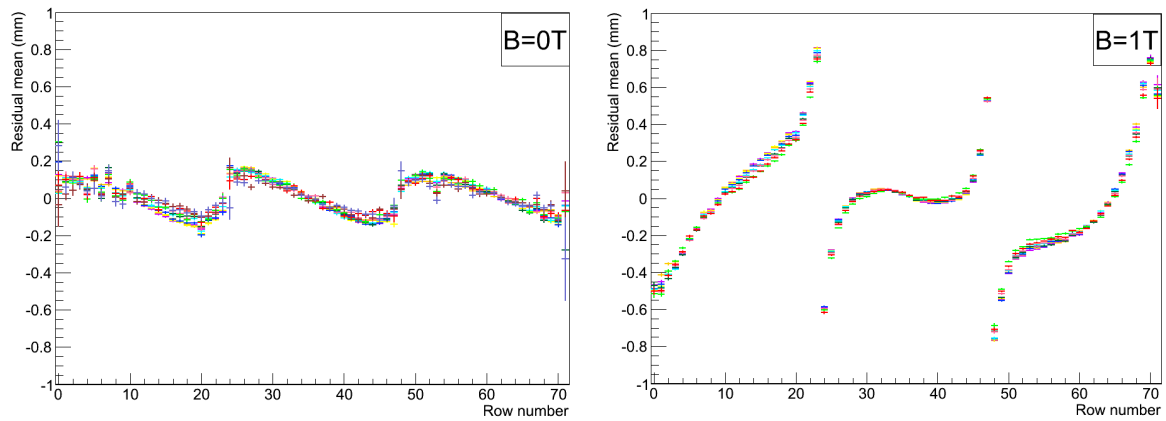


Figure R-7. Valeur moyenne des résidus en fonction du numéro de ligne, dans les cas sans et avec champ magnétique.

La résolution est ainsi déterminée en fonction de la distance de dérive. La résolution à distance zéro est de 60 microns, ce qui est un record pour des carreaux de 3mm de large. La comparaison ligne par ligne de cette résolution montre qu'elle est très uniforme, à part les lignes extrêmes (bords haut et bas des modules) pour lesquelles elle est de 50% au-dessus de la moyenne.

L'étude des résidus moyens pour des traces qui traversent trois modules mettent en évidence des distorsions pouvant atteindre 700 microns.

Le chapitre 8 est consacré au test d'un nouveau type d'imageur neutron, consistant en une TPC Micromégas 'plate'. Un film de polyéthylène de 1mm d'épaisseur est utilisé comme convertisseur, et les protons éjectés par les neutrons sont 'suivis à la trace' dans le volume gazeux, ce qui permet de reconstruire avec une précision meilleure que le millimètre le point d'origine du neutron. Nous avons testé ce détecteur en Chine, avec l'équipe du Professeur Xiaodong Zhang, de l'Université de Lanzhou.

Quelques images obtenues avec un filtre de polyéthylène gravé sont montrées, et l'amélioration de la résolution avec l'extrapolation de la trace est clairement visible.

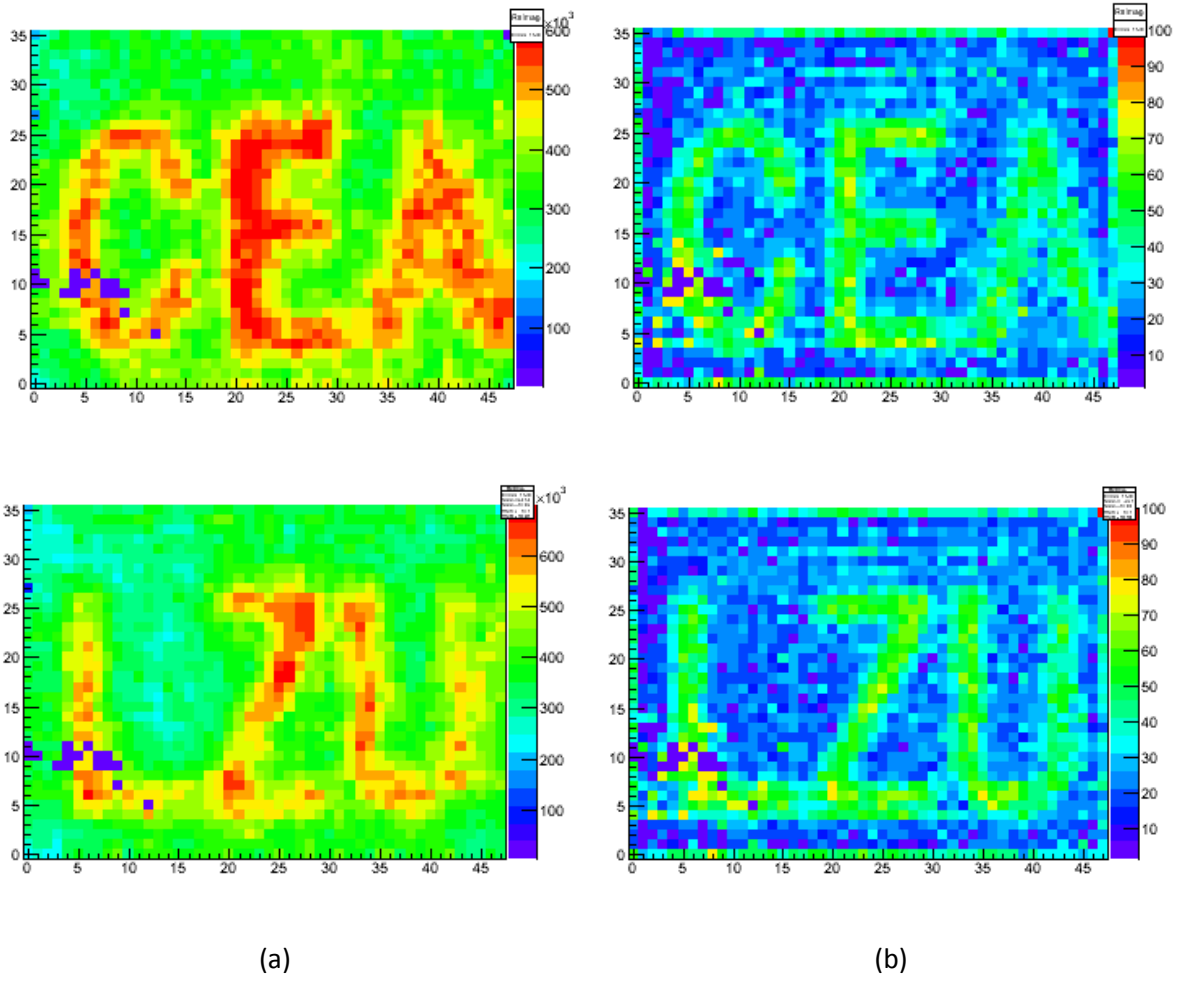


Figure R-8. Image obtenue par neutrons à travers un filtre de polyéthylène, sans et avec la coupure en temps maximum.

# Summary

The study of the fundamental building blocks of matter necessitates always more powerful accelerators. New particles are produced in high energy collisions of protons or electrons. The by-products of these collisions are detected in large apparatus surrounding the interaction point. The 125 GeV Higgs particle discovered at LHC will be studied in detail in the next  $e^+e^-$  collider. The leading project for this is called ILC. The team that I joined is working on the R&D for a Time Projection Chamber (TPC) to detect the charged tracks by the ionization they leave in a gas volume, optimised for use at ILC. This primary ionization is amplified by the so-called Micromegas device, with a charge-sharing anode made of a resistive-capacitive coating.

After a presentation of the physics motivation for the ILC and ILD detector, I will review the principle of operation of a TPC (Chapter 2) and underline the advantages of the Micromegas readout with charge sharing. The main part of this PhD work concerns the detailed study of up to 12 prototypes of various kinds. The modules and their readout electronics are described in Chapter 3. A test-bench setup has been assembled at CERN (Chapter 4) to study the response to a  $^{55}\text{Fe}$  source, allowing an energy calibration and a uniformity study. In Chapter 5, the ion backflow is studied using a bulk Micromegas and the gas gain is measured using a calibrated electronics chain. With the same setup, the electron transparency is measured as a function of the field ratio (drift/amplification).

Also, several beam tests have been carried out at DESY with a 5 GeV electron beam in a 1 T superconducting magnet. These beam tests allowed the detailed study of the spatial resolution. In the final test, the endplate was equipped with seven modules, bringing sensitivity to misalignment and distortions. Such a study required software developments (Chapter 6) to make optimal use of the charge sharing and to reconstruct multiple tracks through several modules with a Kalman Filter algorithm. The results of these studies are given in Chapter 7.

The TPC technique has been applied to neutron imaging in collaboration with the University of Lanzhou. A test using a neutron source has been carried out in China. The results are reported in Chapter 8.

*keywords: tracking, readout, resistive anode, Micromegas, Time Projection Chamber*



# Contents

Acknowledgements .....	7
Résumé .....	9
Résumé de thèse .....	11
Summary .....	19
Contents.....	21
List of tables .....	24
List of figures .....	25
<b>Chapter 1 Introduction .....</b>	<b>31</b>
1. The International Linear Collider Project .....	33
1.1. A Linear Collider.....	33
1.2. Physics at the ILC.....	34
1.3. The ILC Machine Design .....	37
2. The ILD Detector Concept.....	39
2.1. Particle Flow Concept .....	40
2.2. The ILD Detector Layout .....	41
2.3. Requirements to the Tracking System.....	42
<b>Chapter 2 Time projection chamber principles.....</b>	<b>45</b>
1. Principles of the TPC .....	47
1.1. Drift.....	47
1.2. Diffusion.....	48
1.3. Gas amplification .....	50
2. Micromegas general introduction.....	50
2.1. Micromegas TPC.....	51
2.2. Resistive anode.....	51
<b>Chapter 3 Test-beam setup and Micromegas modules .....</b>	<b>55</b>
1. LCTPC collaboration and EUDET .....	57
2. Micromegas modules .....	62
3. The AFTER chip.....	65
4. The integrated electronics for ILC-TPC.....	73

5. Calculation of the material budget of a module .....	75
5.1. Definition of the radiation length .....	75
5.2. The materials of one module .....	76
5.3. Average thickness in radiation length of a module .....	76
6. Towards the ILD TPC .....	77
<b>Chapter 4 Test bench of Micromegas modules .....</b>	<b>79</b>
1. Introduction of the test-bench .....	81
2. Structure of the test bench .....	82
3. $^{55}\text{Fe}$ energy spectrum .....	85
4. Stability .....	86
5. Module comparison .....	87
<b>Chapter 5 Ion backflow measurement .....</b>	<b>89</b>
1. Experimental setup .....	91
2. Characteristics of the bulk Micromegas detector .....	92
2.1. Gain .....	92
2.2. Energy resolution .....	92
2.3. Electron transparency .....	94
3. Ion backflow measurements .....	94
<b>Chapter 6 Analysis software .....</b>	<b>97</b>
1. Introduction .....	99
2. PRF (Pad Response Function) .....	99
3. FTPC programme .....	101
3.1. FTPC analysis chain .....	102
4. ILCSoft .....	107
5. Micromegas modules analysis chain in MarlinTPC .....	112
<b>Chapter 7 Analysis results .....</b>	<b>115</b>
1. Gain study .....	117
2. Drift velocity study .....	120
3. Analysis with one module .....	121
3.1. Uniformity of different modules .....	121
3.2. Spatial resolution .....	122
3.3. Optimization of the ADC accuracy .....	124
4. Analysis with multiple modules .....	125

4.1. Missing pads.....	125
4.2. Distortions .....	127
4.3. Spatial resolution study .....	128
Conclusion.....	135
<b>Chapter 8 Other Micromegas TPC application: imaging by neutrons .....</b>	<b>139</b>
1. Detector description .....	141
2. The characteristics measurements .....	142
3. The neutron tests .....	143
3.1. $^{241}\text{Am}$ - $^9\text{Be}$ neutron source .....	143
3.2. Neutron imaging.....	144
4. Conclusion.....	147
<b>APPENDIX Kalman Filter in ILCSOFT .....</b>	<b>149</b>
1. The principle of Kalman Filter.....	151
2. Kalman Filter in ILCSOFT .....	153
<b>Bibliography .....</b>	<b>157</b>



# List of tables

<i>Number</i>	<i>Page</i>
Table 1-1. Performance goals and design parameters for an LCTPC with standard electronics at the ILC detector.....	43
Table 3-1. Some main test periods with the test modules.....	59
Table 3-2. Characteristics of the AFTER chip.....	67
Table 3-3. Radiation length of the materials of a module.....	76
Table 6-1. Nominal module positions.....	109
Table 6-2. MarlinTPC processors used for the Micromegas analysis.....	111

# List of figures

<i>Number</i>	<i>Page</i>
Figure R-1. A gauche, diagramme de Feynman du processus de Higgs-strahlung; à droite, événement simulé de top-antitop multijet. ....	12
Figure R-2. A gauche, Micromegas à anode conventionnelle, le signal est sur un seul carreau; à droite, le revêtement résistif-capacitif étale la charge sur plusieurs carreaux. ....	13
Figure R-3. Photographie du prototype 7 modules dans son aimant. ....	13
Figure R-4. Résolution en énergie et gain mesurés sur le banc de test pour chacun des 7 modules. ....	14
Figure R-5. La fraction de retour des ions en fonction du rapport du champ d'amplification au champ de dérive. ....	15
Figure R-6. Résolution moyenne des 22 lignes centrales en fonction de la distance de dérive. La courbe rouge est un ajustement de la fonction 7-0-2. Les points ouverts ne sont pas pris dans l'ajustement. ....	16
Figure R-7. Valeur moyenne des résidus en fonction du numéro de ligne, dans les cas sans et avec champ magnétique. ....	17
Figure R-8. Image obtenue par neutrons à travers un filtre de polyéthylène, sans et avec la coupure en temps maximum. ....	18
Figure 1-1. Production cross section of a 125 GeV SM Higgs boson as a function of $s$ with 80% polarization for the electrons and 20% polarization for the positrons. ....	35
Figure 1-2. Some production cross sections as a function of $s$ at $e^+e^-$ collider. ....	35
Figure 1-3. Diagrams for the Higgs production processes. (a) Higgs-strahlung process, (b) WW fusion process, (c) ZZ fusion process, (d) radiation off tops process. ....	36
Figure 1-4. Simulated event $e + e^- \rightarrow H + \mu\mu$ in the ILD detector. ....	36
Figure 1-5. Coupling of the Higgs boson to different SM particles. ....	37
Figure 1-6. International linear collider design. ....	37
Figure 1-7. Bunch structure of the ILC: 2625 bunches with $2 \times 10^{10}$ particles in each bunch are arranged in a bunch train of about 1 ms length. The train repetition rate is 5 Hz ....	38
Figure 1-8. International Large Detector concept. ....	39
Figure 1-9. One quadrant of the ILD detector concept with its subdetector systems . ....	41

Figure 2-1. (a) The structure of Micromegas detector. (b) Bulk Micromegas fabrication process.....	51
Figure 2-2. Left: The conventional anode using directly signal readout technique. Right: Charge dispersion technique with a resistive anode.....	52
Figure 2-3. The evolution of the 2-dimensional charge density function at five different times. ....	53
Figure 3-1. Large Prototype (LP) with the movable stage in the beam area.....	57
Figure 3-2. The field cage of LP-TPC.....	59
Figure 3-3. The setup of the cosmic trigger. ....	60
Figure 3-4. The design of endplate of LP-TPC . ....	61
Figure 3-5. The Large Prototype with only one module installed in the center.....	62
Figure 3-6. Seven identical modules mounted at the endplate of the Large Prototype.....	63
Figure 3-7. The sketch of the readout pad of a Micromegas module with a typical track from the beam. ....	63
Figure 3-8. Five Micromegas modules with different anode materials. ....	64
Figure 3-9. Left: Photograph of one module; Right: Structure of a module.....	65
Figure 3-10. Front-end electronics of one Micromegas module . ....	66
Figure 3-11. Architecture of the AFTER chip . ....	67
Figure 3-12. 60 fC test pulses recorded by the AFTER chip (120 fC range) for 100 ns, 200 ns, 400ns, and 1 $\mu$ s peaking times. ....	68
Figure 3-13. The uniformity of the ENC for the 1728 channels and a typical map of the r.m.s. noise of the 1728 channels (24 $\times$ 72) of one detector module measured in the 120 fC range and with a 200 ns shaping time. ....	69
Figure 3-14. An example of the global value for the pedestal mean value and the r.m.s. value histogram of 1728 channels.....	70
Figure 3-15. Pedestal of the electronics. Each graph represents a 72-channel AFTER ASIC. ....	71
Figure 3-16. R.m.s. per channel measured with a Micromegas module. ....	72
Figure 3-17. The T2K electronics. (a) the packaging of electronics for one module test; (b) one FEC (14 cm $\times$ 25 cm ). ....	73
Figure 3-18. Artist view and photograph of the new FEC . ....	73
Figure 3-19. New integrated electronics split drawing of one module. ....	74
Figure 3-20. Micromegas module mounted with the new integrated electronics. ....	75

Figure 3-21. (a) An example of a model using Micromegas as the amplification system for the ILD-TPC; (b) An example of a model using GEM as the amplification system for the ILD-TPC .....	77
Figure 4-1. The setup of the test bench. ....	81
Figure 4-2. The set of two mechanical arms which holds the $^{55}\text{Fe}$ source.....	82
Figure 4-3. The structure of the test bench.....	82
Figure 4-4. The display of events using X-rays of $^{55}\text{Fe}$ source and the corresponding histogram of each pad's ADC. (a) Before the filter was added between high voltage and mesh electrode; (b) After the filter was added between high voltage and mesh electrode. .....	83
Figure 4-5. (a) Collimated source ( $^{55}\text{Fe}$ ); (b) Source ( $^{55}\text{Fe}$ ) without collimator. ....	84
Figure 4-6. The map of disconnected pads in one of the modules. The disconnected pads are in dark blue.....	84
Figure 4-7. Mechanical problem: some studs de-soldered.....	84
Figure 4-8. An example of X-rays event tested with collimator. ....	85
Figure 4-9. $^{55}\text{Fe}$ energy spectrum. ....	85
Figure 4-10. Left: the distribution of gain over 16 hours. Right: the gain of the detector as a function of time. ....	86
Figure 4-11. Left: the distribution of energy resolution over 16 hours. Right: the energy resolution as a function of time. ....	87
Figure 4-12. Energy resolution and gain for different modules. ....	87
Figure 5-1. Experimental device (left hand) and schematic diagram of the set up (right hand) for the ion backflow measurement. ....	91
Figure 5-2. Gain as a function of $V_{\text{mesh}}$ for $E_{\text{drift}} = 0.2$ kV/cm at atmospheric pressure. ....	92
Figure 5-3. Measured $^{55}\text{Fe}$ spectrum in a T2K gaseous mixture at $V_{\text{mesh}} = 350$ V and $V_{\text{drift}} =$ 400 V.....	93
Figure 5-4. Energy resolution as a function of the ratio of $E_d/E_a$ ( $E_d$ : drift electric field; $E_a$ : amplification electric field). ....	93
Figure 5-5. Electron transparency as a function of the ratio of $E_d/E_a$ in the T2K gas mixture (normalized to unity). ....	94
Figure 5-6. Ion backflow as a function of the field ratio of $E_a/E_d$ .....	95
Figure 6-1. An example of PRF for different drift distances . ....	100
Figure 6-2. The example of one track in the coordinate system. ....	101

Figure 6-3. The pad pulses. ....	103
Figure 6-4. PRF fitting. (a) top one: the scatter plot of the pad's charge and the relative position of the pad to the track; (b) bottom one: the fitting of the scatter points using PRF function.....	104
Figure 6-5. Profile histogram of the residual with the track in one row before bias correction. ....	105
Figure 6-6. Profile histogram of the residual with the track in one row after bias correction. ....	106
Figure 6-7. Track parameters in MarlinTPC for a straight track. ....	108
Figure 6-8. Schematic overview of the modular structure of Marlin. ....	110
Figure 6-9. More than one track passes through module. The left one shows the tracks pass through module 3 (the middle one at the endplate); the right one shows the signal recorded on the pad where two tracks cross.....	113
Figure 7-1. The histogram of pads' ADC in each row. ....	118
Figure 7-2. The distribution of effective number of electrons for 5 GeV electrons for a gas thickness of 6.85 cm simulated by Heed . ....	118
Figure 7-3. Gain as a function of the mesh voltage. ....	118
Figure 7-4. Gain as a function of the mesh voltage with different drift electric fields. ....	119
Figure 7-5. Drift velocity measurements (B=0 T).....	120
Figure 7-6. Drift velocity measurements (B=1 T).....	121
Figure 7-7. Residual mean in $\mu\text{m}$ for each row (from 0 to 23) at three different drift distances with $B = 1 \text{ T}$ . Blue points are for the module with resistive ink anode and red points are for the module with carbon-loaded polyimide anode.....	122
Figure 7-8. Measured resolution as a function of the drift distance $Z$ at $B=0 \text{ T}$ (data taken with 200 ns peaking time): (a) module 4 (resistive kapton anode with a resistivity of about $3 \text{ M}\Omega/\square$ ), (b) module 5 (resistive kapton anode with a resistivity of about $3 \text{ M}\Omega/\square$ ). ....	123
Figure 7-9. Measured resolution as a function of the drift distance $Z$ at $B=1 \text{ T}$ (data taken with 500 ns peaking time): (a) module 2 (resistive ink anode with a resistivity of about $3 \text{ M}\Omega/\square$ ), (b) module 3 (resistive kapton anode with a resistivity of about $5 \text{ M}\Omega/\square$ ). ....	124
Figure 7-10. Resolution as a function of ADC bits at different drift distances.....	124
Figure 7-11. (a) Beam direction (b) Beam event. ....	125
Figure 7-12. The state of missing pads during first two days test. The missing pads are filled with white colour.....	126

Figure 7-13. The state of missing pads in the last-but-one data taking day. The missing pads are filled with white colour. ....	126
Figure 7-14. Left: the residual versus the row numbers in B=0 T. Right: the residual versus the row numbers in B=1 T. Both are before bias correction. ....	127
Figure 7-15. Left: the residual mean versus the row numbers in B=0 T. Right: the residual mean versus the row numbers in B=1 T. Different colours respond to different drift distances from 15 cm to 50 cm. ....	127
Figure 7-16. Examples of track fitting in one event. Left: multi-tracks in one event; Right: signal track in one event. ....	128
Figure 7-17. Single track event. Left: display with 7 modules; Right: display with the centre module (Zoom). ....	128
Figure 7-18. Fitting track using all hits in one track. (Red line: hit position; Blue line: fit track) ....	129
Figure 7-19. Fitting track with the error affected to the hit 35 set to a very large value so that it does not weight in the chi-squared. (Red line: hit position; Blue line: fit track) .....	130
Figure 7-20. Fitting track after removing the hit in row 35 which has large residual. (Red line: hit position; Blue line: fit track) .....	130
Figure 7-21. Distribution of the residuals at 15 cm drift distance. Top: including the test hit in the track fit; Bottom: excluding the test hit in the track fit. Here only shows 3 rows of 72 rows. ....	131
Figure 7-22. Resolution of each row of the central module. ....	131
Figure 7-23. Spatial resolution of the central module at B=1 T. Data with seven modules taken in 2013. ....	132
Figure 7-24. Extrapolation of the spatial resolutions of Micromegas and GEM to the ILD-TPC. ....	133
Figure 7-25. Resolution as a function of the crossing angle at different drift distances in B=1 T. ....	133
Figure 8-1. Sketch of the FNI detector. ....	141
Figure 8-2. The PCB of the neutron detector (sensitive area: 57.4 mm × 88.6 mm). ....	141
Figure 8-3. Energy resolution of the <sup>55</sup> Fe spectrum. ....	142
Figure 8-4. Gas gain as a function of the mesh voltage in 95% Ar+5% isobutane. ....	143
Figure 8-5. <sup>241</sup> Am- <sup>9</sup> Be source spectrum according to ISO 8529 standard. ....	144

Figure 8-6. The conversion efficiency as a function of the thickness of the polyethylene ( $[\text{C}_2\text{H}_4]_n$ ) layer simulated by Geant4. ....	144
Figure 8-7. Left: the setup of the neutron imaging test. Right: the corresponding imaging. .	145
Figure 8-8. Polyethylene masks used for the neutron imaging. ....	145
Figure 8-9. A typical neutron event with the maximum time and the minimum time in this cluster. ....	146
Figure 8-10. Maximum time-difference in one cluster in 40 ns time bin. ....	146
Figure 8-11. Neutron imaging. (a) Integrating the ADC of all events in one pad. (b) Reconstructed using the time information. ....	147
Figure 0-1. Geometric interpretation of the helix parameters for (a) negatively and (b) positively charged tracks .....	154

Chapter 1  
**Introduction**





# 1. The International Linear Collider Project

The International Linear Collider (ILC) is a world-wide project for a future linear particle accelerator. The positron-electron ( $e^+e^-$ ) beams will collide at the centre-of-mass (cms) energy of 200-500 GeV (with a possible later upgrade to 1 TeV). At present, the Large Hadron Collider (LHC) [1] is the world's largest and highest-energy particle accelerator with high energy colliding proton beams. It is designed to reach centre-of-mass energies of 14 TeV with a high peak luminosity of  $10^{34} \text{ cm}^{-2}\text{s}^{-1}$ . The energy of the proton constituents is not fixed and partons collide with all possible energies. Thus a hadron collider covers a wide energy range at the constituent level while running at a fixed beam energy which makes them well suited as discovery machines. Its goals are to further test the Standard Model, determine what breaks the electroweak symmetry, search for new forces of nature, and produce dark matter candidates. But measurements at LHC cannot reach the highest precision. Firstly, the centre-of-mass energy is not adjustable and the initial energy of an interaction is unknown, as well as the precise kinematics. Secondly, the proton-proton interaction cross-section is dominated by inelastic background QCD processes. This means that each interesting signal event is accompanied by large backgrounds produced by the interaction of other parton collisions and it even overlaps with many other proton-proton collisions. The ILC, with its much lower experimental background, polarised beams, and tunable collision energies, will provide precision measurements regarding the LHC discoveries.

## 1.1.A Linear Collider

In a lepton collider, the initial state energy and the polarization are well known and could be changed. The interaction of electrons and positrons is purely electroweak and the Standard Model background is low. The requirements for radiation hardness are smaller compared to the LHC. This allows for high-precision detectors with low material budget.

To increase the energy to the required level, a linear collider instead of a circular collider will be needed. In a ring accelerator, the energy loss in one turn due to synchrotron radiation emitted by accelerated particles is

$$\Delta E \propto \frac{E^4}{R \cdot m^4} \text{ and for the electrons } \Delta E_{e^\pm} [\text{MeV}] \approx 8.85 \cdot 10^{-2} \frac{(E[\text{GeV}])^4}{R[\text{m}]} .$$

Here, R is the curvature radius of the accelerator, m is the particle mass and E is the beam energy. The energy loss increases with the fourth power of the beam energy and decreases

only linearly with the radius. This makes a circular lepton collider unacceptably large if it is supposed to run beyond cms energy of  $\sqrt{s} = 300$  GeV. Therefore the ILC will be a linear machine to avoid the synchrotron radiation losses.

## 1.2. Physics at the ILC

On July 4, 2012, both the CMS [2] and ATLAS [3] teams working at LHC announced the discovery of a new particle in the mass region around 125-126 GeV, with a statistical significance at the level of 5 sigma [4]. A 5-sigma result represents a one-in-3.5 million chance of the result being noise. This is an undeniable proof that a boson, with very Higgs-like properties, has been discovered by the two collaborations. However, a full characterisation of the Higgs includes a measurement of its total decay width, spin, production cross-section and coupling to the known Standard Model (SM) particles. These measurements are very difficult or impossible to perform at the LHC. The task of the ILC will be to measure precisely their properties. In contrast to hadron interactions, the  $e^+e^-$  collisions are characterised by much lower background and the ILC provides an accurate knowledge of the initial conditions like centre-of-mass energy, initial state helicity and charge. The ILC will be the first  $e^+e^-$  collider to reach the  $t\bar{t}$  production threshold at around 350 GeV. This allows the mass and the electroweak properties of the top quark to be accurately measured.

At the ILC, one will measure the mass, spin, and coupling strengths through all decay channels. The main production mechanisms for SM-like Higgs particles at an  $e^+e^-$  collider are as follows. Figure 1-1 shows the production cross-section of a 125 GeV SM Higgs boson as a function of  $\sqrt{s}$  with 80% polarization for the electrons and 20% polarization for the positrons and figure 1-2 shows some production cross sections as a function of  $\sqrt{s}$ .

- a. Higgs-strahlung process:  $e^+e^- \rightarrow (Z) \rightarrow Z + H$
- b. WW fusion process:  $e^+e^- \rightarrow \bar{\nu}\nu(WW) \rightarrow \bar{\nu}\nu + H$
- c. ZZ fusion process:  $e^+e^- \rightarrow e^+e^-(ZZ) \rightarrow e^+e^- + H$
- d. Radiation off tops:  $e^+e^- \rightarrow (\gamma, Z) \rightarrow t\bar{t} + H$

Unseen intermediate states are indicated between parentheses. The corresponding diagrams of these Higgs production processes are shown in figure 1-3.

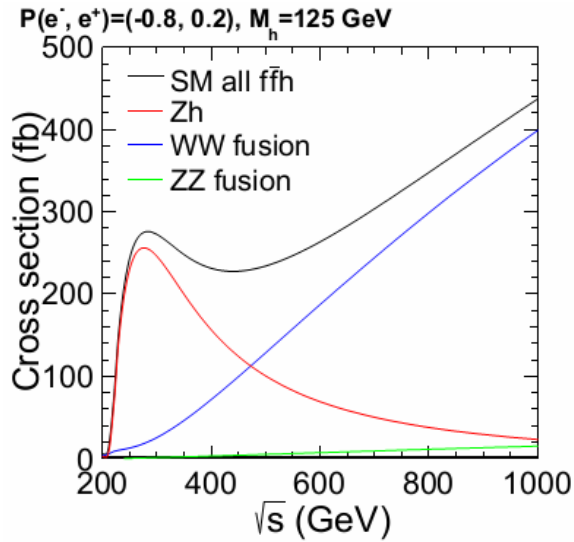


Figure 1-1. Production cross section of a 125 GeV SM Higgs boson as a function of  $\sqrt{s}$  with 80% polarization for the electrons and 20% polarization for the positrons [5].

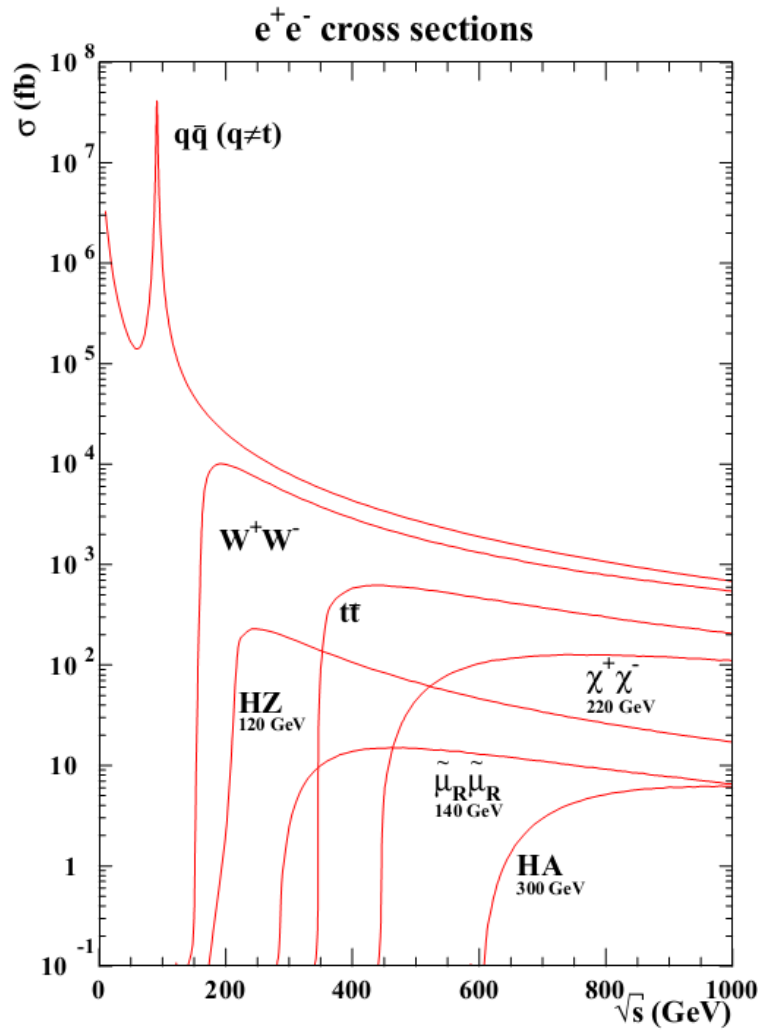


Figure 1-2. Some production cross sections as a function of  $\sqrt{s}$  at  $e^+e^-$  collider [6].

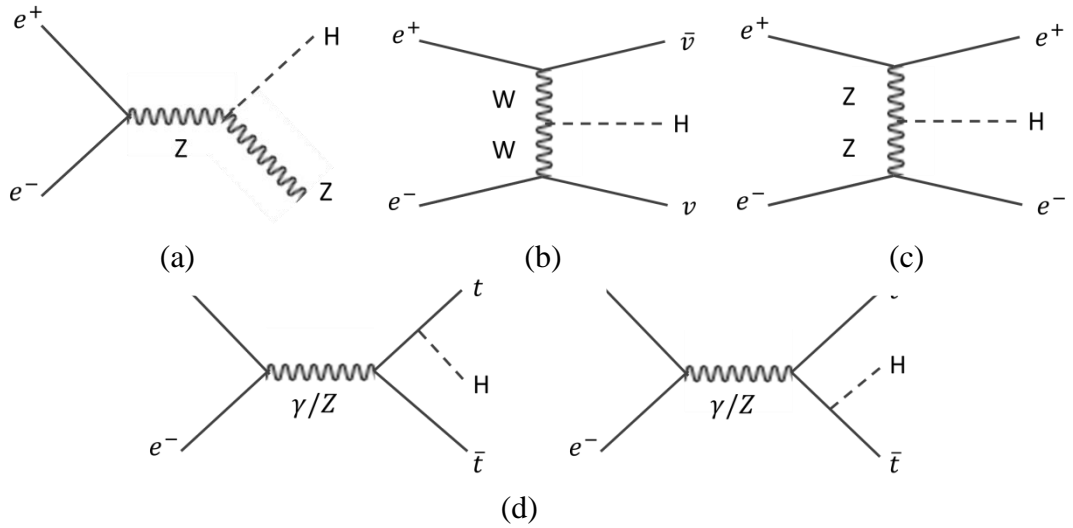


Figure 1-3. Diagrams for the Higgs production processes. (a) Higgs-strahlung process, (b) WW fusion process, (c) ZZ fusion process, (d) radiation off tops process.

At the production threshold the dominating process is Higgs-strahlung (figure 1-3 (a)). A highly virtual Z boson produced in the  $e^+e^-$  annihilation radiates a Higgs boson. This process allows reconstructing the Higgs mass independently of Higgs decay mode, only from the Z recoil mass. A 125 GeV Higgs predominantly decays into  $b\bar{b}$ . The Z can decay into quarks or leptons. Especially the channel  $HZ \rightarrow b\bar{b}\mu^+\mu^-$  has a clear signature and low background. Such an event, coming from an International Large Detector (ILD) simulation, is illustrated in figure 1-4.

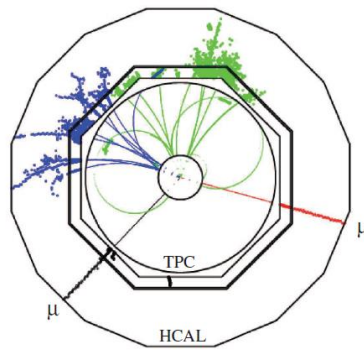


Figure 1-4. Simulated event  $e^+e^- \rightarrow H + \mu\mu$  in the ILD detector [7].

In the analysis, the decay of the Higgs boson will be studied and its absolute decay branching ratios be measured. For a known Higgs mass, the Standard Model predicts the branching ratios of the decay mode as shown in figure 1-5. The measurement of the Higgs decay branching ratio allows the Standard Model to be tested and is sensitive to new physics.

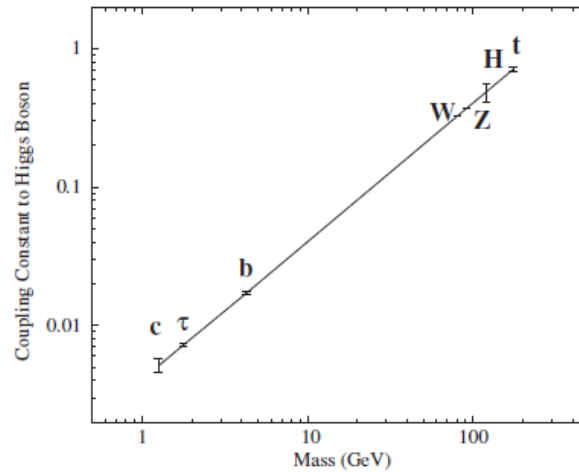


Figure 1-5. Coupling of the Higgs boson to different SM particles [8].

Besides the Higgs boson, the ILC will be able to study several other SM processes. It will more precisely measure the top quark mass. These measurements will profit from the possibility to adjust finely the centre-of-mass energy because they require threshold scans and resonant production of the interesting particles.

### 1.3. The ILC Machine Design

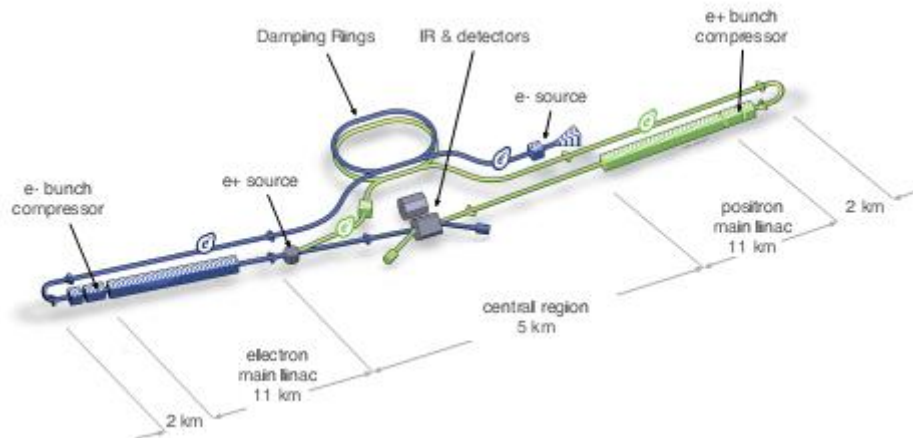


Figure 1-6. International linear collider design [9].

The centre-of-mass energy of ILC will be about 200-500 GeV with an upgrade option to 1 TeV. Polarised electron and polarised positron beams will be provided and will collide at a crossing angle of 14 mrad. The overall length will be about 31 km. Two detectors will be alternately moved into the beam position with a “push-pull” scheme. Figure 1-6 shows the overview sketch of the design of the ILC.

To reduce the emittance of the electron and positron beams, damping rings are used. In order to save money, both damping rings – for electrons and positrons – are positioned in a single tunnel in the middle of the accelerator. Firstly, the beam particles are filled into a 3.2 km circumference damping rings [9]. They are operated at beam energy of 5 GeV. The prepared beams will enter into the linacs and will be accelerated towards the interaction point. In between, the electrons are directed to an undulator and the high energy photons are emitted. These photons hit a positron production target to produce positrons. Then, the produced positrons are filled back into the positron damping ring. In this way, electrons are extracted from a conventional electron source and positrons are created during the runtime.

The beams are delivered to the interaction region, where two movable detectors are placed. In this so-called push-pull concept one detector will take data, while the other one is maintained in parking position. The position will be changed on a regular basis. However, such a push-pull option concept requires many technical challenges and a large development effort. In order to simplify the extraction of the beams from the detectors, a crossing angle of 14 mrad between the two beams is foreseen.

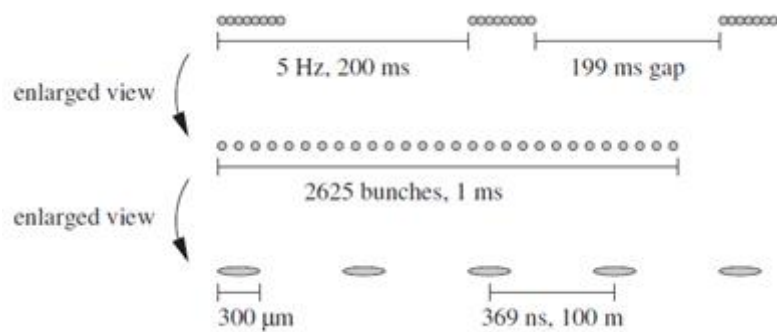


Figure 1-7. Bunch structure of the ILC: 2625 bunches with  $2 \times 10^{10}$  particles in each bunch are arranged in a bunch train of about 1 ms length. The train repetition rate is 5 Hz [10].

The ILC is designed to reach a peak luminosity of  $2 \times 10^{34} \text{ cm}^{-2} \text{ s}^{-1}$ . The electron beam will have a polarisation of up to 80% and positrons will be 30% polarised [11]. Instead of particles being delivered in continuous beams, they are grouped in bunches which are caused by the acceleration in cavities. The bunch structure for the ILC is illustrated in figure 1-7. The bunch trains are delivered with a repetition rate of 5 Hz. The train composed of 2625 bunches with  $2 \times 10^{10}$  particles is 1 ms long, followed by a gap of 199 ms.

## 2. The ILD Detector Concept

At the ILC, the Higgs mechanism will be investigated in detail and the new physics will be studied. The high precision of measurement in the ILC detectors is required to meet the comprehensive physics programme for the ILC.

One of the most challenging tasks is to separate  $Z \rightarrow q\bar{q}$  from  $W \rightarrow q\bar{q}$  final states. As an example, this is needed to distinguish between  $H \rightarrow ZZ$  and  $H \rightarrow WW$  decays or to study  $WW \rightarrow WW$  scattering. The quarks are created in a  $Z$  or  $W$  decay and produce a jet of particles in the detector. To clearly separate these two decay modes, the resolution of the measurement of the jet energies has to be better than  $\Delta E/E \approx 3 - 4\%$  [12]. To study the Higgs recoil mass and low multiplicity events, a very good momentum resolution and a large angular coverage with high efficiencies of tracking system are needed. Another important detector performance parameter is the flavour-tagging ability by means of the lifetime signature. A very precise and efficient vertex detector is needed to meet this requirement. For example, this is necessary to measure branching ratios of Higgs decays into  $b$ ,  $c$  and  $\tau$ .

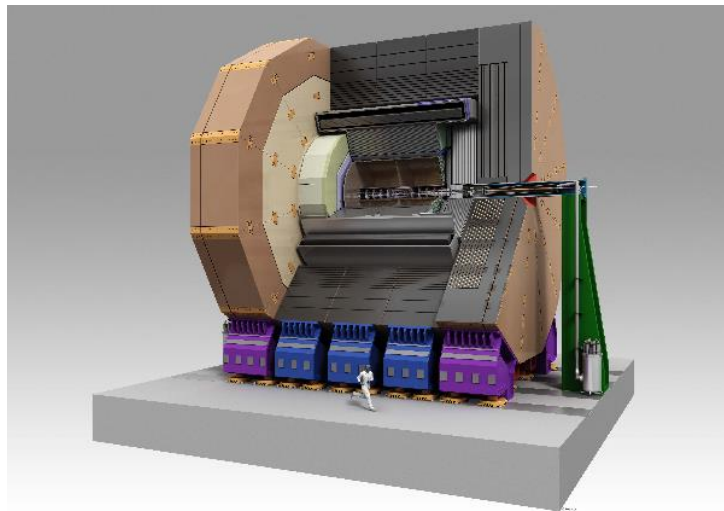


Figure 1-8. International Large Detector concept [13].

The International Large Detector (ILD) shown in figure 1-8 is based on two previous designs of the GLD (Gaseous Large Detector) [14] and the LDC (Large Detector Concept) [15]. The central component of the ILD tracker is a Time Projection Chamber (TPC). This is supplemented by a system of silicon-based tracking detectors, which provide additional measurement points inside and outside of the TPC, and extend the angular coverage down to



very small angles. The b and c quark tagging as well as vertex reconstruction is performed with an accurate vertex detector based on silicon pixel detectors. The TPC is surrounded by a tungsten absorber-based electromagnetic calorimeter (ECAL) and a steel-based sampling hadronic calorimeter (HCAL). The highly granular calorimeter with the accurate tracking system (Particle Flow Approach) ensures the precise jet energy resolution.

## 2.1. Particle Flow Concept

To satisfy the jet energy resolution of the ILD detector required by the ILC, the Particle Flow concept is proposed. In this concept, the full four momentum vectors of all particles which come from the interaction region, are reconstructed using all sub-detectors instead of only the calorimeter. In the tracking system, the momentum  $p$  of charged particles is precisely measured. It translates via  $E^2 = p^2 + m^2$  into energy. The mass is supposed to be negligible at typical ILC energies. To avoid double counting, if the energy deposited in the calorimeter matches the measurement in the tracking detector, it will be removed from the calorimetric information. Photons are identified in the electromagnetic calorimeter (ECAL) and muons are identified by the muon detector, which is inside the iron return yoke. The hadronic calorimeter (HCAL) is used to precisely measure the neutral mesons and hadrons. A jet energy in the particle flow concept is the sum of the energies of all individual particles in the jet. A correct assignment of calorimeter showers to reconstructed tracks is required. The resolution of the detector and the reconstruction software algorithms influences the performance of the particle flow. To realize such a particle flow concept, the calorimeters have to be highly granular in 3 dimensions for good separation of showers.

The energy resolution of a jet is a quadratic sum of the energy resolutions of all sub-detectors and a so-called confusion term:

$$\frac{\sigma(E)}{E} = \frac{\sigma(E_{charged})}{E} \oplus \frac{\sigma(E_{hadron})}{E} \oplus \frac{\sigma(E_{em.})}{E} \oplus \frac{\sigma(E_{confusion})}{E}$$

An ideal jet energy resolution measured in the calorimeter and tracking detector can reach  $20\%/\sqrt{E}$ . To meet the requirement of jet energy resolution, the additional contribution due to the confusion term must be kept below  $20\%/\sqrt{E}$ .

In summary, the requirements for the overall detector design are as follows:

The detector must be as hermetic as possible to minimise the number of particles which escape detection.

The tracking system must be highly efficient and allow for a precise momentum measurement.

The material budget of the tracking system must be minimised to reduce multiple scattering and conversion of particles before they reach the calorimetric system.

The calorimeter must be finely segmented to allow for a correct assignment of calorimeter clusters to particles, even in the high particle densities of a jet.

## 2.2.The ILD Detector Layout

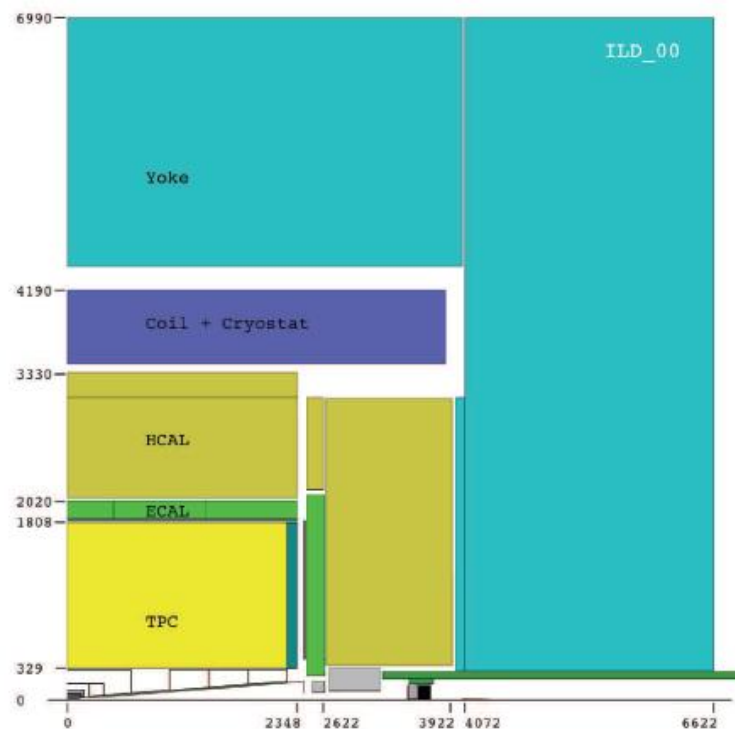


Figure 1-9. One quadrant of the ILD detector concept with its subdetector systems [16].

The ILD detector has been optimised to meet the particle flow concept. Figure 1-9 shows a schematic view of one quadrant of the ILD detector. The bottom left corner of the figure is the interaction point.

The silicon pixel detectors are used as the vertex detector. They are installed around the interaction and approach it down to a distance of 15 mm. These detectors measure about 10 points per particle trajectory with a precision in the 10  $\mu\text{m}$  range. These detectors are important for flavour tagging and the measurement of tracks with very low momenta, which are not able to reach the main tracker.

The vertex detector is surrounded by a large volume Time Projection Chamber (TPC). In the case of the ILD, the TPC is the main tracking detector. It records up to 200 three-dimensional space points per particle and provides quasi-continuous tracking. The resolution of the TPC is aimed at about 100  $\mu\text{m}$  per measured point in the  $r - \varphi$  plane and 500  $\mu\text{m}$  in the  $z$  direction.

The calorimeters consist of an electromagnetic and a hadronic system. The ECAL is a tungsten-silicon sampling calorimeter. The cell size is planned to be  $1 \times 1 \text{ cm}^2$  and 30 active layers are used. For the HCAL, a steel sampling calorimeter is planned with either scintillating tiles with optical readout, or Micromegas, or resistive plate chambers, as sensitive layers. The depth of the calorimeter is five interaction lengths  $\lambda$  and the cell size is  $3 \times 3 \text{ cm}^2$  in up to 48 layers.

The calorimeter system is completed by a system of radiation-hard detectors in the very forward region around the outgoing beam pipes. These specialised calorimeters measure the luminosity and monitor the beam energy spectrum. The LumiCAL measures Bhabha-scattered electrons and positrons and is built similar to the ECAL. It adds calorimetric information for polar angles down to 40 mrad. The BeamCAL made of tungsten-silicon or even tungsten-diamond is another sampling calorimeter, measuring down to 5 mrad. It has to stand high radiation level through beam-induced background and uses those particles to determine parameters of bunch crossings. It can also be used as feedback and control for the beam delivery system. The last component is the LHCAL which serves as an extension of the HCAL down to very small  $\theta$ .

A superconducting solenoidal coil provides an axial-magnetic field of 3.5 T in the detector, which forces charged particles on curved trajectories for the momentum measurement. An iron yoke returns the magnetic field line outside the magnet. It also serves as a muon detector with resistive plate chambers and as a tail catcher for the HCAL.

### **2.3.Requirements to the Tracking System**

In the magnetic field  $B$ , the trajectory of the particle is curved. The inclination angle  $\theta$  between the reconstructed particle trajectory and the beam axis can be measured, as well as the radius  $R$  of the circular projection. The momentum of the particle  $P$  can be calculated from

$$P_T = P \sin\theta \quad \text{and} \quad P_T([\text{GeV}]) \approx 0.3R[\text{m}]B[\text{T}]$$

where  $P_T$  is the component of the momentum vector perpendicular to the beam axis.

In the ILD concept, a momentum resolution of  $\delta_{p_{\perp}}/P_{\perp}^2 \approx 2 \cdot 10^{-5} \text{ GeV}^{-1}$  is required for the whole tracking system. The main reason is for example the measurement of the Higgs recoil mass at the ILC. The momentum measurement accuracy of the TPC is foreseen to achieve  $\delta_{p_{\perp}}/P_{\perp}^2 \approx 9 \cdot 10^{-5} \text{ GeV}^{-1}$  at 3.5 T. Using the Glückstern formula [17],

$$\frac{\delta_{p_{\perp}}}{P_{\perp}^2} = \frac{\sigma_{\perp}}{0.3BL^2} \sqrt{\frac{720}{N+4}} \left( \frac{Tm}{\text{GeV}/c^2} \right)$$

the momentum resolution can be translated into single point resolution  $\sigma_{\perp}$  with respect to the r- $\phi$  plane, which is measurable in prototypes. B is the magnetic field, L is the projected length of the trajectory in the TPC and N is the number of measured space points. With a good resolution and many hits a good momentum resolution can be achieved. For the ILD TPC, there are about 200 measured points per track. With a track length of 2 m in a magnetic field of 3.5 T, a single-point resolution of 100  $\mu\text{m}$  over the whole length of the chamber is required in order to reach the envisaged goal.

The complete tracking requirements of the TPC are summarized in table 1-1.

Size	$\phi = 3.6\text{m}, L = 4.3\text{m}$ outside dimensions
Momentum resolution (3.5T)	$\delta(1/p_t) \sim 9 \times 10^{-5}/\text{GeV}/c$ TPC only ( $\times 0.4$ if IP incl.)
Momentum resolution (3.5T)	$\delta(1/p_t) \sim 2 \times 10^{-5}/\text{GeV}/c$ (SET+TPC+SIT+VTX)
Solid angle coverage	Up to $\cos \theta \simeq 0.98$ (10 pad rows)
TPC material budget	$\sim 0.05X_0$ including the outer fieldcage in $r$ $\sim 0.25X_0$ for readout endcaps in $z$
Number of pads/timebuckets	$\sim 1 - 2 \times 10^6/1000$ per endcap
Pad size/no.padrows	$\sim 1\text{mm} \times 4\text{--}6\text{mm}/\sim 200$ (standard readout)
$\sigma_{\text{point}}$ in $r\phi$	$< 100\mu\text{m}$ (average over $L_{\text{sensitive}}$ for straight radial tracks)
$\sigma_{\text{point}}$ in $rz$	$\sim 0.4 - 1.4 \text{ mm}$ (for zero–full drift)
2-hit resolution in $r\phi$	$\sim 2 \text{ mm}$ (for straight radial tracks)
2-hit resolution in $rz$	$\sim 6 \text{ mm}$ (for straight radial tracks)
dE/dx resolution	$\sim 5 \%$
Performance	$> 97\%$ efficiency for TPC only ( $p_t > 1\text{GeV}/c$ ), and $> 99\%$ all tracking ( $p_t > 1\text{GeV}/c$ )[6]
Background robustness	Full efficiency with 1% occupancy, simulated for example in Fig. 1.3(right)
Background safety factor	Chamber will be prepared for $10 \times$ worse backgrounds at the linear collider start-up

Table 1-1. Performance goals and design parameters for an LCTPC with standard electronics at the ILC detector [18].

Another challenge is the reduction of the material budget of the TPC structure, measured in radiation lengths  $X_0$ . Ideally, the hard scattering process of all particles is only starting from

one of the calorimeters. However, some particles are occasionally scattered and get a new direction in the TPC structure. Hence, the low material budget of the tracking sub-detector is required to reduce the impact of interaction in the tracking system. The material of TPC structure must be optimised with  $X_{\text{wall}} \leq 0.01 X_0$  for the inner field cage,  $X_{\text{wall}} \leq 0.05 X_0$  in the outer field cage and  $\leq 0.25 X_0$  in the endplate. Two MPGD technologies are considered as the readout for the ILD TPC: Micromegas (MICRO-MESH Gaseous detector) and GEM (Gas Electron Multiplier).

## Chapter 2

# **Time projection chamber principles**



The Time Projection Chamber (TPC) was invented by D.R.Nygren in 1974 [19]. It has a large drift volume filled with gas. A homogeneous electric field is provided by a voltage divider chain of resistors in the drift volume. There is also a magnetic field parallel to the electric field. When a charged particle traverses the drift volume, it collides with the gas molecules and induces the gas ionization along its trajectory. In the electric field, the ionized electrons drift toward the anode, while the ions drift toward the cathode. By recording the position of the ionized electrons at the anode and the time at which the electrons reach the anode, the projection of the track can be reconstructed in three dimensions. The TPC can be used to reconstruct the track of particles, measure their momenta, and identify the particles by measuring their ionization energy loss in the volume. A detailed discussion about the characteristics of the drift chamber can be found in [20]. Some reviews of TPC can be found in [21][22].

## 1. Principles of the TPC

### 1.1.Drift

The drift velocity  $\vec{v}$  of a charged particle under the action of the electric field  $\vec{E}$  and magnetic field  $\vec{B}$  is described by the Langevin equation:

$$m \frac{d\vec{v}}{dt} = e\vec{E} + e(\vec{v} \times \vec{B}) + \vec{Q}(t) \quad (2-0-1)$$

where  $m$  is the mass of the charged particle,  $e$  is its charge, and  $\vec{Q}(t) = -K\vec{v}$  describes the average (friction) force due to scattering of the particles with the gas molecules.

For the velocity  $\vec{v}_D$  averaged over many collisions, the Langevin equation has the stationary solution

$$\vec{v}_D = \mu\vec{E} + \tau\vec{v}_D \times \vec{\omega} \quad (2-0-2)$$

where  $\tau = m/K$  is the average time between two collisions of the charged particle and the gas molecules,  $\mu = e\tau/m$  is the electron mobility and  $\vec{\omega} = e\vec{B}/m$  is the cyclotron frequency. Using  $\hat{E}$  and  $\hat{B}$  as the unit vectors of the electric and magnetic field, the equation can be written as follows:

$$\vec{v}_D = \frac{\mu E}{1 + \omega^2 \tau^2} \cdot [\hat{E} + \omega\tau\hat{E} \times \hat{B} + \omega^2\tau^2(\hat{E} \cdot \hat{B})\hat{B}] \quad (2-0-3)$$



In a TPC, the electric field is parallel to the magnetic field, which means that the second term in equation 2-0-3 vanishes:

$$\omega\tau \cdot \hat{E} \times \hat{B} = 0 \quad (2-0-4)$$

and the last term can be written as:

$$(\hat{E} \cdot \hat{B})\hat{B} = \hat{B} = \hat{E} \quad (2-0-5)$$

The equation 2-0-3 can be simplified as follows:

$$\vec{v}_D = \frac{\mu E}{1+\omega^2\tau^2} \hat{E}(1 + \omega^2\tau^2) = \mu\vec{E} \quad (2-0-6)$$

If there is an angle  $\alpha$  between electric field and magnetic field, it yields

$$v_D = \frac{\mu E}{1+(\omega\tau)^2} \sqrt{1 + (1 + \cos^2\alpha) \cdot (\omega\tau)^2 + (\omega\tau)^4 \cdot \cos^2\alpha} \quad (2-0-7)$$

When the angle  $\alpha \leq 45$  degree, the drift velocity is approximated as follows within a few percent correction:

$$v_D \approx \frac{\mu E}{1+(\omega\tau)^2} \cdot (1 + (\omega\tau)^2 \cdot |\cos\alpha|) \quad (2-0-8)$$

In the extreme case, where the electric field and magnetic field are perpendicular, the last term of the equation 2-0-7 is zero, the drift velocity becomes

$$v_D = \frac{\mu E}{\sqrt{1+(\omega\tau)^2}} = \frac{e\tau E}{m\sqrt{1+(\omega\tau)^2}} \quad (2-0-9)$$

## 1.2. Diffusion

Charged particles which are released in a cloud will diffuse when they drift to the electrode. This influences the spatial resolution. In the field-free case, the diffusion is caused by thermic effects and is isotropic. The mean velocity of the electrons in all directions can be described as:

$$v = \sqrt{\frac{8kT}{\pi m_e}} \quad (2-0-10)$$

where  $k$  is the Boltzmann constant,  $T$  is the gas temperature.

In this case, the probability that an electron has no interaction with the gas molecules after a time  $t$  is  $\exp(-\frac{t}{\tau})$ . With  $\lambda$  as the mean free path length, the spread  $\delta_0$  that the electron deviates from its expected position in any fixed direction is approximately given by [23]:

$$\delta_0^2 = \frac{1}{3} \int_0^\infty \frac{dt}{\tau} \exp(-\frac{t}{\tau}) \cdot \left(\lambda \frac{t}{\tau}\right)^2 = \frac{2}{3} \lambda^2 \quad (2-0-11)$$

After a large number of collisions ( $t \gg \tau$ ), the width of the charge cloud has grown to:

$$\sigma_0^2(t) = \delta_0^2 \frac{t}{\tau} = \frac{2}{3} \lambda^2 \frac{t}{\tau} \quad (2-0-12)$$

The general diffusion coefficient is defined as:

$$\widetilde{D}_0 = \frac{\sigma_0^2(t)}{2t} = \frac{1}{3} \frac{\lambda^2}{\tau} = \frac{1}{3} v \lambda \quad (2-0-13)$$

### 1.2.1. Influence of the electric field

In an electric field, the velocity will increase depending on the choice of the chamber gas. In “cool gas”, like CO<sub>2</sub>, the thermal movement is dominant even in a relatively large field. On the other hand, in some gas, like Argon, the movement strongly depends on the electric field and pressure (E/P). In this case, the non-thermal movement is dominant and the diffusion becomes non-uniform.

For the diffusion coefficient, a more common definition is:

$$D = \sqrt{\frac{2\widetilde{D}_0}{v_D}} \quad (2-0-14)$$

here,  $v_D$  is the drift velocity of electron. And the width of the charge cloud  $\sigma_D$  is then:

$$\sigma_D = D\sqrt{L} \quad (2-0-15)$$

here  $L$  is the drift distance.

### 1.2.2. Influence of the magnetic field

With an applied magnetic field along the direction of the drift, the Lorentz force causes the transverse movement of the charged particle to be on a circular arc. The transverse diffusion is strongly suppressed and the longitudinal diffusion is not affected. The spread  $\delta_B$  that the electron deviates from its expected position can be written as:

$$\delta^2(B) = \frac{1}{2} \int_0^\infty \frac{dt}{\tau} \exp\left(-\frac{t}{\tau}\right) \cdot \left(2\rho \sin \frac{v_T t}{2\rho}\right)^2 = \frac{1}{2} \frac{\tau^2 v_T^2}{1 + \omega^2 \tau^2} \quad (2-0-16)$$

where  $v_T$  is the transverse velocity and  $\rho$  is the radius of the circular arc given by  $\rho = v_T/\omega$ .

After a large number of collisions ( $t \gg \tau$ ), the width of the charge cloud becomes:

$$\sigma^2(B, t) = \frac{t}{2} \frac{\tau v_T^2}{1 + \omega^2 \tau^2} = t \frac{\widetilde{D}_0}{1 + \omega^2 \tau^2} \quad (2-0-17)$$

Hence, the transverse diffusion can be defined as:

$$\widetilde{D}_T(B) = \frac{\widetilde{D}_0}{1 + \omega^2 \tau^2} \quad (2-0-18)$$

### 1.3. Gas amplification

If the electric field is above 10 kV/cm, the primary electrons are accelerated and gain enough energy between two collisions to ionize the gas. The primary electrons and the secondary electrons are accelerated further and can produce new electrons, which lead to a gas avalanche multiplication. The developing number of electrons  $N$  can be calculated by:  $N(X) = N_0 \cdot e^{\alpha X}$ .

Where  $X$  is the distance and  $\alpha$  is the first Townsend coefficient, which describes the probability for one ionization per unit length and depends on the gas mixture, the temperature, the pressure and the strength of the electric field. Since the amplification of TPC is operated in the proportional mode, the gas gain can be calculated by:

$$G = \frac{N(x)}{N(x_0)} = \exp\left(\int_{x_0}^x \alpha(x) dx\right) \quad (2-0-19)$$

where  $x_0$  and  $x$  are the starting point and the end point of the avalanche respectively,  $N(x_0)$  is the number of primary electrons and  $N(x)$  is the number of electrons after amplification.

## 2. Micromegas general introduction

The MICRO MESH Gaseous detector (Micromegas) was first introduced in 1996 by I. Giomataris [24]. Because of its good characteristics, high spatial resolution ( $< 50 \mu\text{m}$ ) and high gain ( $> 10^4$ ), good energy resolution, excellent timing resolution ( $\sim 5 \text{ ns}$ ) and robustness [25], it has been widely applied in many high energy physics experiments. The Micromegas detector is a parallel-plate avalanche chamber and is divided into two gaps by a micromesh electrode, several mm drift gap and  $\sim 100 \mu\text{m}$  amplification gap. By applying proper voltages in these three electrodes, a low electric field (about a few 100 V/cm) in the drift gap and a very high electric field (about 100 kV/cm) in the amplification gap are obtained. When a charged particle enters the detector, it induces the gas ionization in the drift gap. Under the

action of the electric field, the primary ionized electrons pass through the mesh and induce avalanche in the amplification gap. The ion cloud induced in the small amplification gap is quickly collected on the micro-mesh and only a small part of it escapes to the drift gap.

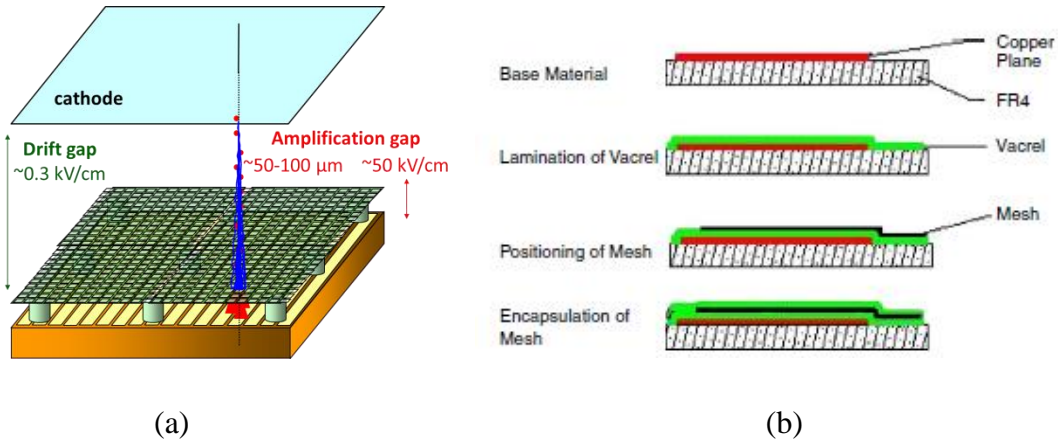


Figure 2-1. (a) The structure of Micromegas detector. (b) Bulk Micromegas fabrication process.

In order to obtain large area detectors, a new bulk Micromegas technique was developed in 2006 [26] shown in figure 2-1. It uses one or more photo resistive film laminated on the anode printed circuit board (PCB) to define the amplification gap. The micro-mesh is laminated on the top and encapsulated with another layer of photo resistive film, like a sandwich structure. Then, the photo-resistive film is exposed to UV light and subsequently etched to produce insulating pillars by photo-lithography.

## 2.1. Micromegas TPC

A Micromegas TPC is a TPC based on the Micromegas as the readout system instead of the wire chamber. The drift gap extends over a large distance. The drifting electrons avalanche in a high field between the mesh and anode which provides amplification of the order of thousand. Compared to the standard wire TPCs, the  $E \times B$  effect is significantly reduced and the spatial resolution is greatly improved in a Micromegas TPC. This is important for the two-track separation in the jets. On the other hand, Micromegas detectors are easy to build with large surface.

## 2.2. Resistive anode

In the high magnetic field, the transverse diffusion is significantly suppressed. The traditional readout pads need to be much narrower to keep the accuracy of the computed centroid of

signals by collecting directly charge signals. The number of readout channels is significantly increased with it. This requires much more materials and cost and also leads to be difficult to manage for a large detector. To improve the spatial resolution for wide pads, a new technology of charge dispersion was developed and firstly studied at Carleton University [27]. It uses a high surface resistive thin layer bonded to the readout pad plane with an insulating layer. Figure 2-2 expounds the difference between the conventional MPGD anode and resistive anode and we can clearly see that a centroid calculation is less precise using the conventional MPGD anode. The resistive layer and the readout plane form a distributed 2-dimensional resistive-capacitive network to spread the avalanche charge in several adjacent pads. The avalanche charge depositing on this layer disperses with the system RC time constant. The RC constant is determined by the surface resistivity of the resistive layer and the capacitance per unit area, which is determined by the space between the resistive layer and the readout plane and the dielectric constant of the insulating layer.

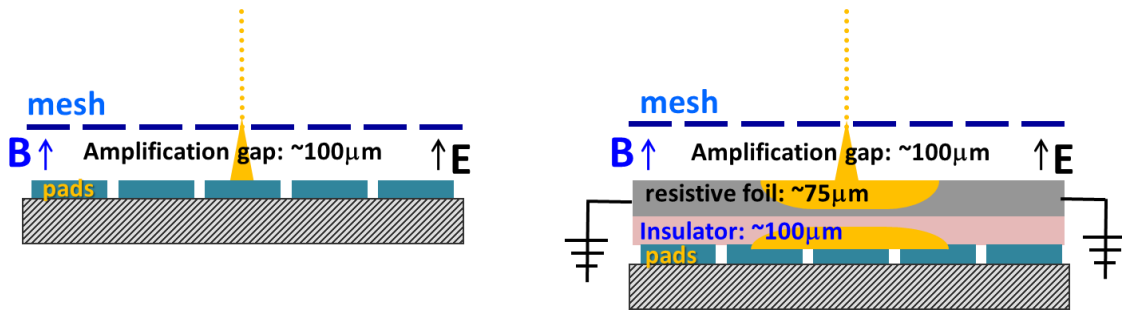


Figure 2-2. Left: The conventional anode using directly signal readout technique. Right: Charge dispersion technique with a resistive anode.

When a charge is deposited on the resistive layer, the telegraph equation for the surface charge density on the 2-dimensional continuous RC network is given by:

$$\frac{\partial \rho}{\partial t} = h \left( \frac{\partial^2 \rho}{\partial r^2} + \frac{1}{r} \frac{\partial \rho}{\partial r} \right) \quad (2-0-20)$$

where  $\rho(r, t)$  is the surface charge density, and  $h = 1/RC$ . Here R is the surface resistivity of the resistive layer and C is the capacitance per unit area.

At time  $t = 0$ , a point charge is deposited at  $r = 0$  and the resistive layer surface is approximated to infinity radius. In this case, the solution for the charge density function is:

$$\rho(r, t) = \frac{1}{2th} \exp(-r^2/4th) \quad (2-0-21)$$

The charge density function of the resistive anode is sampled by readout pads. If the initial charge is a point charge and is localized at origin at  $t=0$ , the evolution of the 2-dimensional charge density function is as figure 2-3 [28]. The charge induced on a pad can be calculated by integrating the time dependent charge density function over the pad area.

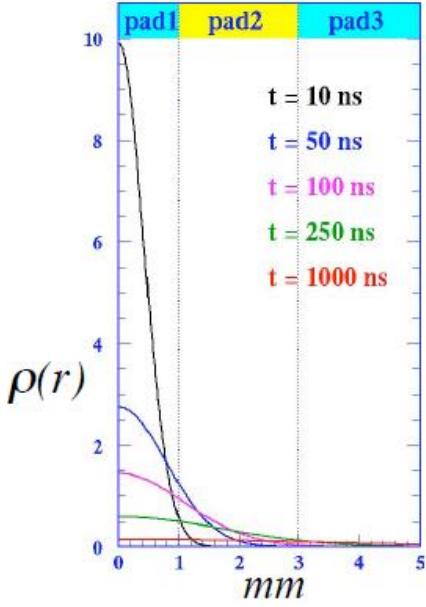


Figure 2-3. The evolution of the 2-dimensional charge density function at five different times.



## Chapter 3

# **Test-beam setup and Micromegas modules**





## 1. LCTPC collaboration and EUDET

In 2007, the Linear Collider TPC collaboration (LCTPC) was founded. The goal of the LCTPC collaboration is to unify the international efforts to build a high-performance TPC for the linear collider physics up to 1 TeV centre-of-mass energy and to provide common infrastructure and tools to facilitate these studies. The detailed description of LCTPC can be found in the LCTPC Memorandum of Agreement [29]. Updated information can be found in [30].

In the framework of the LCTPC collaboration, a Large Prototype TPC called LP-TPC was designed, built, commissioned and tested with the help of the EUDET project [31]. This prototype was developed to allow the groups forming the collaboration to test the new technologies and techniques which will be necessary to build a large TPC with the performances required by the ILD project. Towards this goal the anode endplate of the LP-TPC can be equipped with up to seven active and exchangeable readout modules, which allows testing any MPGD technology. Since 2008, it has been used in the test beam environment at DESY. In 2011, the cooling system was upgraded by adding cryo-coolers at 4 and 10 K to easily switch to the cooling, with no need to supply external liquid Helium.

The EUDET consortium (Detector R&D towards the international linear collider) provides the test beam area T24/1 at the DESY II test beam with a TPC test set up shown in figure 3-1, as a test beam infrastructure.



Figure 3-1. Large Prototype (LP) with the movable stage in the beam area.

## Test Beam

The particle beam consists of electrons and its momentum can be changed from 1 GeV/c to 6 GeV/c. The electrons emerge from converted Bremsstrahlung beam and cross a doublet of dipole magnets, which controls the energy of the beam.

Micromegas data were generally taken in two-week periods. In November and December 2008, data were taken with a standard-anode module. The drift velocity was measured and found to be consistent with the prediction from the Magboltz Monte Carlo [32]. The resolution was found to increase quickly with drift distance (faster than expected from diffusion only) and this was traced to the field inhomogeneity: at this time the magnet was fixed and the only way to change the drift distance was to slide the TPC in the magnet, so that part of the TPC was outside the region of good magnetic field. This period was used to study the signal shapes and vary the parameters of the electronics (shaping time, sampling frequency, amplifier gain), as well as to tune the Switched Capacitor Array (SCA) starting time. The electronics was based on AFTER chips from the test production of T2K. In May 2009, the same module was tested again with AFTER chips from the final T2K production, which had possibility to by-pass the shaping stage, as it was feared that the shaping would impair the long charge-sharing signals. The conclusion was that the noise was increased without any benefit. A module with Carbon Loaded Kapton (CLK) as the resistive foil was tested at the end of the month. In June, laser runs were taken to study the distortions. In October, data were taken at CERN in a high intensity pion beam with a test box which contains one module. In November, a test was performed with a silicon tracker on both side of the TPC. In December 2009, modules 4 and 5 made with a resistive carbon-loaded Kapton anode were tested without magnetic field. In March 2010, modules 2 and 3 were tested in  $B=1$  T. At this time, module 4 and 5 were also mounted at the endplate of the Large Prototype. Unfortunately, due to a design defect of the grounding, these two detectors were destroyed before data taking. In 2011, the detector made with a resistive carbon-loaded kapton layer with a resistivity of 3 Mohm/square was chosen based on the previous results, and produced using a quasi-industrial production chain. In May, this detector was tested with new integrated electronics in  $B=1$  T magnet. The new electronics worked well during test. In July 2012, six modules were tested simultaneously with  $B=1$  T magnet and all modules were connected to the high voltage with a common filter. In February 2013, seven modules which fully covered the endplate were performed at the same time without and with  $B=1$  T magnetic field. At this

time, each module was equipped with a filter. The noise was significantly reduced compared to the test which was implemented in July 2012. The main test periods are listed in table 3-1.

Test period		Module name	Module material
Nov.-Dec. 2008	test with only one module	module 1	standard anode
May 2009		module 1	standard anode
Dec. 2009		module 3	resistive CLK ~5 M $\Omega$ /□ anode
		module 4	resistive CLK ~3 M $\Omega$ /□ anode
		module 5	resistive CLK ~3 M $\Omega$ /□ anode
March 2010		module 2	resistive ink ~3 M $\Omega$ /□ anode
		module 3	resistive CLK ~5 M $\Omega$ /□ anode
May 2011		module prototype	resistive CLK ~3 M $\Omega$ /□ anode
July 2012		test with six modules	resistive CLK ~3 M $\Omega$ /□ anode
Feb. 2013	test with seven modules	resistive CLK ~3 M $\Omega$ /□ anode	

Table 3-1. Some main test periods with the test modules.

In most of the data taking periods, the beam size was measured to be 3 to 4 mm r.m.s. in both vertical and horizontal directions.

### Field cage

A schematic sketch of the LP-TPC field cage (FC) cylinder is shown in figure 3-2. It serves as a gas containment and provides a uniform electric field. The drift volume is 610 mm length and 720 mm diameter. This allows drift distances up to 59 cm to be probed.

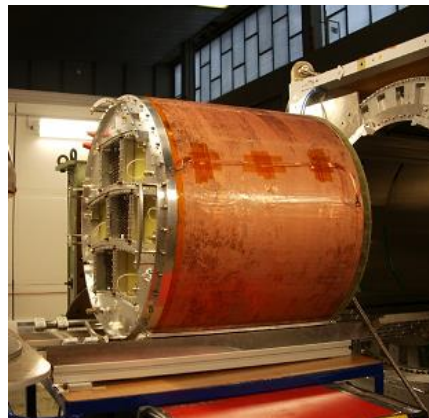


Figure 3-2. The field cage of LP-TPC.

### PCMAG

The field cage is placed in a superconducting magnet PCMAG (as shown in figure 3-1), which is provided by KEK. The PCMAG has a usable diameter of about 85 cm and a usable length of about 130 cm. It provides a magnetic field density up to 1.2 T in the central region of the magnet.

### Cosmic-ray trigger

A scintillator hodoscope is installed on the test beam setup. It can be used for detecting cosmic muon in standalone as well as in test beam mode. The hodoscope has three layers of scintillator slabs as shown in figure 3-3 [33]. On the top of the TPC, a scintillator layer including five slabs with a size of 873 mm  $\times$  175 mm for each is parallel to the TPC's axis. On the bottom, two scintillator layers are set. One layer includes three slabs parallel to the TPC's axis and one layer has four slabs perpendicular to the TPC's axis. Multi Photon Pixel Counters (MPPC) are used as the photon counting device to transform the scintillator light into electric charge. The MPPC operates at low voltage and is insensitive to magnetic fields. They are however very sensitive to variations in temperature. This disadvantage is circumvented by controlling the temperature by means of Peltier devices driven by a thermocouple.

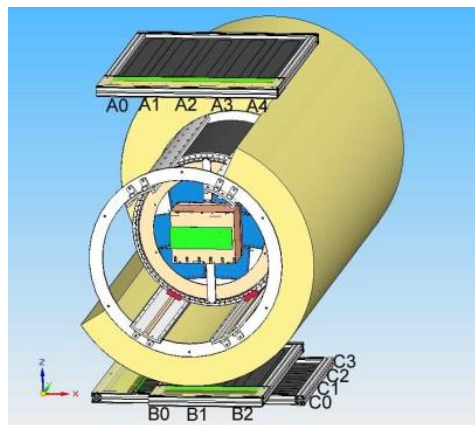


Figure 3-3. The setup of the cosmic trigger.

### Moving stage

A moving stage is mounted with TPC prototype so that it can be moved in horizontal, vertical direction, as well as rotated in the horizontal plane. The drift distance can be changed by moving the whole apparatus cage along the axis of magnet. A motor system allows the



## 2. Micromegas modules

Using the standard Micromegas technology, tests of a Micromegas TPC, which were performed at Saclay and KEK from 2002 to 2007, show that there is not enough charge spreading between the readout pads in one row with 2 mm-wide pads. The resolution was limited to 200-300  $\mu\text{m}$ . To meet the requirement of ILC, the charge dispersion technology was developed and applied for the Micromegas TPC. The principle of this technology has been introduced in Chapter 2 section 2.2.

Since 2008, up to twelve Micromegas modules have been tested as the amplification of the LP-TPC. Different materials were adopted and compared. In the first three years, five different single modules surrounded by dummy modules were tested in the center of the LP-TPC endplate as shown in figure 3-5. The electronics designed for the T2K experiment was used as the readout electronics of a single Micromegas module. After the choice of the resistive material for the anode and the module construction process, seven identical modules were equipped at the endplate of the LP-TPC as shown in figure 3-6. This fully covered the endplate of LP-TPC with Micromegas modules.

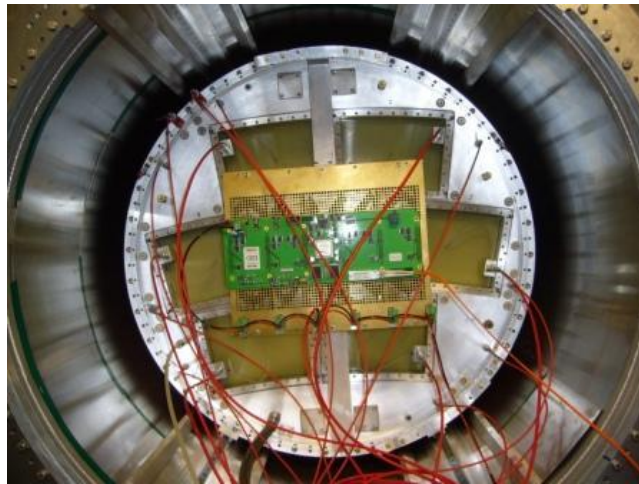


Figure 3-5. The Large Prototype with only one module installed in the center.

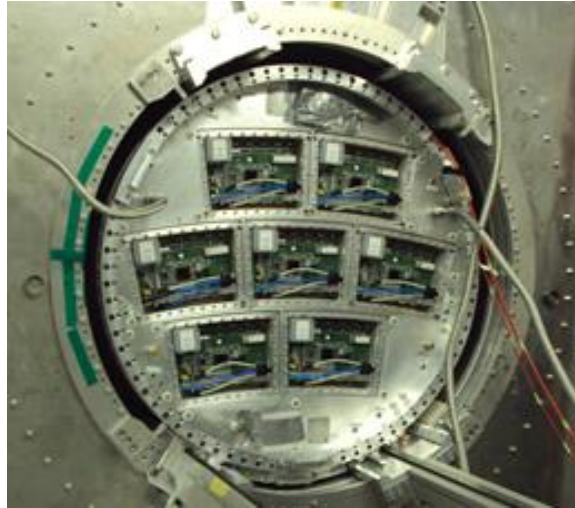


Figure 3-6. Seven identical modules mounted at the endplate of the Large Prototype.

Figure 3-7 shows the sketch of the readout pads of a Micromegas module with a typical track from the beam. A single Micromegas module is about  $22 \times 17 \text{ cm}^2$  with the pad size of  $3 \times 7 \text{ mm}^2$ . It has 1728 pads arranged in 24 rows by 72 columns. Two of them shown in an orange square rectangle in figure 3-7 are sacrificed to leave space for a high voltage connection of the mesh through the PCB. Others pads are used to read out the signal of ionized electrons. Since the module has a keystone shape, the pad width varies from 2.7 mm to 3.2 mm from inner row to outer row.

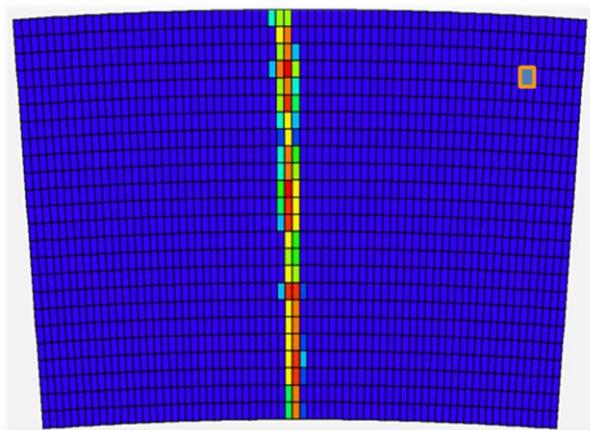


Figure 3-7. The sketch of the readout pad of a Micromegas module with a typical track from the beam.





Figure 3-8. Five Micromegas modules with different anode materials.

Figure 3-8 gives five different Micromegas modules tested in the various periods from 2008 to 2010. They are chronologically described below:

Module 1. A standard bulk Micromegas. There is no resistive layer between the mesh and anode. 128  $\mu\text{m}$  pillars are used to support the mesh. The routing of the readout pads, designed at CERN, is an eight layers PCB.

Module 2. A resistive-ink detector. There is a resistive-ink layer with a resistivity of about 3 Mohm/square covering the copper pads. Between the copper pads and the resistive layer, a 75  $\mu\text{m}$  prepreg layer is used as the insulator. All copper pads are connected all around the module to the ground.

Module 3. A resistive-kapton detector. There is a resistive carbon-loaded kapton (CLK) layer with a resistivity of about 5 Mohm/square covering the copper pads. Between the copper pads and the resistive layer, a 75  $\mu\text{m}$  prepreg layer is also used as the insulator. All copper pads are connected all around the module to the ground.

Modules 4 and 5. Two resistive-kapton detectors with a resistive carbon-loaded kapton layer with a resistivity of about 3 Mohm/square covering the copper pads. The difference between these two modules is the routing of the PCB, one designed at Saclay with a six layers PCB and one designed at CERN with an eight layers PCB. Unfortunately, these two modules were destroyed during the data taking due to a fault in the design of the grounding of the resistive layer. This was revised for the subsequent modules.

Since 2011, the resistive carbon-loaded kapton layer with a resistivity of about 3 Mohm/square is chosen as the resistive layer material and nine modules were produced using a quasi-industrial production chain. The structure of modules is shown in figure 3-9. The resistive layer is 75  $\mu\text{m}$  Dupont 100 XC10E5 resistive Kapton. A 100  $\mu\text{m}$  LF 0121 Dupont Pyralux bond ply prepreg layer is used as the insulator. But after the stacking during the manufacture process of module, the prepreg layer becomes less than 100  $\mu\text{m}$ . All copper pads are connected all around the module to the ground. To overcome the default happened in modules 4 and 5, 2.5 mm width photoresist is put between the mesh and grounding as shown in figure 3-9.

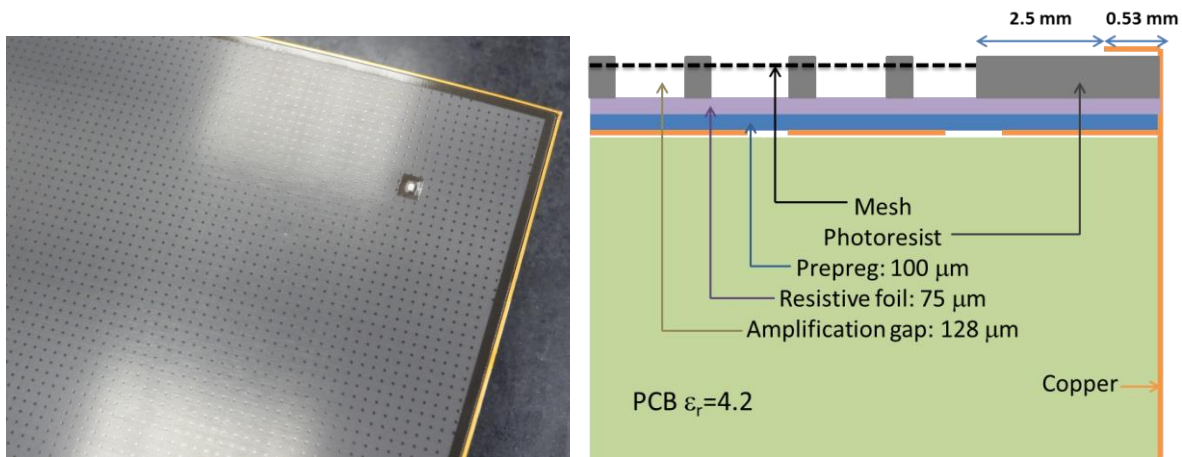


Figure 3-9. Left: Photograph of one module; Right: Structure of a module.

### 3. The AFTER chip

The AFTER chips developed for the T2K experiment are used as the readout of the Micromegas modules. A module electronics unit is composed of six Front-End Cards (FECs) linked to one Front-End Mezzanine (FEM) card directly mounted at the back of a Micromegas detector as shown in figure 3-10.

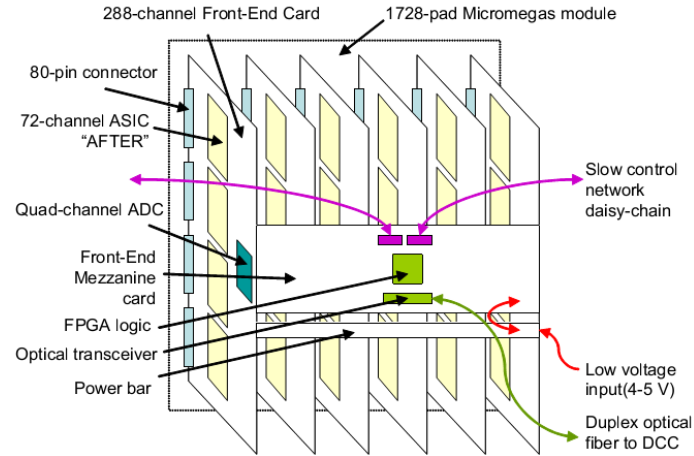


Figure 3-10. Front-end electronics of one Micromegas module [35].

A FEC includes 4 custom-made “AFTER” front-end chip (ASIC for TPC Electronic Readout) and a commercial 12-bit quad-channel ADC. The architecture of the AFTER is shown on figure 3-11. It includes 72 effective channels connected to 72 pads of the detector, and 4 dummy channels. Each effective channel includes a low noise charge preamplifier, a pole zero compensation stage, a second order Sallen-Key low pass filter, and a 511-time bin Switched Capacitor Array (SCA). Four extra similar channels are available for optional common mode or fix pattern noise rejection. The signal coming out from each SCA channel is continuously sampled and stored at the sampling rate which can be up to 100 MHz.

When a stop signal is received, the SCA state is frozen and the analog data are sequentially read and multiplexed column by column towards an external commercial 12-bit ADC. The SCA can be totally or partially read. The AFTER chip collects and filters the detector signals and samples them continuously in an analog memory, based on a SCA until an external stop signal arrives, tagging the end of the drift time. The analog data from all the channels of the chip is multiplexed towards one of the four channels of the external ADC achieving thus a first 72 to 1 data concentration. Four AFTER chips and the required external ADC are mounted on a 288-channel FEC. This scheme permits to decouple the sampling frequency and digitization and digital data treatment clock frequencies.

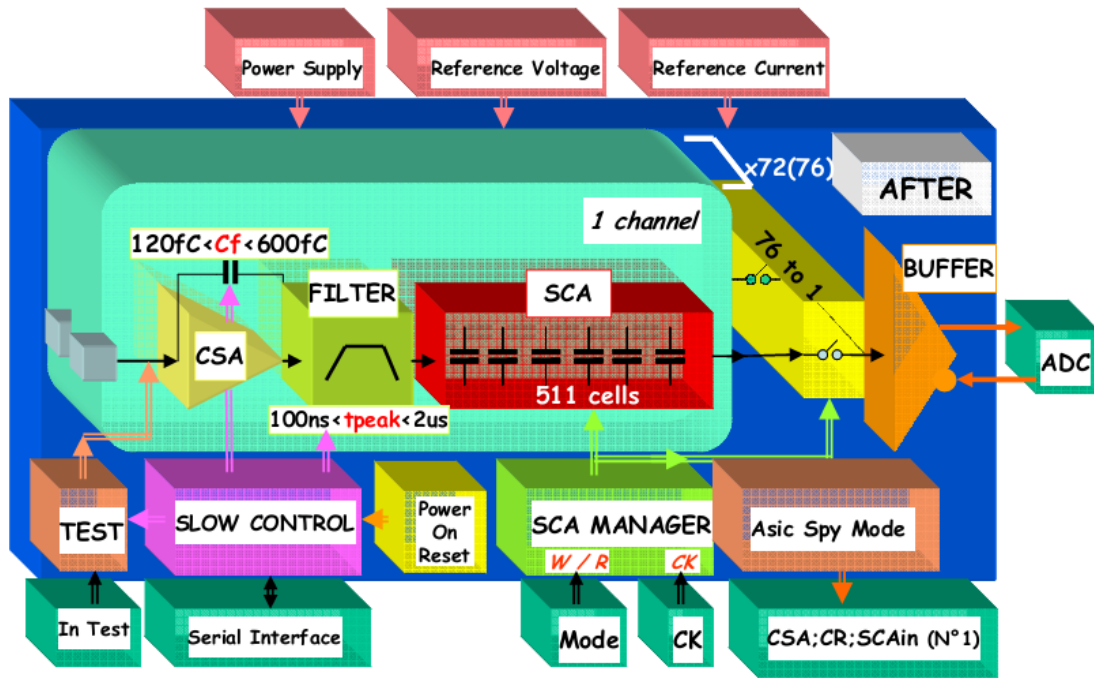


Figure 3-11. Architecture of the AFTER chip [36].

The FEM is used to gather events digitized by the six FECs of a detector module, perform optionally pedestal subtraction and zero suppression, and send data to a back-end Data Concentrator Card (DCC) through a full-duplex gigabit optical link. The 100 MHz experiment global clock, trigger information, and configuration data are sent through the return path of this optical link. The FEM board is also connected to a CAN-bus network which is used for slow control and monitoring of the operating temperature, voltage, and current of the FEM board.

Parameter	Value
Number of channels	72
Samples per channel	511
Dynamic Range	10 MIPS on 12 bits
MIP charge	12 fC to 60 fC
MIP/Noise ratio	100
Gain	120, 240, 360, 600
“Detector” capacitor range	0 pF – 40 pF
Peaking Time	From 100 ns to 2 $\mu$ s (16 values)
INL	1% range 0-3 MIPS; 5% range 3-10 MIPS
Sampling frequency	1 MHz to 100 MHz
Readout frequency	20 to 25 MHz
Polarity of detector signal	Negative or Positive
Test	1 among 72 channels or all

Table 3-2. Characteristics of the AFTER chip.

Outside the detector, the Data Concentrator Card (DCC) aggregates the data of the TPC endplates and sends event fragments to a merger computer that performs a final data reduction and communicates with the experiment DAQ system via a standard network connection.

To match various kinds of detectors and gas mixtures, this electronics offers a large flexibility in sampling frequency, shaping time, and gain as shown in the table 3-2. For instance, 4 different gains from 120 to 600 fC range are selectable to adapt the chip range to the detector gain and its shaping time and sample frequency could be chosen to match the drift time in the gas. These parameters and the control of the chip are managed by slow control, using a custom serial 4-wire link. Several test modes are available, allowing pulsing one or several channels with a known charge for test or calibration purposes.

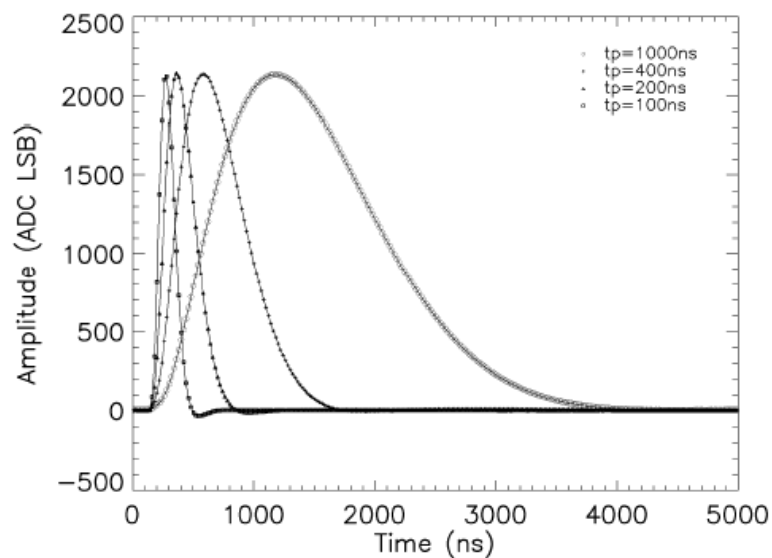


Figure 3-12. 60 fC test pulses recorded by the AFTER chip (120 fC range) for 100 ns, 200 ns, 400ns, and 1  $\mu$ s peaking times.

The electronics is more compact and has better noise and power consumption performances, thanks to the use of modern technologies. All the measured characteristics are fulfilling the design specifications. Figure 3-12 shows the response of the AFTER chip for 4 different shaping times recorded using a 50 MHz sampling frequency [37]. Figure 3-13 shows the uniformity of the Equivalent Noise Charge (ENC) for the 1728 channels and a typical map of the r.m.s. noise of the 1728 channels (24 $\times$ 72) of one detector module measured in the 120 fC range and with a 200 ns shaping time. From the r.m.s. map, we can see that there are 11 pads with blue colour which means that two pads for high voltage (row 20, column 64 and column

65) and 9 other pads are disconnected. Figure 3-14 shows the global value for the pedestal mean value and the r.m.s. value histogram for 1728 channels. During the pedestal test, the pedestal mean value of electronics was set to 250 instead of 0 which can be seen from the histogram named PedMeanGlobal. In the histogram of r.m.s. global, two peaks appear. The small peak is caused by the 4 dummy channels of each ASIC and the large peak shows the r.m.s. value of the electronics which is around 6.

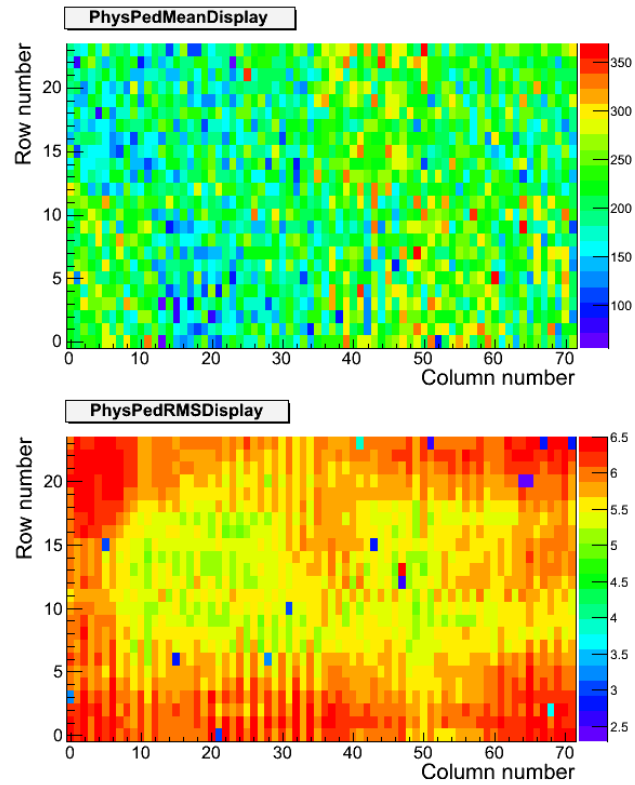


Figure 3-13. The uniformity of the ENC for the 1728 channels and a typical map of the r.m.s. noise of the 1728 channels (24×72) of one detector module measured in the 120 fC range and with a 200 ns shaping time.

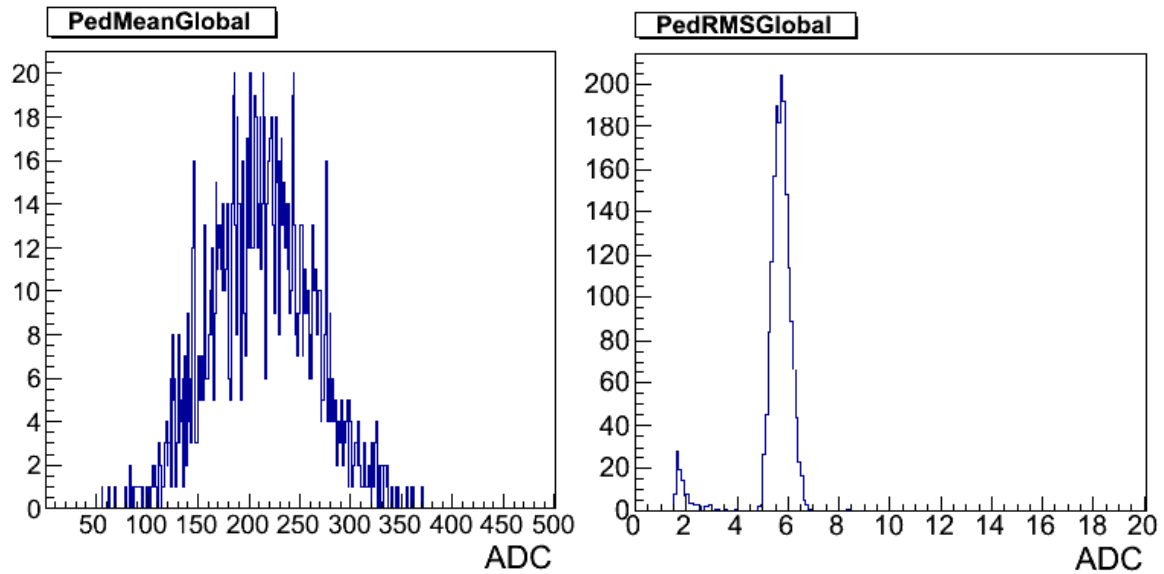


Figure 3-14. An example of the global value for the pedestal mean value and the r.m.s. value histogram of 1728 channels.

Figure 3-15 and figure 3-16 show the example of the pedestal of the electronics and r.m.s. per channel measured with a Micromegas module. In figure 3-15, each graph represents a 72-channel AFTER ASIC and totally, the electronics has 24 ASICs. In figure 3-16, each graph has at least four lower r.m.s. values. These four lower values correspond to the 4 dummy channels in each ASIC which are disconnected. For others, they are probably due to disconnected pads.

Most of the data were taken with zero suppression: the average pedestal was subtracted and remaining positive signals less than four standard deviations above the pedestal were set to zero and thus ignored in the subsequent analysis steps. In the latest data, the pedestal r.m.s. was typically 5.5 ADC counts, which places this cut at 22 ADC counts. This corresponds to 2 electrons at a gain of 2000.

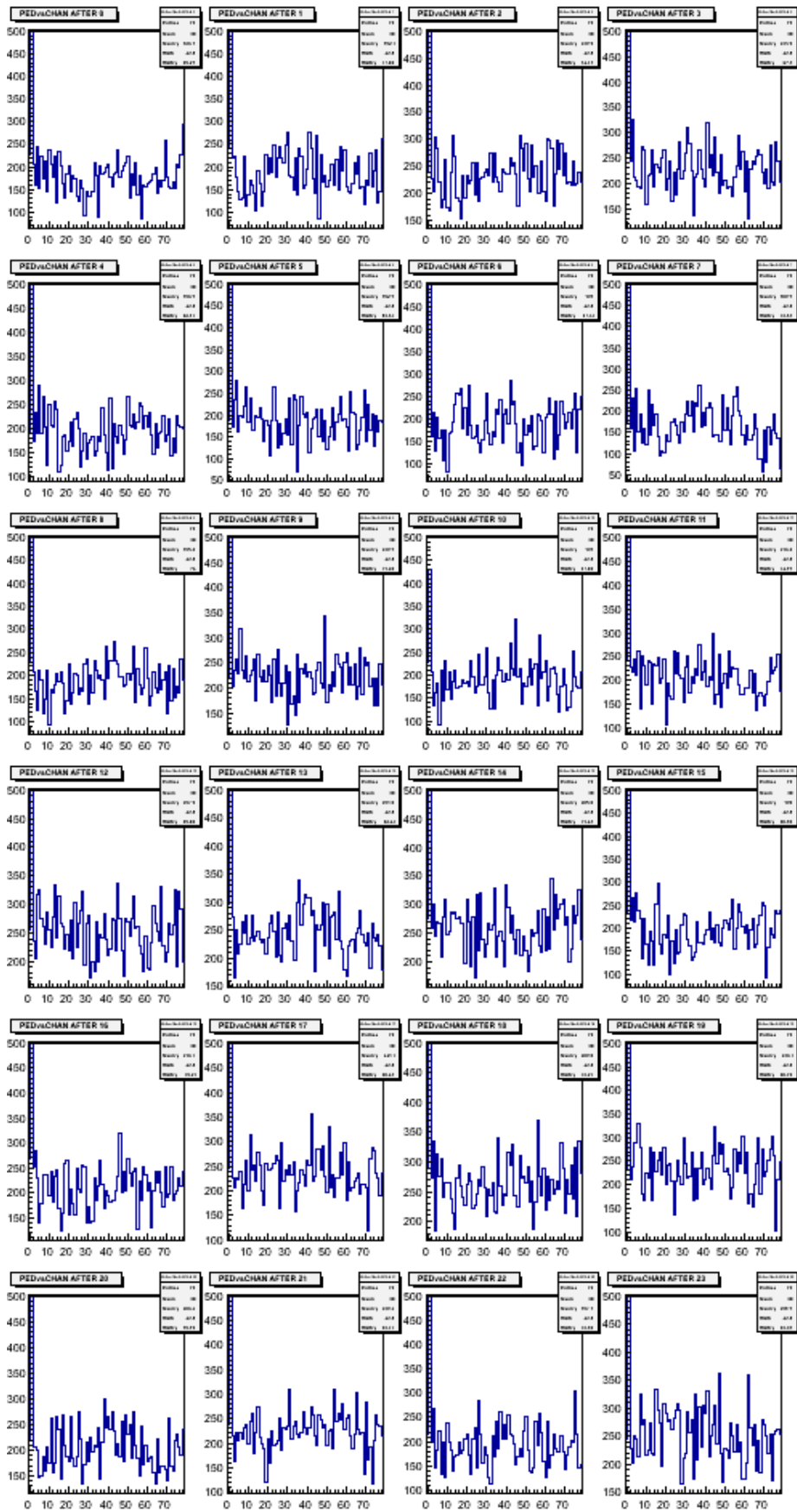


Figure 3-15. Pedestal of the electronics. Each graph represents a 72-channel AFTER ASIC.



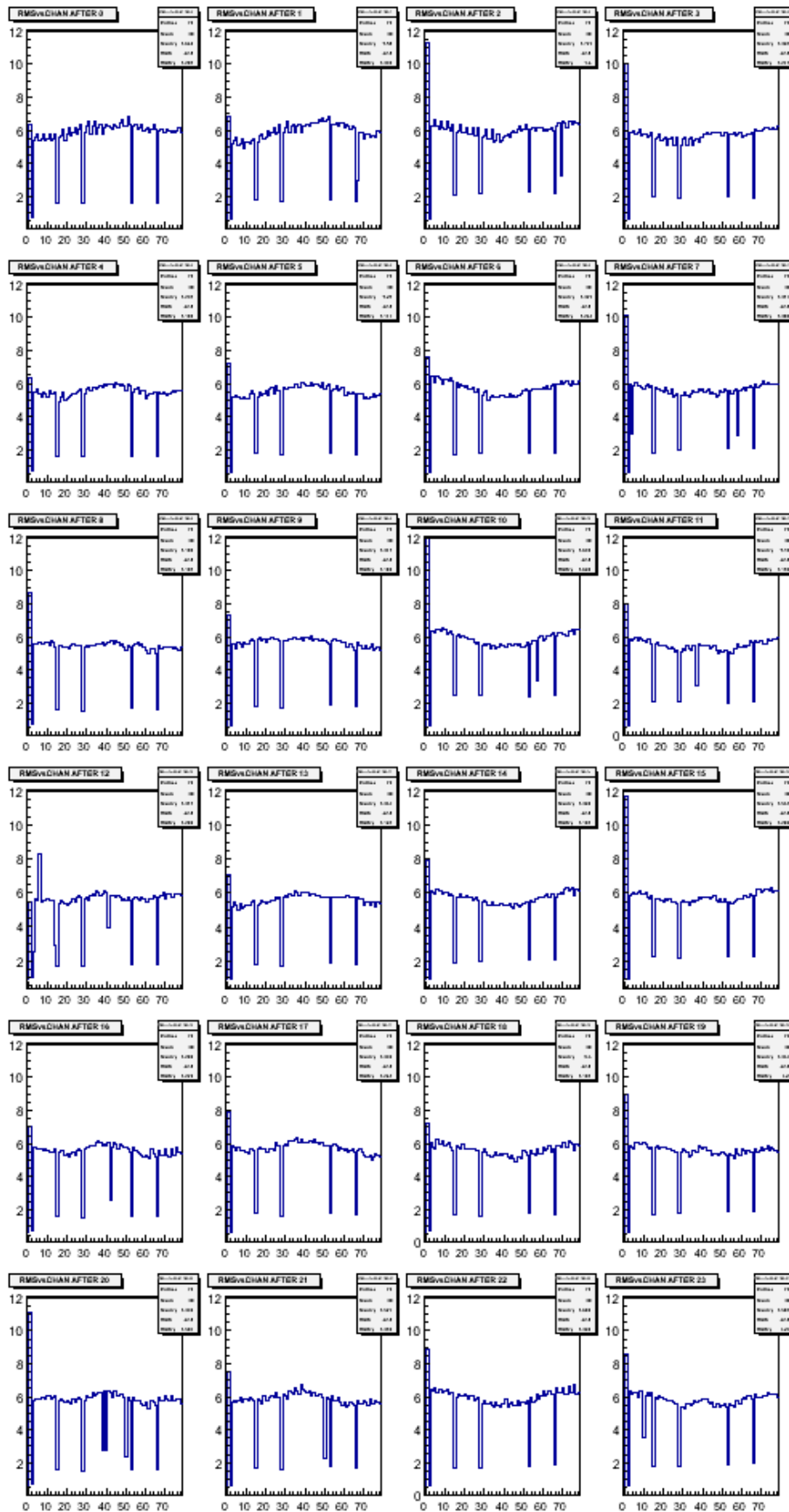


Figure 3-16. R.m.s. per channel measured with a Micromegas module.

## 4. The integrated electronics for ILC-TPC

During the test of one module mounted at the endplate of LP-TPC, the T2K AFTER electronics was used as the readout electronics as shown in figure 3-5. In this version of electronics, the size of each FEC is  $14\text{ cm} \times 25\text{ cm}$  shown in figure 3-17 on the right side. Six FEC cards are mounted at the back of a Micromegas module perpendicularly to it as shown in figure 3-5. Figure 3-17 left side shows the size of electronics for one module compared with the size of a module. Using such configuration, it becomes difficult to mount seven modules simultaneously. To reach the goal of multi-modules test, a new integrated electronics which matches the size of a module was designed.



Figure 3-17. The T2K electronics. (a) the packaging of electronics for one module test; (b) one FEC ( $14\text{ cm} \times 25\text{ cm}$ ).

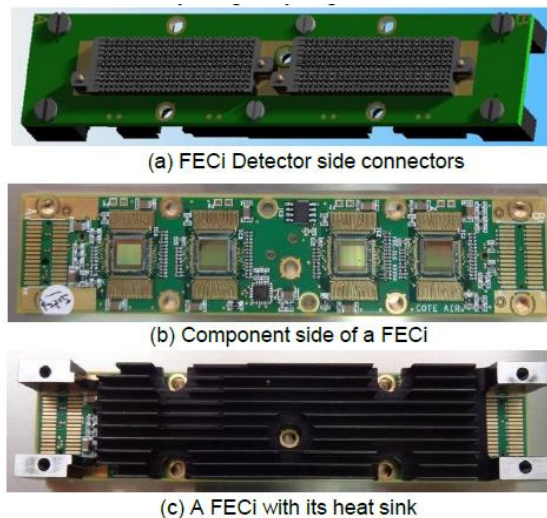


Figure 3-18. Artist view and photograph of the new FEC [38].

In order to install the electronics flat on the back of the detector, each FEC must fit in only one sixth of the area of a detector module, approximately  $125\text{ mm} \times 28\text{ mm}$ . It means that the size of the electronics is one-tenth of the T2K FEC (the number of channels is unchanged). To

meet this goal, a miniaturization of the front-end electronics and a back-end readout system with multi-module capabilities have been developed using the protection from the resistive foil. The size of the new front-end card is only  $2\text{ cm} \times 16\text{ cm}$  as shown in figure 3-18.b. Each front-end card still has four 72-channels AFTER chips. Thanks to the resistive foil, most of the protections of the electronics against sparks have been removed, such as double diodes, charge-limiting capacitors, except for current-limiting resistors. To connect the FEC to the detector module, two 300-pins grid-array solder-less connectors from SAMTEC (GFZ series) are used (as figure 3-18.a). These provide a robust, high density and low profile interconnect. Only 288 pins are connected to detector pads while the remaining 312 contacts are grounded. Six AFTER chips are digitized in parallel and four sequential iterations are needed to completely read out a detector module. Each iteration takes  $79 \times 511$  clock cycles at 20 MHz leading to an irreducible dead-time of 8 ms for complete module readout. The FEC also includes an on-board pulse for calibration and a silicon identification chip that also performs temperature, supply current and voltage measurements. An additional mezzanine card is on top with a single six-channel ADC conversion which replaces ADCs on all FEC cards. Figure 3-19 shows the split drawing of the new electronics for each layer of one module and figure 3-20 shows the new integrated electronics mounted at the back of a module.

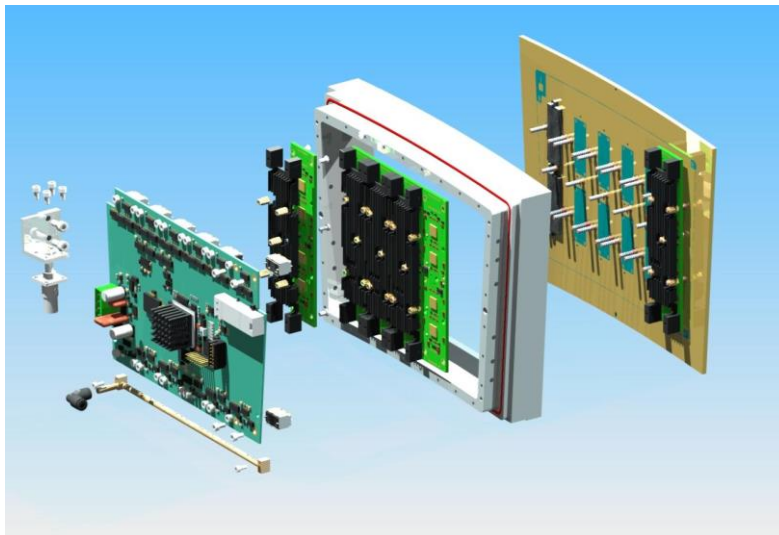


Figure 3-19. New integrated electronics split drawing of one module.

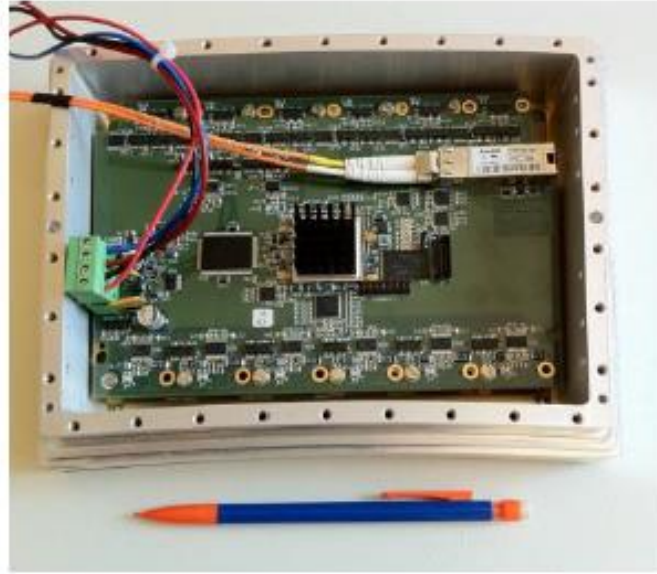


Figure 3-20. Micromegas module mounted with the new integrated electronics.

## 5. Calculation of the material budget of a module

### 5.1. Definition of the radiation length

The radiation length of a material is defined as the mean length (per cm) over which an electron loses its energy by the factor  $1/e$  by the bremsstrahlung radiation. Because of the electromagnetic field induced by the electrons of an atom, a high-energy electron will lose its energy and emit photons when it passes in the vicinity of this atom [39].

#### 5.1.1. Single element material

For most of the elements, the experimental measurement value of radiation lengths can be found in [40]. If the material is composed by a single type element, the radiation length can also be approximated by the following expression [41]:

$$X_0 = \frac{716.4 \cdot A}{Z(Z+1) \ln \frac{287}{\sqrt{Z}}} \text{ g} \cdot \text{ cm}^{-2} = \frac{1432.8 \cdot A}{Z(Z+1)(11.319 - \ln Z)} \text{ g} \cdot \text{ cm}^{-2} \quad (3-0-1)$$

where  $Z$  is the atomic number and  $A$  is its atomic weight.

#### 5.1.2. Composite materials

For most of case, the material is composed by different elements and different parts of the detector are made by different materials. The general formula for the radiation length of composite material can be calculated by:

$$\frac{W_0}{X_0} = \sum \frac{W_i}{X_i} \text{ g} \cdot \text{cm}^{-2} \quad (3-0-2)$$

where  $W_0$  is the total mass of the sample in g,  $X_0$  is the combined radiation length of the sample in  $\text{g}/\text{cm}^2$ ,  $W_i$  is the mass of the individual component in g and  $X_i$  is the radiation length of the individual component in  $\text{g}/\text{cm}^2$ .

## 5.2. The materials of one module

From figure 3-19, a Micromegas module mainly includes the following parts:

- Module frame: 450 g Aluminum (The actual mass is 938 g, but this is largely overestimated to match the thickness of a GEM module with a gating grid)
- Back-frame: 120 g Aluminum
- Detector (including SHV, Studs, PCB): 422 g mainly Silicon
- 12 ‘300-point’ connectors: 30 g (mainly plastic, say carbon)
- Each FEC (totally 6 FECs): PCB 20 g Silicon, radiator 24 g Aluminum, 4 screws 45 g mainly iron
- FEMI: 170 g Silicon
- Stud screws: 24 g in total
- Air cooling: 140 g (of which 12 g brass, rest is Plexiglas)

## 5.3. Average thickness in radiation length of a module

Base on the above materials of a module and equation 3-0-2, the average radiation length of a module with the size approximated to  $22 \times 17 \text{ cm}^2$  rectangle can be calculated. The result and the radiation length of each composition are listed in table 3-3.

		M (g)	Radiation Len. ( $\text{g}/\text{cm}^2$ )
Module frame + Back-frame + Radiator ( $\times 6$ )	Al	714	24.01
Detector + FEC PCB ( $\times 6$ ) + FEMI	Si	712	21.82
12 ‘300-point’ connectors	Carbon	30	42.70
screws for FEC + Stud screws	Fe	294	13.84
Air cooling	brass	12	12.73
	Plexiglas	128	40.54
Average of a module		1890	21.38

Table 3-3. Radiation length of the materials of a module.

The average thickness in radiation length of a module can be calculated as following:

$$\frac{d}{X/\rho} = \frac{W/\rho S}{X/\rho} = \frac{W}{XS} = \frac{1890}{21.38 \times 17 \times 22} = 0.236.$$

where  $d$  is the thickness,  $S$  is the surface size,  $\rho$  is the average density,  $W$  is the total mass, and  $X$  is the radiation length in units of  $\text{g}/\text{cm}^2$  for a module.

From the above results, the material budget of a Micromegas module is less than 25% of a radiation length which meets the requirement of the endplate of the TPC.

## 6. Towards the ILD TPC

The ILD-TPC is a large cylinder designed with a diameter of the inner field cage of 65 cm, of the outer field cage of 360 cm and a central cathode, which divides the TPC into two equivalent volumes with a drift distance up to 215 cm in a large magnet operating at 3.5 T. The tolerance is about 300  $\mu\text{m}$  for the alignment of the field cage axis and 450  $\mu\text{m}$  for the parallel alignment of anode and cathode. The material budget of the wall is 1%  $X_0$  for the inner field cage and 5%  $X_0$  for the outer field cage. The field cage has to be lightweight as well as a high mechanical precision. The design of the final ILD-TPC has also been started, with considering of the surrounding detectors, including mounting structures and spaces for supplying lines and cables. Some examples of the model for the ILD-TPC are shown here. Figure 3-21 (a) shows the design using Micromegas as the amplification system. Each endplate has 80 modules with 8000 pads. The wide pad size of about  $3 \times 7 \text{ mm}^2$  is used. Figure 3-21 (b) shows the design using GEM as the amplification system. Each endplate has 240 modules arranged in 8 layers.  $10^6$  pads are foreseen for each endplate with a pad size of about  $1 \times 6 \text{ mm}^2$ .

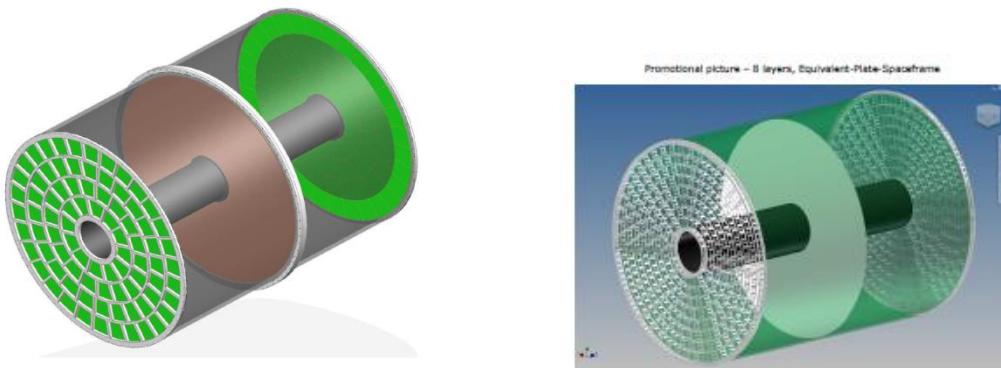


Figure 3-21. (a) An example of a model using Micromegas as the amplification system for the ILD-TPC; (b) An example of a model using GEM as the amplification system for the ILD-TPC [42].



## Chapter 4

# **Test bench of Micromegas modules**





To calibrate and characterize the energy resolution and uniformity of each Micromegas detector module, a test-bench has been built and was operated in a clean room at CERN. The test-bench was built for the T2K experiment in 2007 and adapted to our modules by us in 2011~2012. The goal of the test-bench is to study the following characteristics of the readout modules one by one: response of the pads to the source, energy resolution, gain, and stability with time.

## 1. Introduction of the test-bench

Figure 4-1 shows the test-bench setup. The tested module is held in a vertical plane in a  $33 \times 36 \times 4$  cm<sup>3</sup> gas-tight box. The gas box is a small drift chamber providing 4 cm long drift region and made in G10 FR-4 glass epoxy composites. One side is equipped with one module under test and the other side is a cathode. An aluminized mylar sheet is used as cathode and supported by a grid in G10 to ensure the uniformity of the drift field. The grid ensures the flatness of the cathode to avoid any torsion. The <sup>55</sup>Fe source is put in an aluminium collimation tube and fixed on a set of two mechanical arms as shown in figure 4-2. It is located behind the cathode of the gas box. By moving the mechanical arms, the source can be shifted in X or Y direction for the scanning of the different active surface of the detector. During the calibration, the T2K gas (Ar:CF<sub>4</sub>:iC<sub>4</sub>H<sub>10</sub> =95%:3%:2%) was used as the gas mixture. All tests were operated at atmospheric pressure and room temperature.

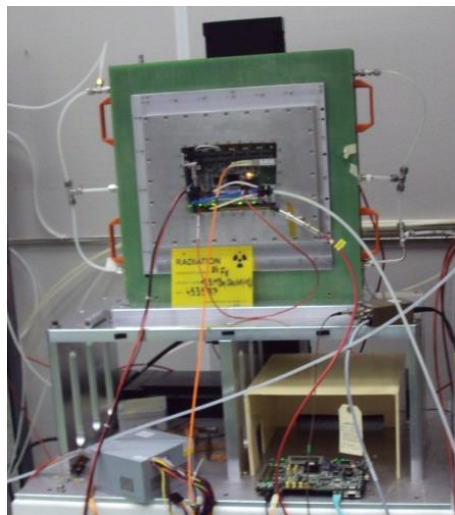


Figure 4-1. The setup of the test bench.

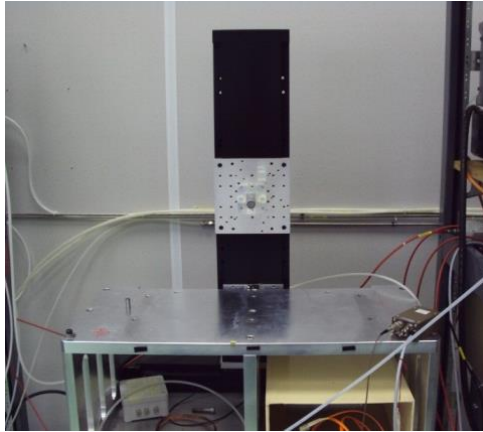


Figure 4-2. The set of two mechanical arms which holds the  $^{55}\text{Fe}$  source.

## 2. Structure of the test bench

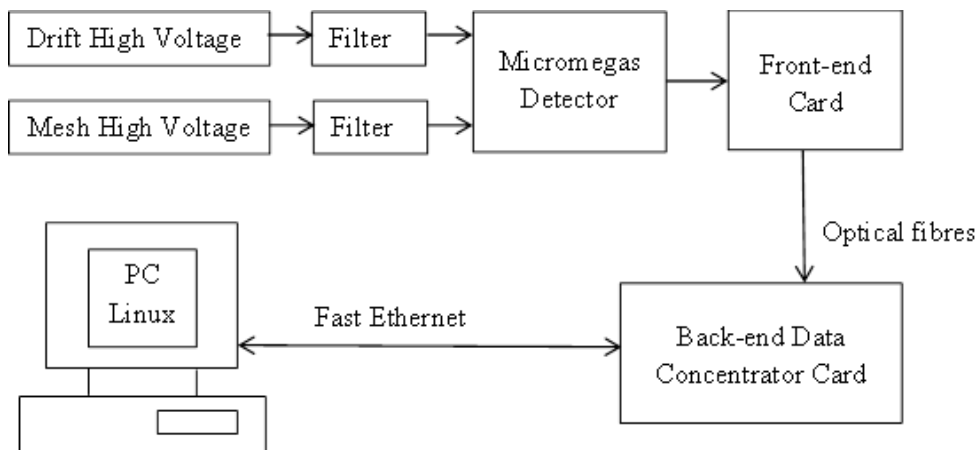


Figure 4-3. The structure of the test bench.

Figure 4-3 shows the set-up of the test bench. The drift high voltage and mesh high voltage were connected to the drift electrode and mesh electrode respectively. The signal was collected by the PCB and read out by the Front-end Card. The new integrated AFTER-based electronics was used to read out the pad signal. It is flat at the back of the detector. By an optical fibre, the FEM card of electronics was linked to an off-detector data concentrator card (DCC), then controlled by a PC running under a Linux system. Using this new integrated electronics, the pedestal can be taken in two ways. One way is same as the normal T2K electronics, the pedestal data are saved on the PC. Another way is to keep the pedestal information in the memory of the electronics. In the first way, we can re-read the pedestal information anytime when we need. In the second way, there is no pedestal data saved on the PC. This saves a lot of disk space, but the pedestal information will be lost when the

electronics is switched off/on and it requires to re-do the pedestal calibration. At the same time, the temperature of electronics can be monitored during data taking to prevent damage to the electronics.

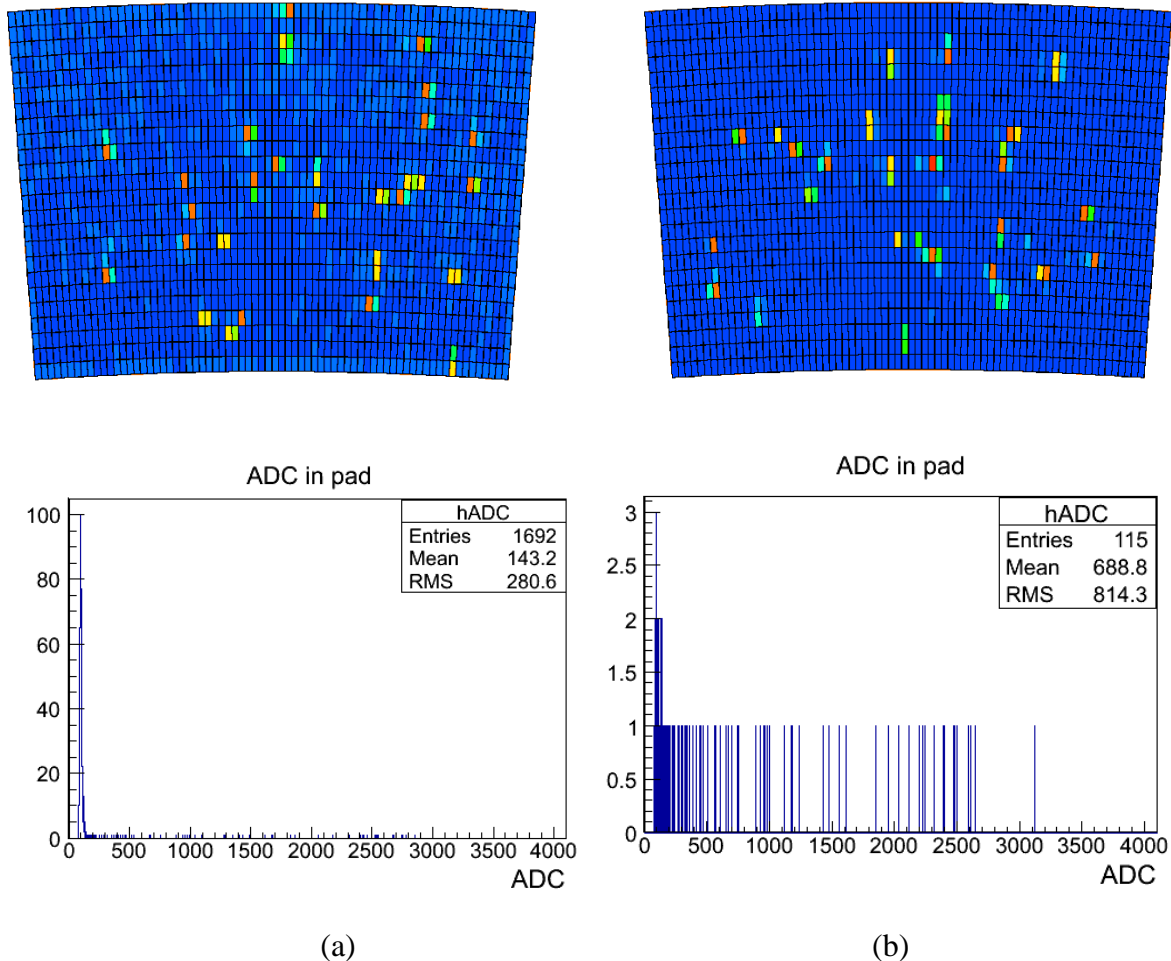


Figure 4-4. The display of events using X-rays of  $^{55}\text{Fe}$  source and the corresponding histogram of each pad's ADC. (a) Before the filter was added between high voltage and mesh electrode; (b) After the filter was added between high voltage and mesh electrode.

To reduce noise, high pass T filters were added between high voltage and detector. In figure 4-4, (a) shows a display before the filter was added between mesh and high voltage, (b) shows a display with the filter added. There are 1692 pads recording signal and most of pads have less than 100 ADC in the histogram of figure 4-4 (a). Compared with (a), only 115 pads record signal in (b). The lower ADC signals are filtered and the noise is reduced.

During our data taking, the second way of the pedestal recording was used. Each time, when the electronics was switch on/off, the pedestal recording was redone. After the pedestal recording, the drift voltage was set at 860 V and the mesh voltage was set at 380 V during

data taking. The amplification gap of our module is 128  $\mu\text{m}$  and the drift gap of the gas box is 4 cm. For each detector module, the data were taken in two situations as shown in figure 4-5: with a  $^{55}\text{Fe}$  source collimated using a collimator and with a  $^{55}\text{Fe}$  source without collimator. With collimator, the spot of X-rays is limited to 2-6 pads and the gain and energy resolution of the detector are studied. Without collimator, the X-rays of  $^{55}\text{Fe}$  source could cover the whole detector for a full scan, so that the maps of disconnected pads and dead pads can be done. Using the display programme, the measurements were monitored during data taking.

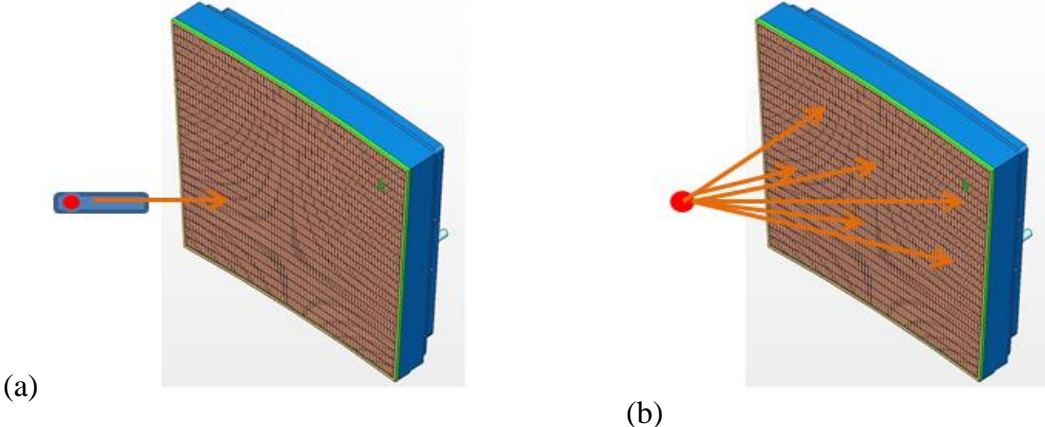


Figure 4-5. (a) Collimated source ( $^{55}\text{Fe}$ ); (b) Source ( $^{55}\text{Fe}$ ) without collimator.

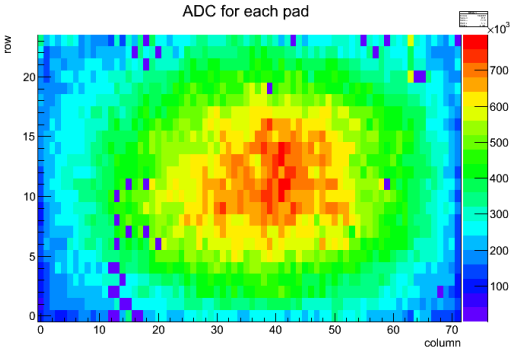


Figure 4-6. The map of disconnected pads in one of the modules. The disconnected pads are in dark blue.

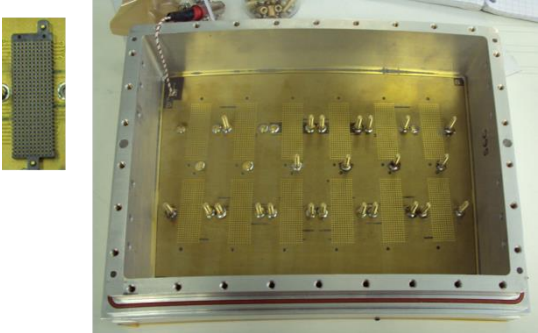


Figure 4-7. Mechanical problem: some studs de-soldered.

By integrating the ADC of all events in each pad, the disconnected pads or dead pads could be checked. Figure 4-6 shows an example of the map of disconnected pads. A pad coloured in dark blue in the map means there is no charge collected in it. This module has about 30 pads disconnected, in addition to two pads space for passing the connection of mesh voltage. This is caused by a mechanical problem. The 300-pins connector (shown in the left of the figure 4-7) between the PCB and the readout electronics is fixed by the pressure of the radiator, and the radiators are fixed by the threaded stud which is soldered on the PCB. Unfortunately, the soldered stud is not easy to fix firmly to the PCB. If some soldered studs are not well welded (as shown in figure 4-7), connections are lost between detector PCB and FECs. This caused some pads signal missing. These disconnected pads will be recovered by re-solder the soldered studs. During the test, the detector and electronics worked well and no ASIC was lost, demonstrating the valid protection of the resistive film.

### 3. $^{55}\text{Fe}$ energy spectrum

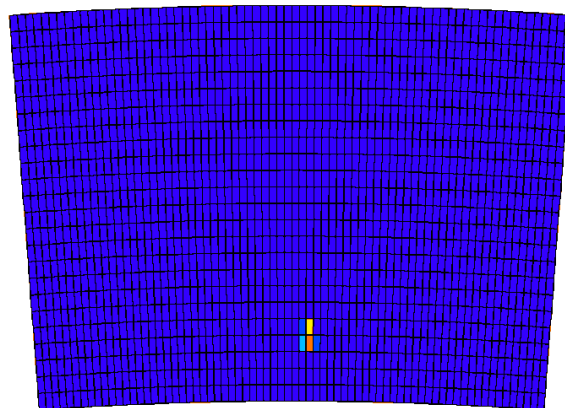


Figure 4-8. An example of X-rays event tested with collimator.

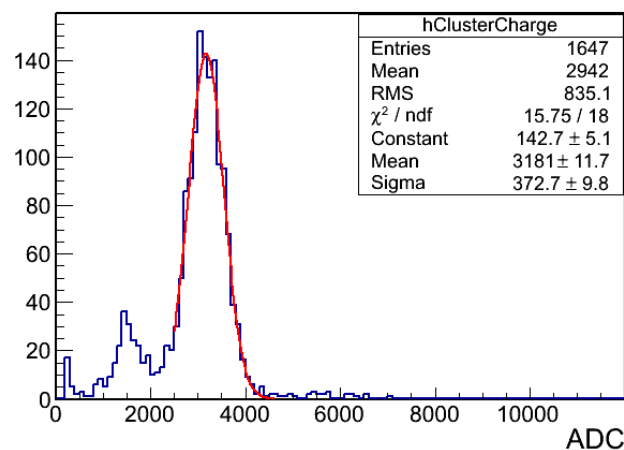


Figure 4-9.  $^{55}\text{Fe}$  energy spectrum.

By moving the mechanical arms, the  $^{55}\text{Fe}$  source is kept at different distances to the cathode. Since the collimator limits the number of illuminated pads, the X-rays spot is about 2-6 pads as shown in figure 4-8. To get the energy spectrum, each spot is looked as one cluster. To get the cluster's charge, each pad's maximum ADC is counted to get the sum ADC of pads in one cluster. Then the cluster's charge is filled into one histogram as figure 4-9. The 3 keV Ar escape peak is well separated from the 5.9 keV  $^{55}\text{Fe}$  X-ray. Using a Gaussian fit, the mean value is at 3181 ADC channel and the energy resolution is 12%. The best energy resolution obtained for a bulk Micromegas detector is 7% r.m.s., but there is no resistive layer applied. During data taking, 120 fC electronics gain is used and 1 fC has 6242 electrons. The full scale of ADC is 4096. The average number of ionized electrons induced by 5.9 keV photon in Argon is 234. Then the gain can be calculated as:  $(3181 \times 120 / 4096) \times 6242 / 234 \approx 2486$ .

## 4. Stability

To study the stability of the gain and the energy resolution of the detector, one of the modules had taken data for over 16 hours with collimated source at room temperature and atmospheric pressure. In figure 4-10, the left plot (a) shows the distribution of gain and the right plot (b) shows the gain as a function of time. In figure 4-11, the left one (a) shows the distribution of energy resolution and the right one (b) shows the energy resolution as a function of time. In figure 4-10 (b), the gain increases with time at the beginning and then keeps stably about 2500 at  $V_{\text{mesh}}=380$  V. This is caused by the presence of oxygen in the gaseous mixture at the beginning of data taking. The energy resolution varies between 11.5% and 13.5%.

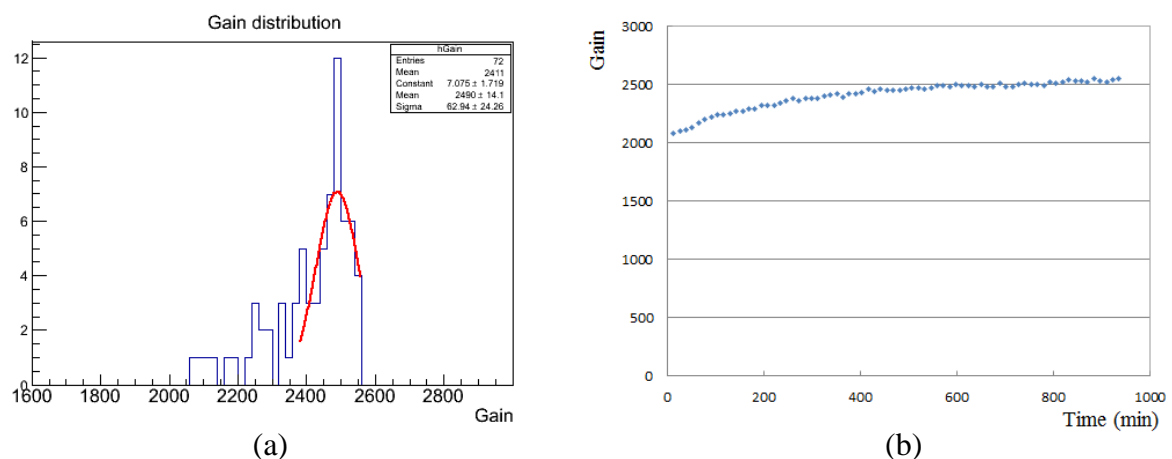


Figure 4-10. Left: the distribution of gain over 16 hours. Right: the gain of the detector as a function of time.

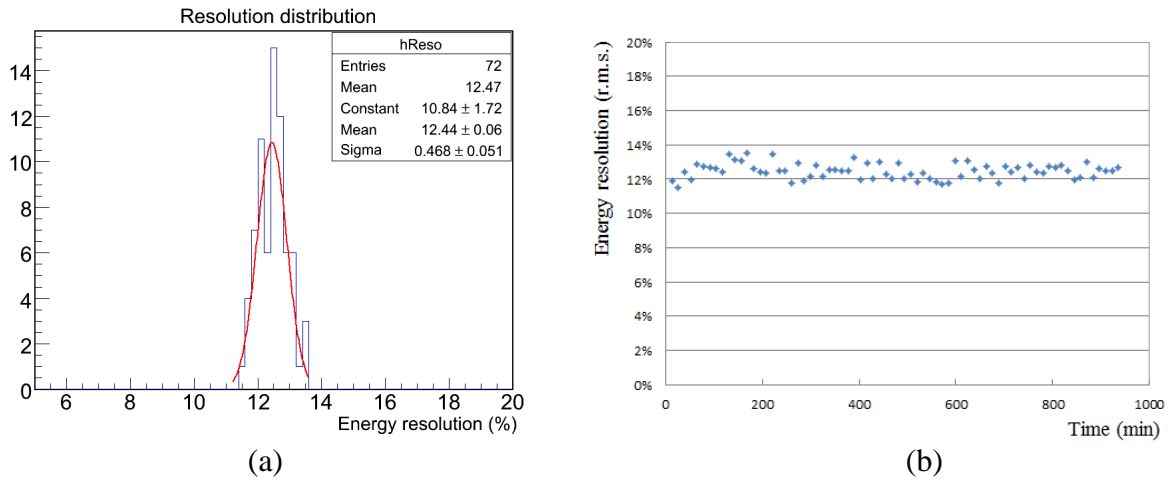


Figure 4-11. Left: the distribution of energy resolution over 16 hours. Right: the energy resolution as a function of time.

## 5. Module comparison

Figure 4-12 shows the energy resolution and the gain of seven of the modules. One point is corresponding to one module. The energy resolutions for different modules are around 12% and the average gain is about 2630 at  $V_{\text{mesh}} = 380$  V. The spread between modules is around 15%. The results show that the characteristic between different modules are similar. This demonstrates that the effectiveness of the quasi-industrial production chain.

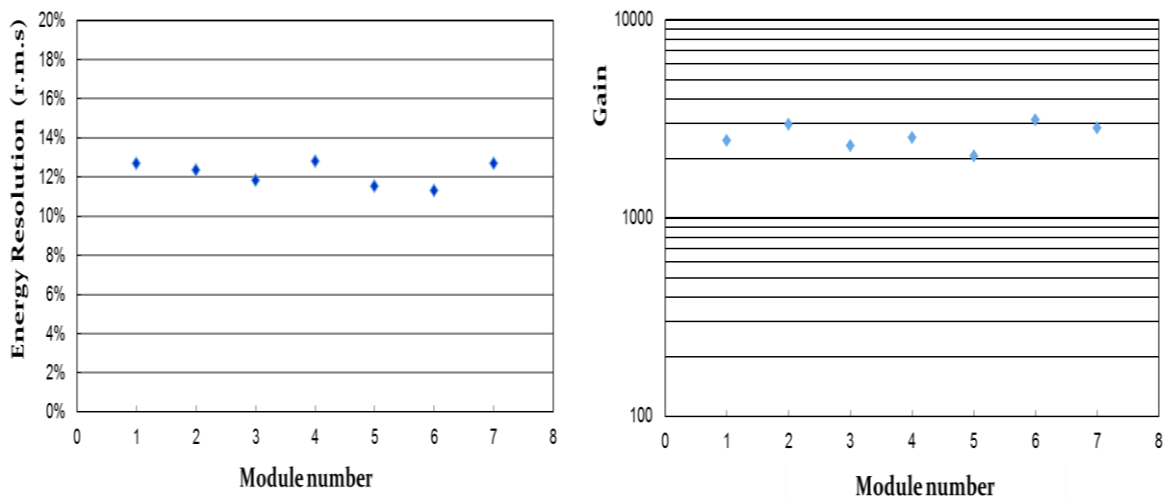


Figure 4-12. Energy resolution and gain for different modules.





Chapter 5

**Ion backflow measurement**



In a TPC, ions produced in the amplification gap can slowly flow back to the cathode. This creates a space charge which distorts the drift electric field. It is very important to limit this backflow to some level. This backflow fraction reaches 20-30% in the case of a wire chamber [43]. In some TPC experiments, such as ALEPH, STAR, ALICE, a gating grid was used to stop most of the secondary ions near the endplate. The structure of a Micromegas detector has the intrinsic property to stop a large fraction of the secondary positive ions produced in the amplification gap on the mesh. This has been studied using a standard Micromegas with 50  $\mu\text{m}$  amplification gap [44] or integrated grid Micromegas detectors [45] in the P10 gaseous mixture (90% Ar+10% CH<sub>4</sub>). In this chapter the ion backflow (IBF) suppression capability of the bulk Micromegas is investigated. The charge gain, the energy resolution and the IBF were measured using a <sup>55</sup>Fe source or an X-ray gun.

## 1. Experimental setup

A bulk Micromegas detector was used to investigate the ion backflow. It has 128  $\mu\text{m}$  amplification gap and 1 cm drift gap with a 18  $\mu\text{m}$  thick 400 Lpi (lines per inch) woven micromesh. The T2K gas was used as the gaseous mixture same as the LP-TPC gaseous mixture. All the measurements were performed at the room temperature and atmospheric pressure.

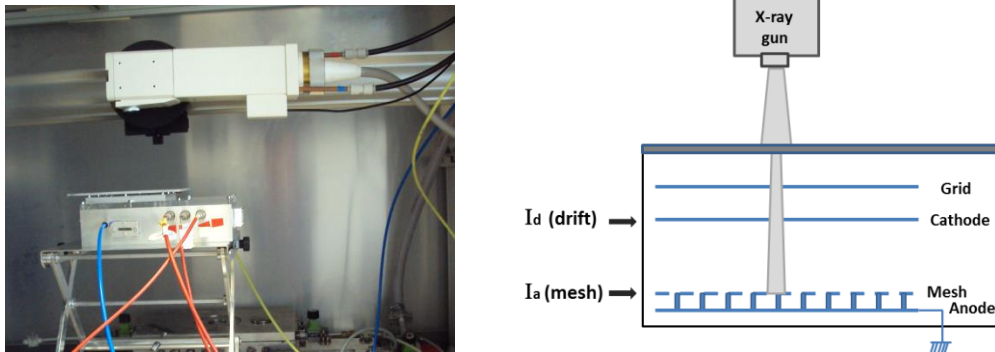


Figure 5-1. Experimental device (left hand) and schematic diagram of the set up (right hand) for the ion backflow measurement.

An intense X-ray gun (model XRG 3000) was used to produce primary electrons. The anode of the detector was non-segmented and grounded. The mesh and cathode were respectively set with negative high voltage provided by the CAEN model N471A power supply. Currents on the mesh and cathode were directly monitored by the power supply. To avoid a current to be created between the shielding box of the detector and the cathode, a grid was put 3 mm above

the cathode and set to the same high voltage as the cathode. The experimental device and the schematic diagram of the setup are shown in figure 5-1.

## 2. Characteristics of the bulk Micromegas detector

The characteristics of the bulk Micromegas detector, such as gain, energy resolution, electron transparency were firstly measured using a  $^{55}\text{Fe}$  source. The signal was read out from the mesh through a pre-amplifier (ORTEC Models 142B), spectroscopy amplifier (ORTEC models 472A), and a digital multichannel analyser (MCA 8000A Pocket), then recorded by a computer. A thin Chromium-foil was used to filter the high energy photon ( $K_\beta$ ) from the  $^{55}\text{Fe}$  source and keep the 5.9 keV photon.

### 2.1. Gain

Figure 5-2 displays the gain as a function of the mesh voltage. In the measurements, the drift electric field was kept constant at  $E_{\text{drift}} = 0.2$  kV/cm. The gain increases with the applied voltage on the mesh and reaches around 2000 for  $V_{\text{mesh}} = 380$  V.

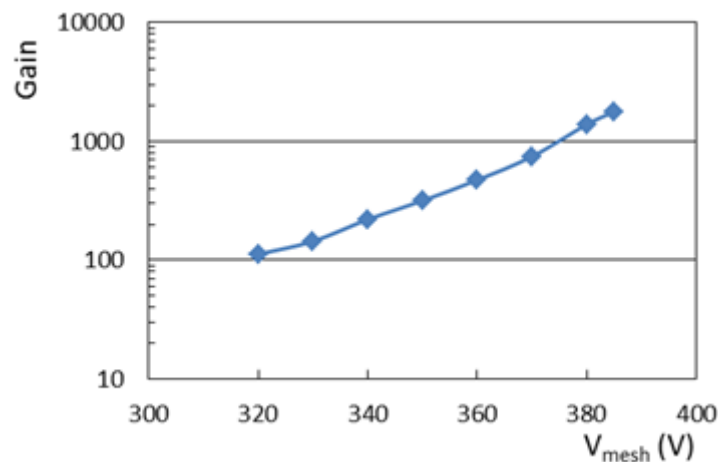


Figure 5-2. Gain as a function of  $V_{\text{mesh}}$  for  $E_{\text{drift}} = 0.2$  kV/cm at atmospheric pressure.

### 2.2. Energy resolution

The energy resolution is calculated from the r.m.s. of the peak position distribution according to the following equation:

$$E_{\text{Reso}} = \frac{\sigma_P}{P}$$

A typical measured  $^{55}\text{Fe}$  spectrum is shown in figure 5-3. A Gaussian and a linear function were used to fit the photo-peak and the background.

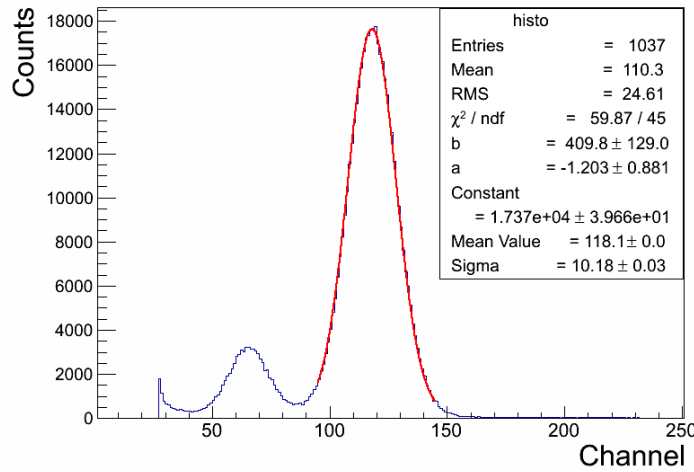


Figure 5-3. Measured  $^{55}\text{Fe}$  spectrum in a T2K gaseous mixture at  $V_{\text{mesh}} = 350 \text{ V}$  and  $V_{\text{drift}} = 400 \text{ V}$ .

The trend of the energy resolution was investigated with various drift electric fields at a fixed mesh voltage  $V_{\text{mesh}} = 350 \text{ V}$ . The results are shown in figure 5-4. The energy resolution degrades by more than 10% when the ratio of  $E_d/E_a$  is larger than 0.01. The first point at low drift field is for  $E_d=14 \text{ V/cm}$  where recombination is likely to happen.

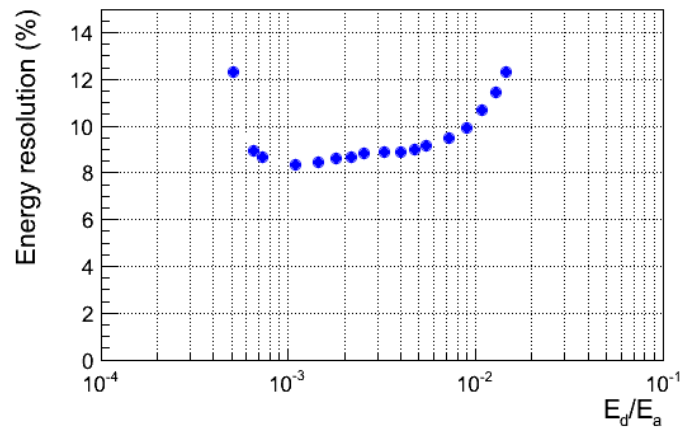


Figure 5-4. Energy resolution as a function of the ratio of  $E_d/E_a$  ( $E_d$ : drift electric field;  $E_a$ : amplification electric field).

### 2.3. Electron transparency

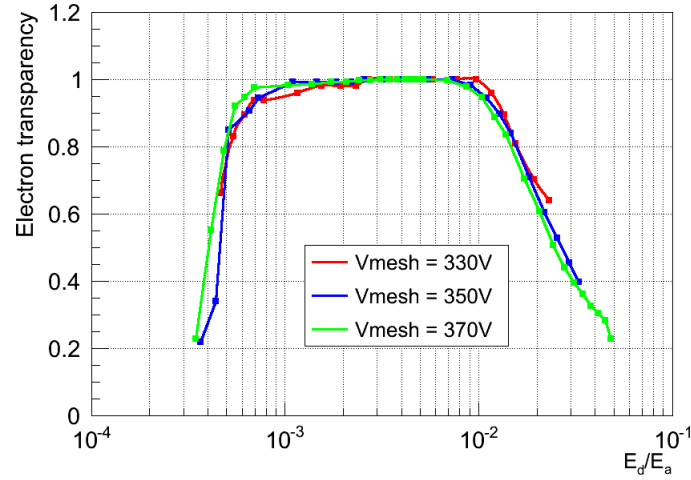


Figure 5-5. Electron transparency as a function of the ratio of  $E_d/E_a$  in the T2K gas mixture (normalized to unity).

Figure 5-5 shows the electron transparency as a function of the ratio of  $E_d/E_a$ . Here the electron transparency has been normalized to unity. To measure the electron transparency, the mesh voltage was fixed at a given value and the drift electric field was changed. Because of the electric field, the primary electrons created by ionization in the drift gap transfer through the mesh and avalanche at the amplification gap. If the drift electric field is too low to separate efficiently the electron-ion pairs in the gas, some of them will recombine. If the drift electric field is too high compared with the amplification electric field, the primary ionization electrons cannot effectively pass through the mesh, the electron transparency will become low. Figure 5-5 shows that the field ratio of  $E_d/E_a$  has to be less than 0.01 to obtain full electron transmission through the mesh. For different mesh voltages, the range of  $E_d/E_a$  for the full electron transparency also slightly changes.

The working point at the ILC will probably be  $E_d=230$  V/cm or less and  $E_a=30$  kV/cm (corresponding to 380 V on the mesh) which gives  $E_d/E_a \sim 0.0077$  and is on the plateau.

### 3. Ion backflow measurements

To measure the ion backflow, an intense X-ray gun was used to produce primary electrons in the drift gap. The voltage on the mesh was kept constant. The field ratio of the drift electric field to the amplification electric field was changed by changing the voltage on the drift electrode. Currents on the cathode and mesh were monitored. The ion backflow represents the

fraction of the secondary ions created in the amplification gap that drift into the drift gap, and then are collected by the cathode. It can be calculated according to the following equation:

$$IBF = \frac{I_a - I_p}{I_a}$$

where  $I_d$  and  $I_a$  are respectively the currents collected on the cathode and mesh,  $I_p$  is proportional to the number of primary ionized ions in the drift gap and is equal to the cathode current without amplification applied in the amplification gap.

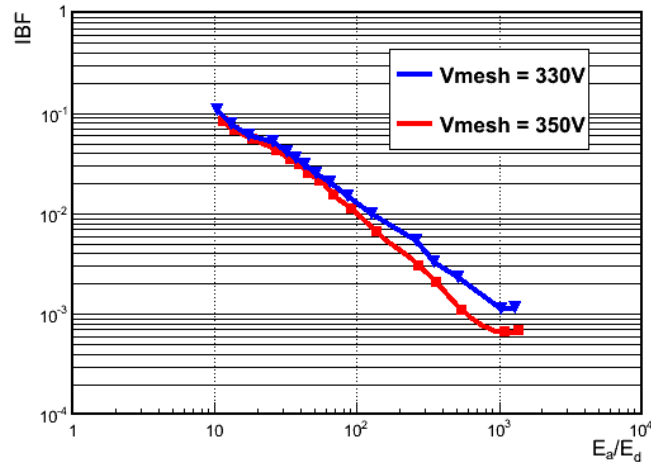


Figure 5-6. Ion backflow as a function of the field ratio of  $E_a/E_d$ .

Figure 5-6 shows the ion backflow as a function of the field ratio of  $E_a/E_d$  at  $V_{\text{mesh}} = 330\text{ V}$  and  $V_{\text{mesh}} = 350\text{ V}$  respectively. The measurement results show that the ion backflow is an inverse function of the field ratio between the amplification and the drift electric fields, and decreases faster at higher mesh voltage but this may be an effect of space charge. For our Micromegas modules tested in LP-TPC, the field ratio is set around 200. The ion backflow will be of the order of  $3 \sim 6 \times 10^{-3}$ . All these results are consistent with the measurement results with a standard Micromegas in [44].





Chapter 6  
**Analysis software**



## 1. Introduction

The data taking provides us with events characterized by a collection of pads, each of which bears a signal above the noise. The signals are sampled at a given frequency (by default 25 MHz) and the amplitude is given as a function of time in ADC counts. The pulses are shaped so that the pulse height is proportional to the charge collected by the pad. The charge deposited on a given pad and the time of this deposition are taken to be the maximum of the pulse and the time of this maximum. So, each pad above the threshold contains a charge and time information, and its position is given by two coordinates.

The role of the software is to reconstruct 3D tracks among these collections of pads. From these tracks various aspects of the detector performance are obtained: the r.m.s. of the residuals measures the resolution, the average residuals signal distortions, the charge deposited on the pad row gives the particle energy loss, and the track curvature in the magnetic field allows the momentum to be measured.

## 2. PRF (Pad Response Function)

In the standard Micromegas or bulk technology, the charge is spread among pads due to the diffusion in the gas. A Gaussian fit can thus be used to determine the hit position. In the charge dispersion technology, the charge is spread on the neighbouring pads by a resistive-capacitive layer. A more general function has to be used to describe the charge distribution, the pad response function (PRF). The PRF expresses the relation between the charge fraction deposited on a pad and the relative position of the pad to the position of a track parallel to the long side of a pad. The width of the PRF is an important parameter to study the spatial resolution of a TPC. Figure 6-1 gives an example of PRF fitting for different drift distances ( $z$ ). Because the diffusion of ionization electrons increases with the drift distance, the charge signal is collected in more pads after longer drift distance. The width of PRF increases with the drift distance. In the last years, different expressions were adopted for the PRF.

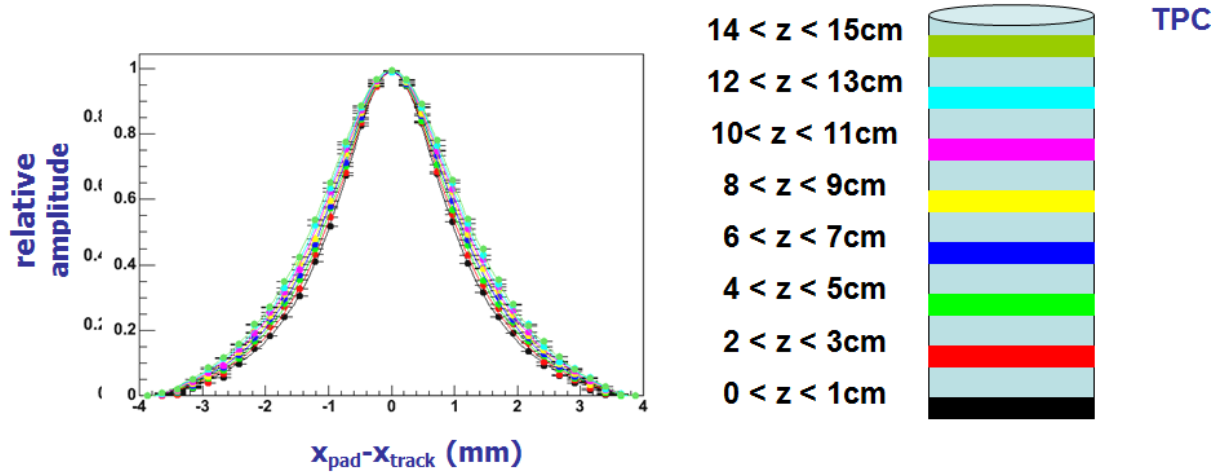


Figure 6-1. An example of PRF for different drift distances [46].

Before 2011, the PRF was given by the ratio of two symmetric 4<sup>th</sup> order polynomials:

$$PRF(x, \Gamma, \Delta, a, b) = \frac{1+a_2x^2+a_4x^4}{1+b_2x^2+b_4x^4} \quad (6-0-1)$$

It has four parameters  $a_2, a_4, b_2$  and  $b_4$ , and can be expressed in terms of full-width-at-half-maximum FWHM ( $\Gamma$ ), base width ( $\Delta$ ), and two scale parameters a and b.

$$a_2 = -(2/\Delta)^2(1 + a)$$

$$a_4 = (2/\Delta)^4 a$$

$$b_2 = (2/\Gamma)^2(1-b-2(1+a)(\Gamma/\Delta)^2 + 2a(\Gamma/\Delta)^4) \quad (6-0-2)$$

$$b_4 = (2/\Gamma)^4 b$$

All these parameters depend on the drift distance. But more parameters mean more time to find the right parameters for the different drift distance fitting and more correlation between the parameters.

Since 2012, a so-called Product-Form given in equation 6-0-3 is used as the PRF function,

$$PRF(x, r, w) = \frac{\exp[-4\ln 2(1-r)x^2/w^2]}{1+4rx^2/w^2} \quad (6-0-3)$$

It is a combination of a Gaussian with a Lorentzian function. When  $r=1$ , the PRF becomes a pure Lorentzian, and when  $r=0$ , the PRF becomes a pure Gaussian. Both the Lorentzian and the Gaussian share the same width parameter  $w$ . This function has only two parameters. Compared to equation 6-0-1, this leads to a better convergence of the parameter fits. The detailed discussion of this PRF function can be found in thesis [47].

### 3. FTPC programme

Before 2012, only one module mounted at the centre of the endplate of the TPC prototype was tested at a time. The FTPC program, which was developed by Carleton group, was used to do the analysis. The FTPC is a stand-alone programme written in C language, converted from an historical program written in FORTRAN.

The  $\chi^2$  minimization is used for track fitting. The track is described by the function

$$x_{track} = x_0 + \tan\phi * y_{row} \quad (6-0-4)$$

where  $x_{track}$  is the  $x$  position of the track crossing a given row,  $y_{row}$  is the  $y$  position of this row,  $\phi$  is the azimuthal angle of the track in this row and  $x_0$  is the intercept of the tangent line of the track in this row with the  $x$ -axis. The origin of the coordinate system is the centre of the module, the  $x$ -axis is along the row direction and the  $y$ -axis is perpendicular to the row direction. Figure 6-2 gives the example of one track in the coordinate system.

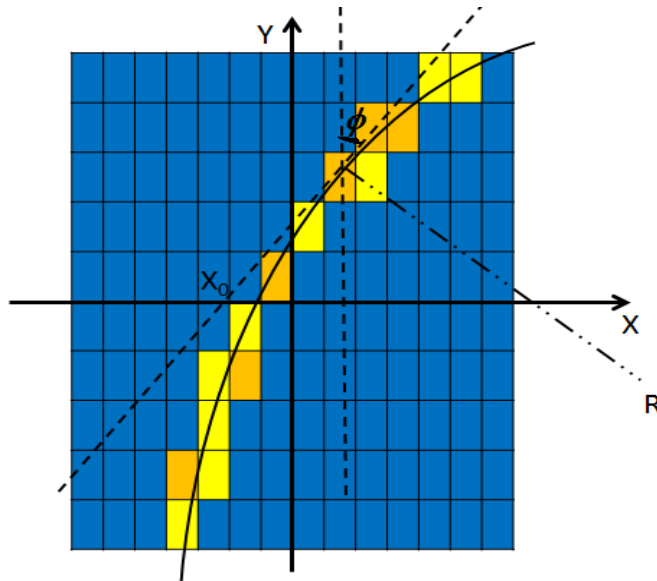


Figure 6-2. The example of one track in the coordinate system.

The  $\chi^2$  minimization to fit the track is given by the following equation:

$$\chi_{track}^2 = \sum_i^n \chi_{row}^2 = \sum_i^n \sum_j^m \left[ \frac{A_j^i - A_{peak}^i \text{PRF}(x_j^i - x_{track}^i)}{\sigma_{A_j^i}} \right]^2 \quad (6-0-5)$$

where  $i$  is the row number and  $j$  is the pad number in one row,  $x_j^i$  is the position of pad  $j$  in row  $i$  and  $x_{track}^i$  is the track cross point in row  $i$ ,  $A_j^i$  is the amplitude of the pad  $j$  in row  $i$  and

$A_{peak}^i$  is the scaling factor between the amplitude and the PRF corresponding to row  $i$ . The equation 6-0-1 is used as the PRF function.

By solving the condition of extremum:

$$\frac{\partial \chi_{row}^2}{\partial A_{peak}^i} = 0 \quad (6-0-6)$$

the solution for the value of  $A_{peak}^i$  is obtained as follows:

$$A_{peak}^i = \frac{\sum_j^m \frac{A_j^i PRF(x_j^i)}{\sigma_{A_j}^2}}{\sum_j^m \frac{PRF^2(x_j^i)}{\sigma_{A_j}^2}} \quad (6-0-7)$$

where the error  $\sigma_{A_j}^i$  was set to the square root of the pad's amplitude.

### 3.1.FTPC analysis chain

In FTPC, the analysis chain includes four steps. Firstly, the amplitude and time information of each pad needs to be extracted from the raw data encoded by electronics. The collected information of pads is stored in a so-called dense data (DD) file. To use a PRF function to fit the amplitude of the pads in one cluster, the PRF parameters need to be found. So, the second step is to tune the PRF parameters using the collected pad amplitudes and track position. After the PRF calibration, the PRF is used to calculate the bias correction and the resolution of the detector.

#### - Dense data production

The raw data include the full pulse information of the hit pads. For AFTER electronics, it has up to 511 sampling time bins for each channel. In compressed mode, a pulse lasts only a few time bins. During our analysis, we just need two values for each pad, amplitude and time. So, first the amplitude and time for each pad are extracted and saved in a file named DD (dense data). This greatly reduces the file size compared to the raw data size. There are many different ways to determine the amplitude and time, such as Single Point Maximum, Gaussian fit, or Parabola fit. In our analysis, the Single Point Maximum was used. It uses the largest ADC value in the pulse as the amplitude of the pad and the corresponding time bin as the time of the pad. An example is shown in figure 6-3.

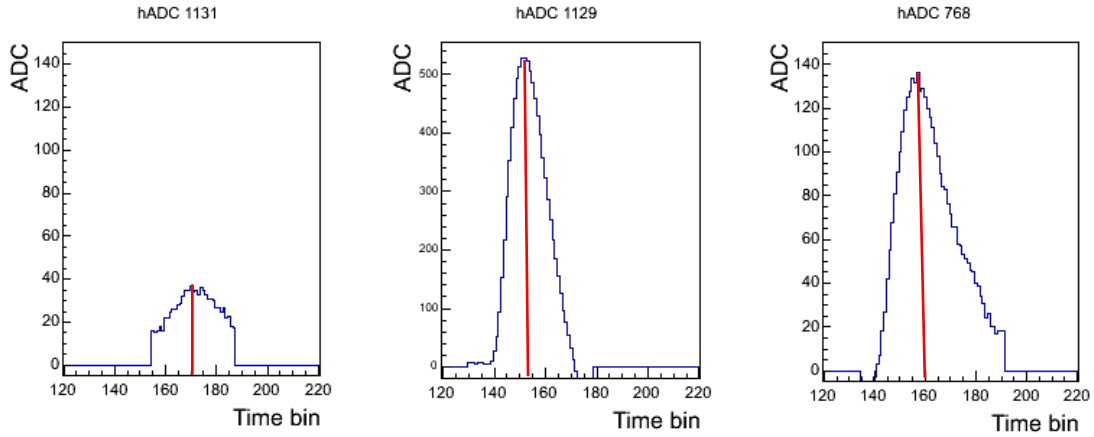


Figure 6-3. The pad pulses.

- PRF calibration

The PRF reflects the relation between the pad’s charge and the deviation of this pad to the track. To calibrate the PRF, the seed track needs to be known. Since there is no external equipment to precisely measure the track position in the LP-TPC environment, an initial guess track obtained from the measurement data was used. The position of the pad that has the largest amplitude in each raw is used to determine the seed track. A linear least squares fitting is used to fit these positions. The fitting line serves as the seed track to calibrate the PRF. The inverse radius of curvature of the seed track is always set to 0.

Figure 6-4 shows an example of a PRF fitting. Figure 6-4 (a) is the scatter plot of the pad amplitude and the relative position of the pad to the track. In the plot, the x-axis and y-axis are respectively as following:

$$\Delta x = x_{pad}^i - x_{track}$$

$$A_{Norm} = A_i / A_{peak}$$

where  $x_{pad}^i$  is the pad position in the row direction and  $x_{track}$  is the track position in this row,  $A_i$  is the pad amplitude and  $A_{peak}$  is calculated from equation 6-0-7. Figure 6-4 (b) shows the fitting to the scatter plot in the figure 6-4 (a) using the PRF function. To start the fitting process, initial PRF parameters are required. According to the meaning of the PRF function parameters, the starting parameter  $\Gamma$  is set to the width of the cluster in one row and equates to the number of the signal pads multiplied by the width of a pad,  $\Delta$  is set to the half of the  $\Gamma$ ,  $b$  is always kept to 0 during fitting and the initial value of  $a$  is set to 1. Each time, the new



parameters are given by the fitting and set as the starting value for the next fitting. To determine whether the new parameters are better used for PRF function, the  $\chi^2$  value from the fitting is checked. If the  $\chi^2$  becomes smaller, the new parameters are accepted. This fitting processes are repeated until the  $\chi^2$  does not become better compared the previous fitting. These final parameters obtained from the fitting are used as PRF parameters in the next processes: bias correction and resolution calculation.

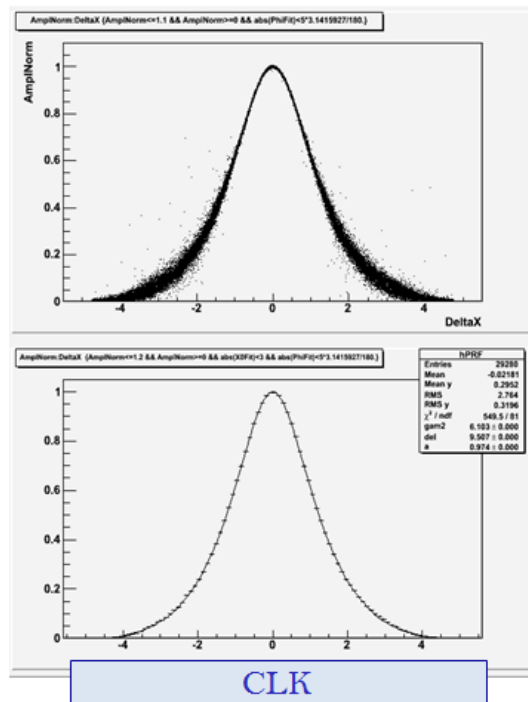


Figure 6-4. PRF fitting. (a) top one: the scatter plot of the pad's charge and the relative position of the pad to the track; (b) bottom one: the fitting of the scatter points using PRF function.

- Bias correction

The residual is the deviation of the measurement hit position in one row with respect to the position of the real track crossing this row. It can be separated into two parts: the symmetrical deviation part and the asymmetrical part. The symmetrical part includes the diffusion of the electrons passing a certain drift distance and the measurement error. In this part, the average deviation of all events is approximated to zero. The asymmetrical part is caused by the imperfect construction of the resistive anode. Each position on the resistive anode has a position dependent systematic error associated with its track position. This part always keeps the same error in a certain position among different events and cannot be removed by the

statistics of a large number of events. A bias correction is required to calculate and correct this systematic error before the final resolution is calculated.

To get the value used for the bias correction, the row residual and the fitting track are required.

The row residual is calculated by the equation 6-0-8:

$$\Delta = x_{track} - x_{hit} \quad (6-0-8)$$

where  $x_{hit}$  is the measurement hit position in this row and  $x_{track}$  is the corresponding track crossing position in this row in one event. The  $x_{track}$  is calculated by the equation 6-0-5 and the  $x_{hit}$  is calculated by minimizing the chi-square in the equation 6-0-9:

$$\chi_{row}^2 = \sum_j^m \left[ \frac{A_j - A_{peak} PRF(x_j - x_{hit})}{\sigma_{A_j}} \right] \quad (6-0-9)$$

Then, the row residual  $\Delta$  with the track  $x_{track}$  of each event is filled in a profile histogram for each row. Figure 6-5 gives an example of the profile histogram. The Y-axis displays the mean value of the row residual when a track crosses the corresponding position in this row. This mean value is used as the value of the bias correction. Then, the equation to calculate the measurement hit  $x_{hit}$  becomes as following from the equation 6-0-9:

$$\chi_{row}^2 = \sum_j^m \left[ \frac{A_j - A_{peak} PRF(x_j - x_{hit} + Bias(track)_i)}{\sigma_{A_j}} \right] \quad (6-0-10)$$

where  $Bias(track)_i$  is the bias correction function of this row, which is obtained from the profile histogram.

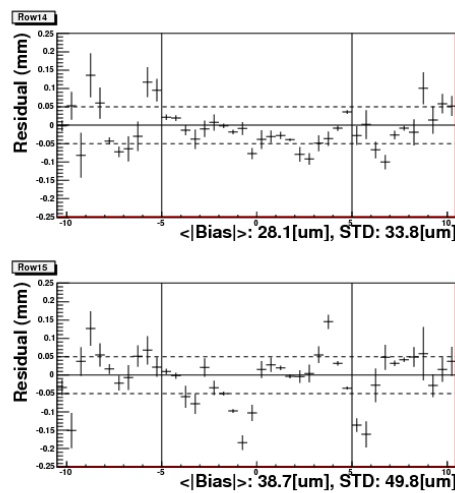


Figure 6-5. Profile histogram of the residual with the track in one row before bias correction.

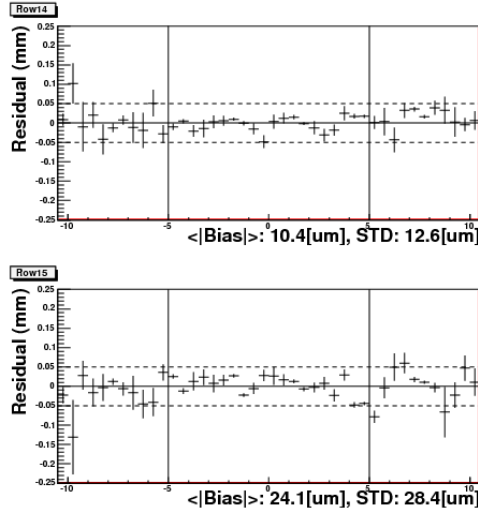


Figure 6-6. Profile histogram of the residual with the track in one row after bias correction.

After applying the bias correction, the systematic error caused by the imperfect construction of the resistive anode will be greatly reduced. Figure 6-6 gives the profile histogram after the bias correction corresponding to the same RUN data of Figure 6-5. We can see that the residual mean in each row is significantly improved.

- Spatial resolution calculation

The final step is to calculate the spatial resolution. Since there is no external equipment to precisely measure the track position, the deviation between the real track and the measurement hit position cannot be known and a fitting track is used to estimate the spatial resolution. After the bias correction, the residual for each row is calculated in two ways:  $\Delta_{in}$  is called the inclusive track fit residual and  $\Delta_{ex}$  is called the exclusive track fit residual. For a test row, the first way is to fit track including the test row and the second way is to fit track excluding the test row. The inclusive and exclusive residuals are calculated using the following equation respectively:

$$\Delta_{in} = x_{track}^{in} - x_{hit}$$

$$\Delta_{ex} = x_{track}^{ex} - x_{hit}$$

Then, the residual  $\Delta$  of the test row is calculated by the following equation:

$$\Delta = \frac{\Delta_{in}}{|\Delta_{in}|} \cdot \sqrt{\Delta_{in} \times \Delta_{ex}} \quad (6-0-11)$$

The standard deviation from Gaussian fit of the distribution of the residual  $\Delta$  is used to estimate the spatial resolution of the test row. Notice that, here the spatial resolution is not

estimated by the geometric mean method (see the Chapter 7 section 4.3), but this way also gives the correct estimate for the spatial resolution [48].

To get the general evaluation of the spatial resolution of the detector, a weighted average of rows is used:

$$\sigma = \frac{\sum \sigma_i \times \frac{1}{e\sigma_i^2}}{\sum \frac{1}{e\sigma_i^2}} \quad (6-0-12)$$

where the  $\sigma_i$  is the spatial resolution of row  $i$  and  $e\sigma_i$  is the associated error.

## 4. ILCSoft

Since 2012, multi-modules were tested at the endplate of LP-TPC simultaneously and the analysis has been done using the MarlinTPC software framework. MarlinTPC is a package for TPC developed in the ILCSoft software framework. It provides the simulation, digitisation, analysis, and reconstruction of TPC to handle multiple readout modules on its endplate for the LC-TPC collaboration. To obtain the spatial resolution, the Kalman Filter is used to fit the tracks. To implement the MarlinTPC software, the following packages, which are provided as a part of the ILCSoft, are required.

### Linear Collider Input Output (LCIO)

LCIO is a complete persistency framework that defines a data model for linear collider detector studies [49]. It supports C++ and Java languages. It provides the standard data format for all research groups, making codes and results more exchangeable and comparable. The container classes named collection of data objects store one or more objects of these data classes. The following data classes are used in our analysis.

1. TrackerRawData: generic class for raw tracker data without any correction applied. CellIDs are used to decode the readout channel and an arbitrary length vector for the ADC values is stored as a complete spectrum, as well as the time bin ID of the first valid sample of spectrum. During our data taking, multiple modules are mounted on the endplate and each module has 1726 channels. Two integer CellIDs are used: CellID1 is used as the physics channel of the pad in each module and CellID2 is used as the module number to denote the identification of the module.
2. TrackerData: same as TrackerRawData, except the type of ADC values stored in the vector. The ADC values are calibrated by applying all electronics related corrections

like pedestal subtraction and stored as float values in the vector instead of short integer values in TrackerRawData.

3. TrackerPulse: extracted from TrackerData to get the reconstructed pulse information. In this thesis, the maximum value in one spectrum is used as the amplitude of this channel and the corresponding time bin is used as the time of this channel.
4. TrackerHit: used to store the information of reconstructed measured hits in each row, such as the hit position and error matrix.
5. Track: this class stores the reconstructed track parameters and the coordinate of the reference point. For LCIO, a track is described by the parameters shown in figure 6-7:

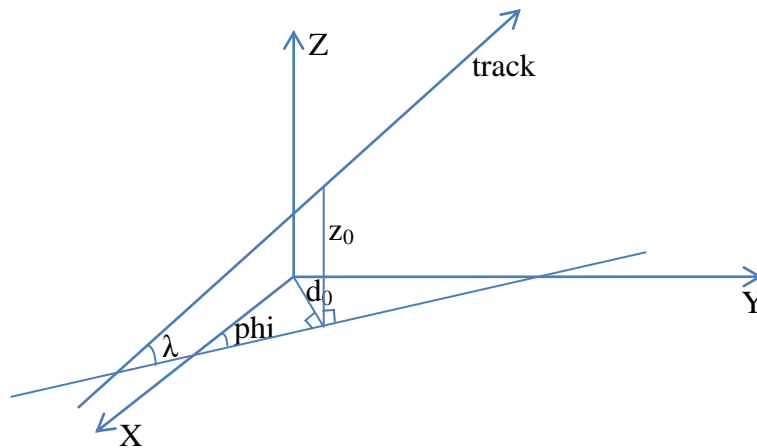


Figure 6-7. Track parameters in MarlinTPC for a straight track.

**$d_0$** : impact parameter of the track in the x-y plane in mm.

**phi**: angle between the track and x-axis at the reference point in the x-y projection in rad.

**omega**: signed curvature of the track in  $\text{mm}^{-1}$ .

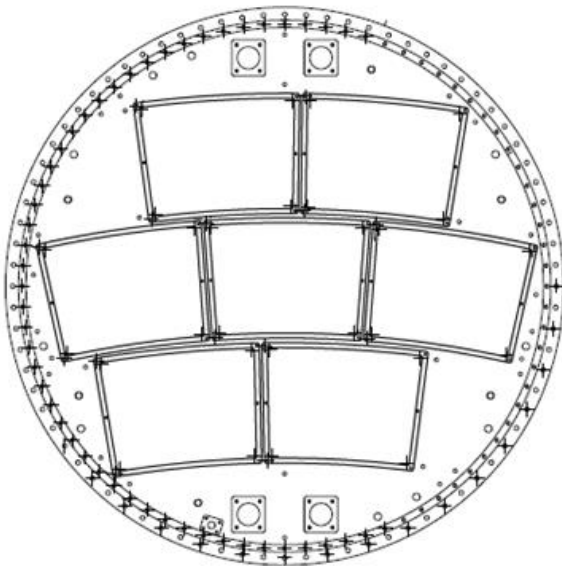
**$z_0$** : z-coordinate of the point on the track above the point of closest approach to the origin in the x-y plane in mm.

**$\tan\lambda$** : tangent of the angle between the track and its projection at the reference point in the x-y plane.

### GEometry Api for Reconstruction (GEAR) [50]

Gear is a geometry description toolkit for ILC reconstruction software [50]. It uses a XML file to define the geometry parameters of the detector. In our case, it is used to provide the geometry of LP-TPC, as well as the pad size of each Micromegas module. To define the pad

plane of each detector module, Gear provides four ways to define the pad layout: RectangularPadRowLayout, FixedPadAngleDiskLayout, FixedPadSizeDiskLayout and VersatileDiskRowLayout. They could be used to describe rectangular pads or keystone-shaped pads. For the Micromegas module, it has 1728 keystone shaped pads arranged to 24 rows by 72 pads. The height of each row is same except the first row. In a row, the pad pitch is same except two pads at each edge. To describe the difference height of rows, the VersatileDiskRowLayout is used to depict the geometry of a Micromegas module and the pad pitch difference in one row is neglected. This will influence the analysis results if the tracks pass through the edge or around the crack area. The LP-TPC endplate includes seven modules. The pad planes are same between these modules. This allows the displacement and rotation of the pad plane of module to arrange seven modules on the end plate of LP-TPC. The parameters of LP-TPC are taken from the technical drawing provided by Dan Petersen [51]. This drawing is viewed from the outside of endplate of LP-TPC. In the Gear file, all modules are placed according to the view from gas side, so all the angles of the central axis of modules are reversed. The displacements and rotations of the centre of each module used in Gear file are listed in table 6-1.



Row	Module position	Angle (degree)	Row position
inner / lower	right	-3.00	-172.5 mm
inner / lower	left	5.39	-172.5 mm
middle	right	-8.50	0 mm
middle	centre	-0.11	0 mm
middle	left	8.27	0 mm
outer / upper	right	-5.00	+171.615 mm
outer / upper	left	3.39	+171.615 mm

Table 6-1. Nominal module positions.

### Modular Analysis and Reconstruction for the LINear collider (Marlin)

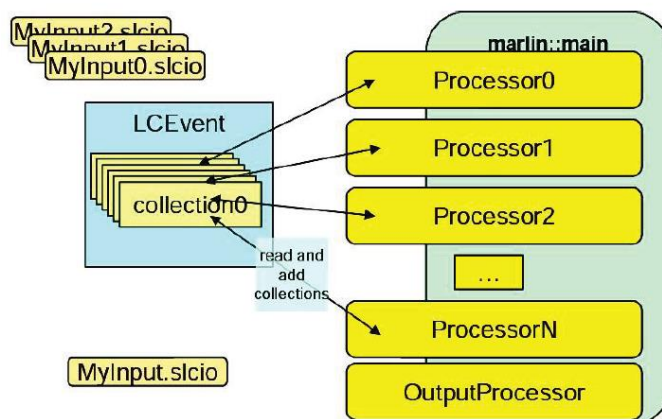


Figure 6-8. Schematic overview of the modular structure of Marlin.

Marlin [52] is a C++ software framework for ILC, based on LCIO. The main goal of Marlin is to facilitate the modular development of reconstruction and analysis code. It is implemented by different processors via a XML steering file. The steering file provides the parameters of the active processors and gives the order of the process calls. In each processor, the LCIO collections are read and written as input/output. The schematic overview of the modular structure of Marlin is shown in figure 6-8 [53].

### MarlinTPC

MarlinTPC is a special package based on Marlin common software framework for the TPC at ILC [54]. It provides a common software framework for the simulation, digitisation, analysis and reconstruction of TPC to handle multiple readout modules on the TPC endplate for the LC-TPC collaboration. One of the goals of MarlinTPC is to ensure that much code can be shared among the different groups and the results can be easily compared despite of many different readout structures, electronics, amplification systems used in different groups. A more detailed introduction of MarlinTPC can be found in [55]. In this thesis, the MarlinTPC analysis processors chain used for the Micromegas analysis is shown in table 6-2. The function of each process will be discussed in detail in the following section.

Data structure	Processor name	Input/output collection name
TrackerRawData		ADC_CHAN_DATA
	TrackerRawDataToDataConverterProcessor	
TrackerData		TPCConvertedRawData
	PedestalSubtractorProcessor	
TrackerData		TPCData
	PulseFinderProcessor	
	ChannelMappingProcessor	
TrackerPulse		TPCPulses
	PRFBasedHitFinderProcessor	
TrackerHit		TPCHits
	TrackMakingKalmanFilterProcessor	
Track		TPCTracks
	RootFileProcessor	

Table 6-2. MarlinTPC processors used for the Micromegas analysis.

### Kalman Filter

In a uniform magnetic field, a charged particle follows a helical trajectory. However, due to the multiple Coulomb scattering and energy loss, the helix trajectory is distorted for a low momentum track. A simple  $\chi^2$  fitting for track reconstruction is not sufficient. In order to solve this problem, the Kalman Filter for track reconstruction was introduced in HEP [56] [57] [58]. It is designed to effectively estimate its state at a certain point from multiple observations about a system. It allows that a different track parameter vector is used for a different measurement point. When a new measurement point is added, the track parameters are updated. The evolution of the track parameters can be estimated step by step. Hence the fit near the interaction point is effectively improved compared to a simple  $\chi^2$  fitting. The principle of Kalman Filter and application in ILCSoft are listed in appendix. A detailed introduction can be found in [59].



## 5. Micromegas modules analysis chain in MarlinTPC

The raw data recording by electronics of Micromegas modules are in a peculiar binary format file. They are sampled and digitized at 25 MHz by default. In order to do an analysis using ILCSoft, the first step is to convert the raw data format to LCIO data format. This is done by a program independent of MarlinTPC. The data are converted and saved in a standard LCIO data file according to the TrackerRawData collection, including two integer cell IDs, the time bin ID of the first valid sample of spectrum and an ADC values vector of complete spectrum. Then the converted LCIO data are used in MarlinTPC and the analysis is done according to the analysis processors chain shown in table 6-2.

### **TrackerRawDataToDataConverterProcessor**

The data in TrackerRawData collection is integer FADC. In this processor, the data objects are converted to TrackerData collection with floating point numbers for the channel time spectrum.

### **PedestalSubtractorProcessor**

During data taking, the pedestal mean of 250 was set for the read-out electronics. The pedestal value of 250 is subtracted for the analysis.

### **PulseFinderProcessor**

Using this processor, the charge and time of a pulse in each channel are calculated. The maximum ADC value in an ADC spectrum is counted as the charge of pulse and the corresponding time bin is counted as the time of pulse. The time value depends on the time bin and the clock frequency of electronics as follows:

$$T (ns) = time\ bin \times \left( \frac{1 \times 10^3}{Sampling(MHz)} \right) \quad (6-0-13)$$

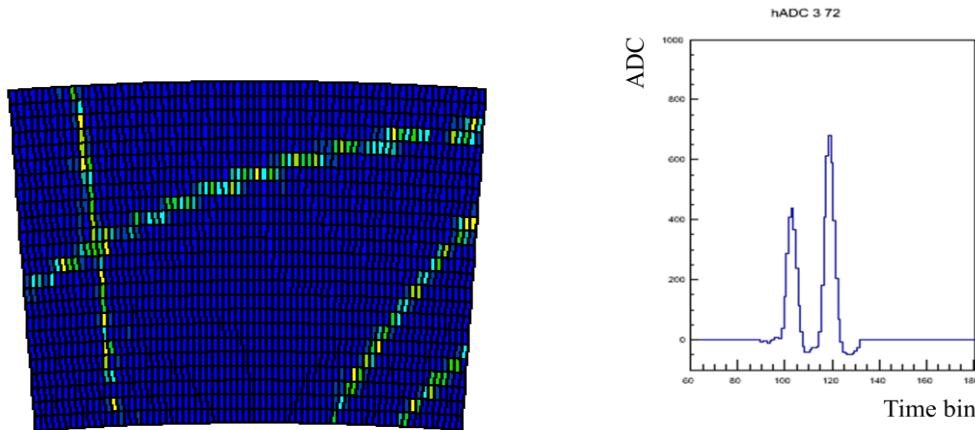


Figure 6-9. More than one track passes through module. The left one shows the tracks pass through module 3 (the middle one at the endplate); the right one shows the signal recorded on the pad where two tracks cross.

For analysis purpose, a threshold of 40 is applied and all charge values of pulses below this threshold will be neglected. In some events, more than one track passes through one pad. In this case, the arriving times of these tracks in this pad are different as shown in figure 6-9. The multiple pulses are split. The right hand side in figure 6-9 shows the multiple pulses in one pad, one with ADC 438 and time bin at 103 and one with ADC 682 and time bin 119.

### **ChannelMappingProcessor**

This processor is used to connect the hardware channel numbers of the electronics with the GEAR pad geometries number. In this processor, the TPCChannelMapping collection is called. This channel mapping is produced by a stand-alone programme called Mapping Generator, which allows generating the required LCIO file of mapping collection from a simple text file. In this mapping, the module IDs, the pad IDs and the corresponding hardware Channel IDs are provided. The pad ID is specified by the row number and the pad number in a row.

### **PRFBasedHitFinderProcessor**

In this processor, the hit positions in each row are calculated. To look for the hit in one row, the first step is to group pulses which are contiguous in time and lie on adjacent pads. Such a group is called a hit. To have well constrained fit of the hit position by the Pad Response Function, the minimum number of pads in one hit is 2.

The following Pad Response Function is used to calculate the hit position.

$$PRF(x: r, w) = A \frac{\exp(-4\ln(2)(1-r)x^2/w^2)}{1+4rx^2/w} \quad (6-0-14)$$

### **TrackMakingKalmanFilterProcessor**

In this processor, the Kalman Filter is used for track finding and fitting. Each row is defined as one layer. All hits are filled in the corresponding layer. The best hit with the minimum  $\Delta\chi^2$  in each layer is checked and fitted using Kalman Filter algorithm. When a new hit is added in the track, the track parameters are updated with the new collected information. When all layers are checked, a track is found and collected in the LCIO format.

When this step is finished, the number of the tracks in one event and the hits information in each track are obtained.

### **RootFileProcessor**

After the tracks are collected, the RootFileProcessor is used to analyse the track information. The track numbers in one event are checked and only the events with one track are used for the study of the spatial resolution. The hits in one track are checked and refitted to get the parameters of the track. The bias correction is applied. The residual of each row is calculated and saved into a root file, as well as the tracks and the hits information.

Chapter 7  
**Analysis results**



In the last few years, the Micromegas modules have been tested without magnetic field and in a 1 T magnetic field with a 5 GeV electron beam in several periods, as well as using a  $^{55}\text{Fe}$  source or cosmic-rays. The working gaseous mixture in the TPC was Ar/CF<sub>4</sub>/Isobutane (95:3:2), so-called T2K gas. The T2K gas was chosen for its high speed, large  $\omega\tau$  and low diffusion. The tests were carried-out at room temperature and atmospheric pressure. The performances of the Micromegas TPC, such as gain, energy resolution, uniformity, resolution, distortion *etc...*, have been studied in detail.

## 1. Gain study

The gain of the Micromegas modules has been studied in several periods under different conditions.

In the last two periods, data were taken at several settings of the mesh high voltage with two values of the drift electric field. The maximum ADC in the pulse of one pad is used to calculate the collected charge in this pad. To get the charge per row, first the ADC count in each pad is summed in each row. To suppress the noise, each pad's amplitude is required to be not less than 30 ADC counts and the sum of the charge in each row to be larger than 50 ADC counts. Then, these values are filled in one histogram. Figure 7-1 shows the histogram of each row's ADC. It follows a Landau distribution. Using a Landau fitting, the most probable value (MPV) is used as the average ADC in one row. For our Micromegas module, the pad length is 6.85 mm. Figure 7-2 shows the histogram of effective number of electrons for 5 GeV electrons for a gas thickness of 6.85 cm simulated by Heed [60]. The corresponding electrons using MPV are 45 in one row. The full ADC for each pad is 4096 ADC which corresponds to the electronics gain 120 fC. So the gain is obtained with the following formula:

$$\text{The fitted MPV} \times \frac{120 \times 10^{-15}}{4096} \times \frac{1}{1.6 \times 10^{-19}} / 45 \quad (7-0-1)$$

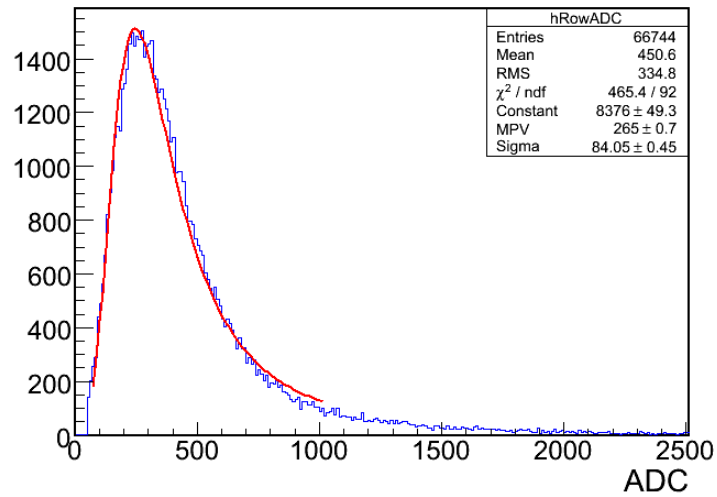


Figure 7-1. The histogram of pads' ADC in each row.

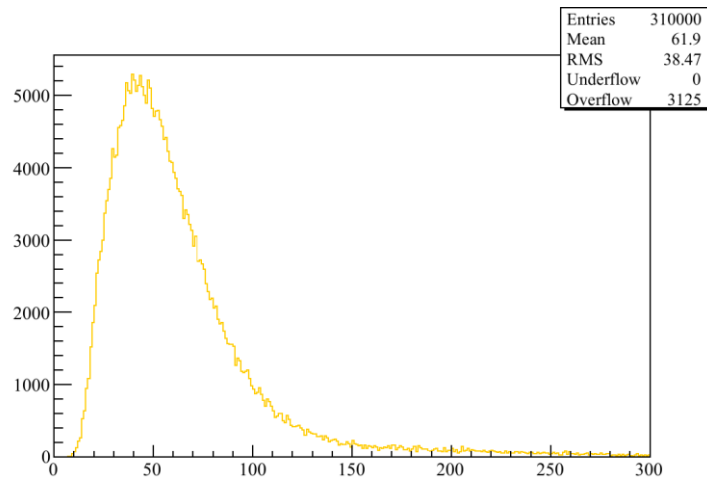


Figure 7-2. The distribution of effective number of electrons for 5 GeV electrons for a gas thickness of 6.85 cm simulated by Heed [61].

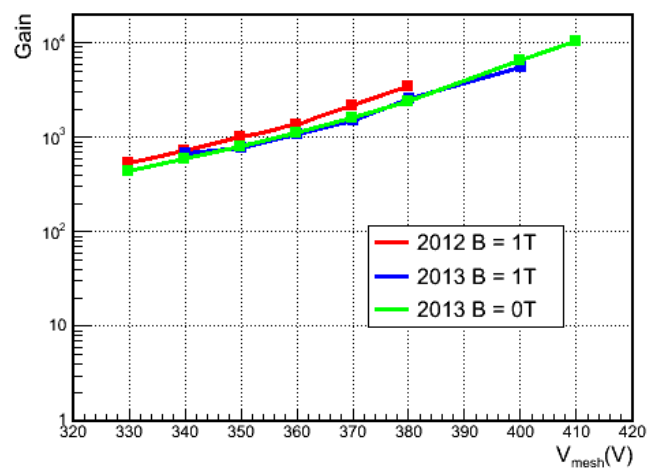


Figure 7-3. Gain as a function of the mesh voltage.

Figure 7-3 shows the gain as a function of the mesh voltage. At the same time, the gains measured in different test periods are compared. The drift electric field was set to 230 V/cm during these data taking. The red line shows the results obtained in June, 2012 and other lines show the results from January 2013. Since the atmospheric pressure, the gas purity due to O<sub>2</sub> and H<sub>2</sub>O contamination in the gaseous mixture were different during these two test periods, the results measured in 2013 is lower than 2012, but the results between these two beam-test periods are consistent. Compared with the gain 2500 obtained from 2013 beam data at  $V_{\text{mesh}} = 380$  V, the gain is about 2700 for the same module obtained from the test-bench.

From figure 7-4, where the gain curves are compared for drift electric fields of 140 V/cm and 230 V/cm, we can see that these two agree which shows that there is no significant change in collection efficiency.

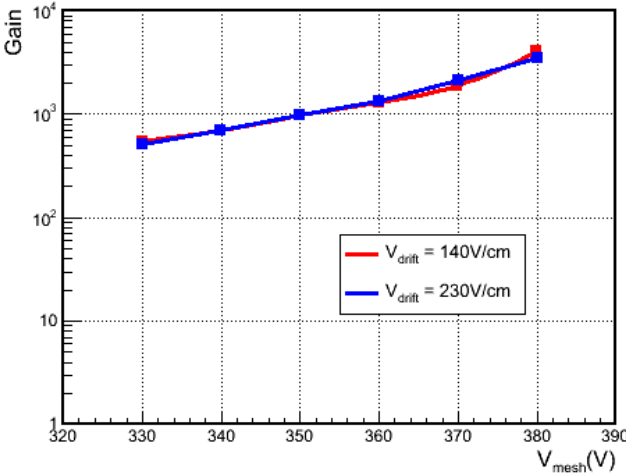


Figure 7-4. Gain as a function of the mesh voltage with different drift electric fields.



## 2. Drift velocity study

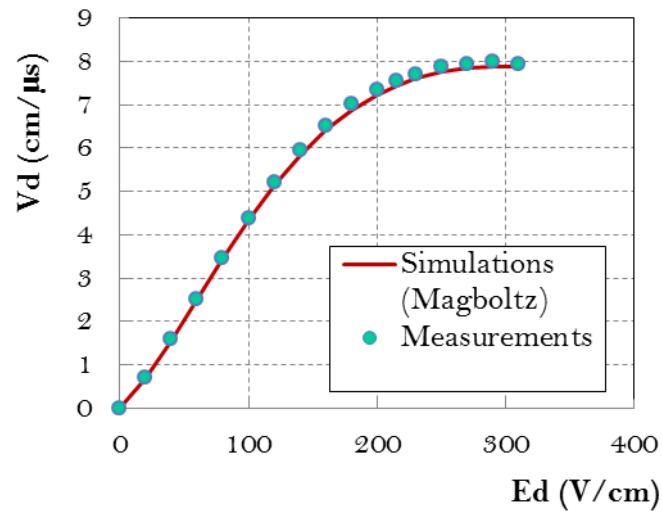


Figure 7-5. Drift velocity measurements ( $B=0$  T).

With  $B=0$  T, the electron drift velocity in T2K gas has been measured as a function of the drift electric field in 2009, as shown in figure 7-5. The gas temperature was stable at  $19$  °C during the measurements, and the pressure remained around 1035 hPa. The water content of the gas mixture was measured to be 35 ppm. The measurements are compared with simulations. From figure 7-5, we can see the simulation results are a little lower than the experiment results. This was also found in the GEM TPC preliminary study [62]. At the drift electric field of 230 V/cm, the measured drift velocity is  $7.698 \pm 0.040$  cm/ $\mu$ s, compared with the Magboltz simulation result of  $7.583 \pm 0.025$  cm/ $\mu$ s (the error on the simulation is dominated by the uncertainty on the gas composition). The difference is small but significant:  $1.5 \pm 0.6\%$ .

With  $B=1$  T, the electron drift velocity in T2K gas has also been measured in 2013. The results are shown in figure 7-6. The gas temperature was stable at  $16.5$  °C during the measurements, and the pressure remained around 1010 hPa. The water content of the gas mixture was measured to be 99 ppm. The simulation results are also shown in figure 7-6. The slight variation in the measurements may be due to a variation of the water content.

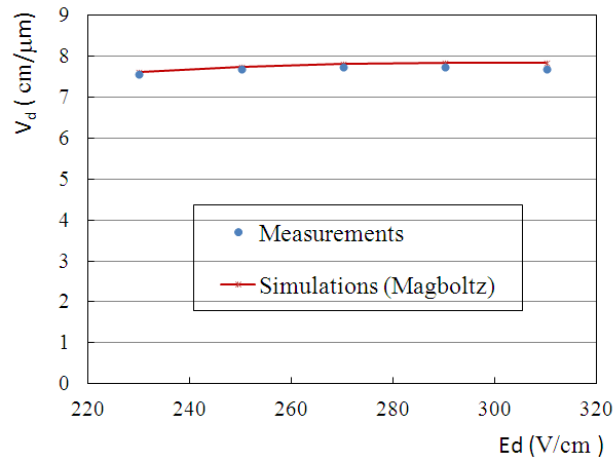


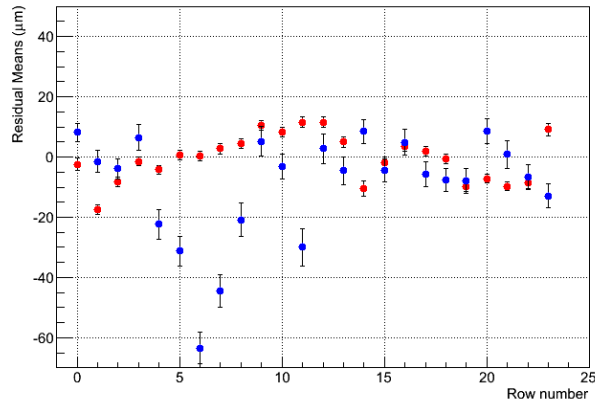
Figure 7-6. Drift velocity measurements (B=1 T).

### 3. Analysis with one module

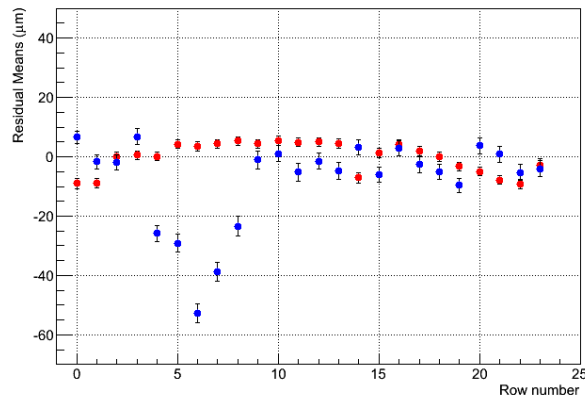
From December 2008 to March 2010, data have been taken with only one module mounted at the center of the endplate of the TPC, without magnetic field and in a 1 T magnetic field, with a 5 GeV electron beam. Data were taken at different drift distances by moving the detector perpendicular to the beam, along the magnet axis. All the data used for analysis here are with zero suppression.

#### 3.1. Uniformity of different modules

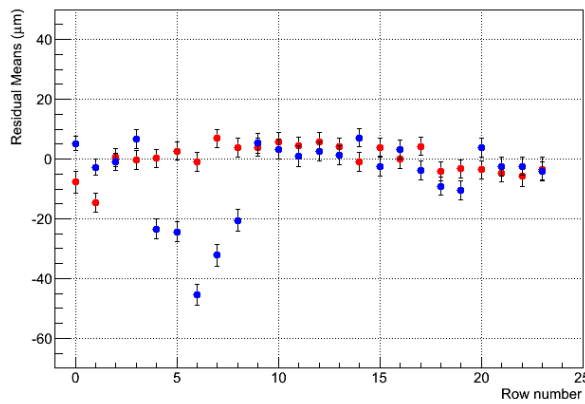
The residual mean (with bias correction) for each row at three different drift distances are shown in figure 7-7. The distortions are independent of the drift distance. The residual mean was found to be consistent with zero for the module with carbon-loaded polyimide anode and reached 40  $\mu\text{m}$  for the module with resistive ink anode. The uniformity over 24 rows in the resistive Kapton module is very good, with no edge effect or dead area up to the edge of the module. The distortions of the module with resistive ink anode are probably caused by the non-uniformity of the resistive layer. The material of resistive ink was discarded for the production of subsequent modules.



(a)  $Z = 5$  cm



(b)  $Z = 35$  cm



(c)  $Z = 50$  cm

Figure 7-7. Residual mean in  $\mu\text{m}$  for each row (from 0 to 23) at three different drift distances with  $B = 1$  T. Blue points are for the module with resistive ink anode and red points are for the module with carbon-loaded polyimide anode.

### 3.2. Spatial resolution

With the same data, the equation 6-0-1 was used as the PRF function and FTFC was used as the analysis program to study the spatial resolution. Since there is no external reference point in our setup, the position of the true track cannot be known. The spatial resolution of each row

is given by the standard deviation of residual calculated using the equation 6-0-11, and then the spatial resolution of one module is given by the equation 6-0-12. Figure 7-8 show the spatial resolution as a function of the drift distance with B=0 T for module 4 and module 5 respectively. Their anodes are made by some materials. Figure 7-9 show the spatial resolution as a function of the drift distance with B=1 T for module 2 with resistive ink anode and module 3 with resistive kapton anode. At large drift distance, the spatial resolution is reduced due to the magnet field compared to figure 7-8. The module with resistive kapton anode has better resolution than the module with resistive ink anode.

Using a fit function as follows to fit the measured spatial resolutions, we can get the spatial resolution at drift distance Z=0.

$$\sigma = \sqrt{\sigma_0^2 + \frac{C_D^2 Z}{N_{eff}}} \quad (7-0-2)$$

where  $\sigma_0$  is the spatial resolution at Z=0,  $C_D$  is the transverse diffusion constant, taken from Magboltz, and  $N_{eff}$  is the number of effective electrons over the length of a pad.

From the fit results, we can see the spatial resolution at Z=0 was found to be about 60  $\mu\text{m}$  without magnetic field ( $C_D = 315.1 \mu\text{m}/\sqrt{\text{cm}}$ ) or with 1T magnetic field ( $C_D = 94.2 \mu\text{m}/\sqrt{\text{cm}}$ ), which is about 50 times smaller than the pad size.

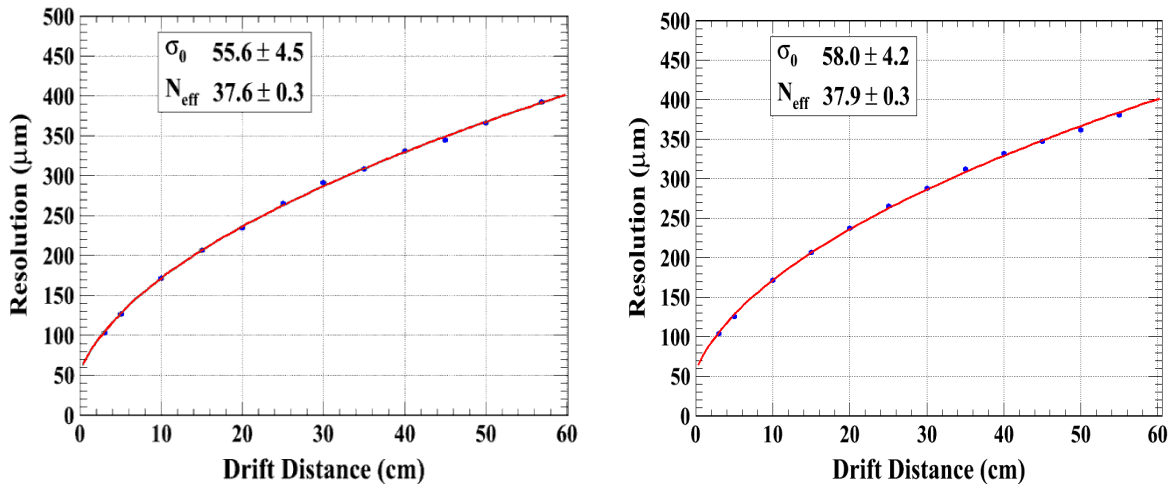


Figure 7-8. Measured resolution as a function of the drift distance Z at B=0 T (data taken with 200 ns peaking time): (a) module 4 (resistive kapton anode with a resistivity of about 3  $\text{M}\Omega/\square$ ), (b) module 5 (resistive kapton anode with a resistivity of about 3  $\text{M}\Omega/\square$ ).

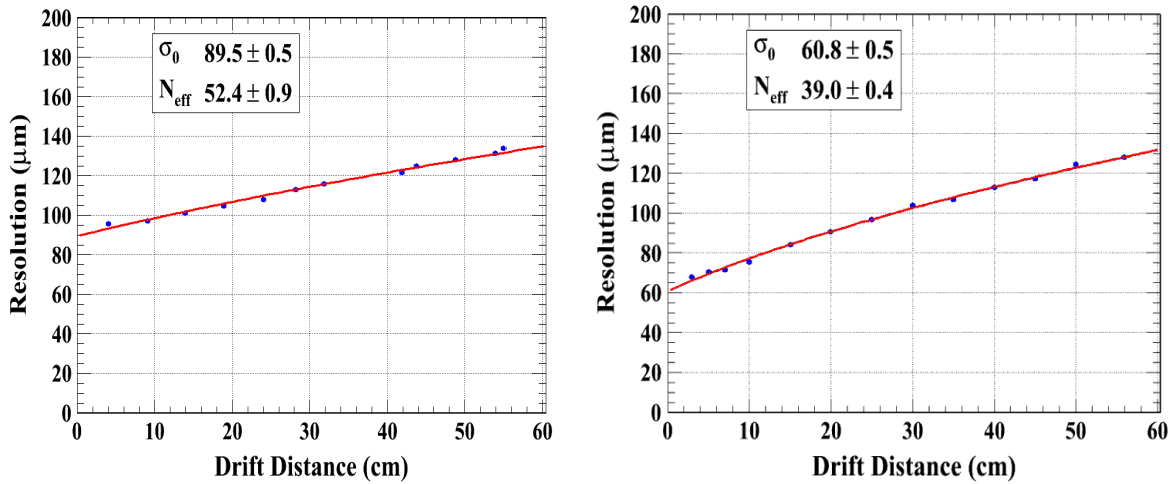


Figure 7-9. Measured resolution as a function of the drift distance  $Z$  at  $B=1$  T (data taken with 500 ns peaking time): (a) module 2 (resistive ink anode with a resistivity of about  $3 \text{ M}\Omega/\square$ ), (b) module 3 (resistive kapton anode with a resistivity of about  $5 \text{ M}\Omega/\square$ ).

### 3.3. Optimization of the ADC accuracy

The ADC used in T2K electronics digitizes the signals over 12 bits, which allows 4096 values. The precision of the ADC is an important cost driver for the system. The power consumption increases dramatically with the number of bits. To see how the spatial resolution deteriorates with decreasing the number of bits, I grouped the ADC bits by two, four, and eight... and repeated the whole analysis with the rounded-up ADC counts using the data taken in 2011. The results are shown in figure 7-10. From this study, we conclude that down to 9 bits the deterioration is acceptable.

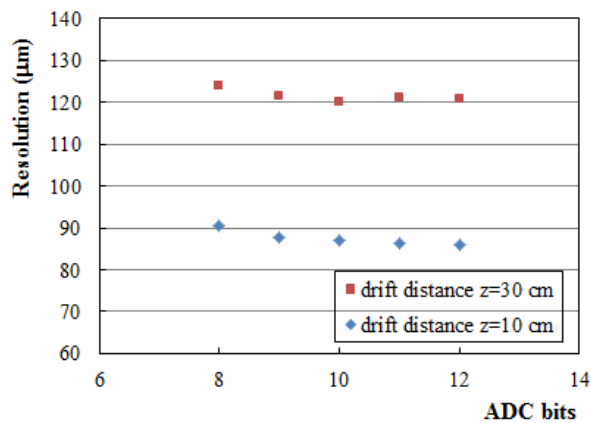


Figure 7-10. Resolution as a function of ADC bits at different drift distances.

## 4. Analysis with multiple modules

Since 2012, beam tests with multiple modules were carried out with 5 GeV electron beam. The endplate of the TPC was rotated by 90 degrees so that the beam can pass through three modules arranged in three rows as shown in figure 7-11 (a). The beam direction is parallel to the endplate of TPC. A typical beam event is displayed in figure 7-11 (b) with the beam direction from bottom to top. The figure 7-11 (a) is seen from outside of the TPC and figure 7-11 (b) is seen from gas side of the TPC. The endplate of TPC is defined as x-y plane in the coordinate system with x-axis approximately perpendicular to the pad rows of the module and y-axis parallel to the rows of the module. The z-axis is perpendicular to the endplate and parallel to the magnetic field and electric field direction.

Towards the goal of the development of standard ILC analysis software to make the results easily compared between different groups, the analysis software for the beam data with multiple modules was switched from FTPC analysis software to a standard ILC analysis software, MarlinTPC, and the Kalman Filter is used to reconstruct the tracks.

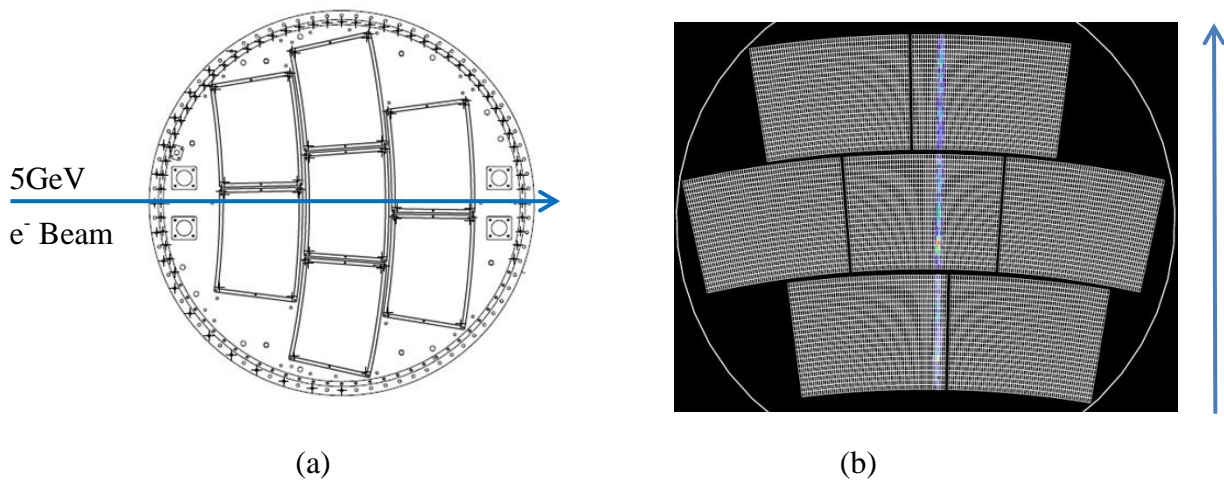


Figure 7-11. (a) Beam direction (b) Beam event.

### 4.1. Missing pads

Since 2012, the new integrated electronics which has been introduced in chapter 3 are used as the readout electronics. This new electronics allows us to mount multiple modules simultaneously (see the figure 3-6). Considering the mechanical problem which has been discussed in chapter 4, the map of disconnected pads is checked firstly. By integrating the cosmic events, the number of missing pads can be checked. For example, the figure 7-12 shows the state during the first two days test. The pads coloured in white mean there is no

charge collected on them. And the figure 7-13 shows the state of missing pads in the last-but-one data taking day. Here in these two figures, the geometry of the detectors is approximate. It is only used to check how many pads are missing. From figure 7-13, we can see that only the central middle module keeps the good condition. Due to this mechanical problem, only the central module is used for the study of the spatial resolution.

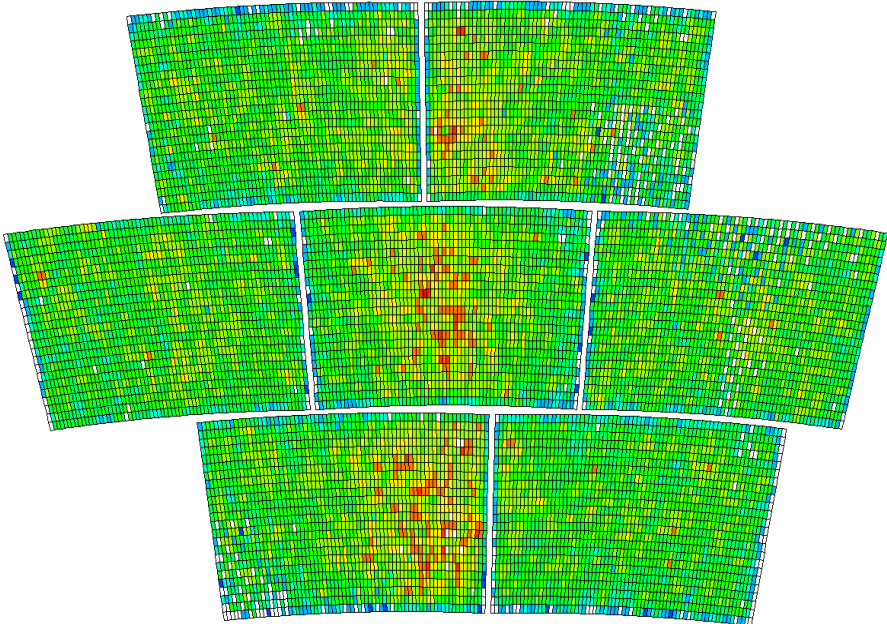


Figure 7-12. The state of missing pads during first two days test. The missing pads are filled with white colour.

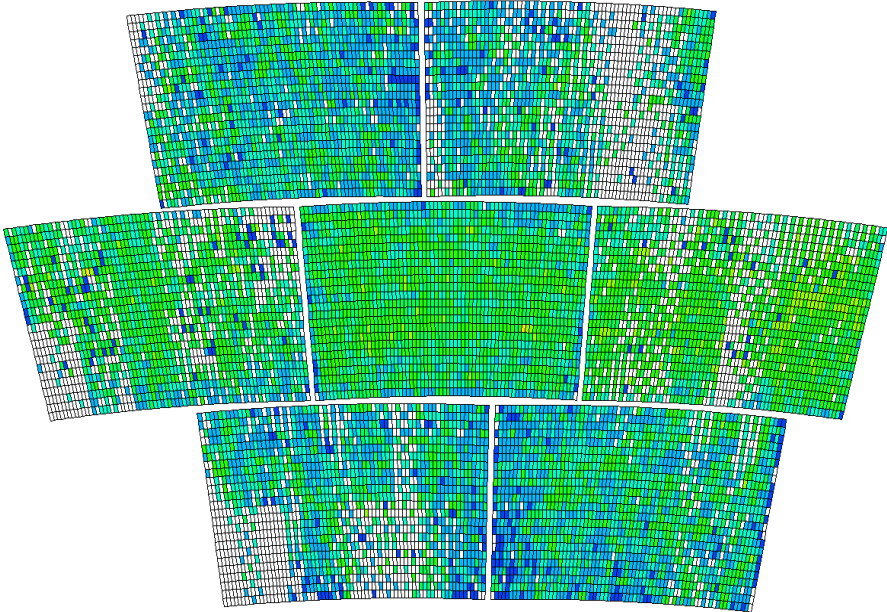


Figure 7-13. The state of missing pads in the last-but-one data taking day. The missing pads are filled with white colour.

## 4.2. Distortions

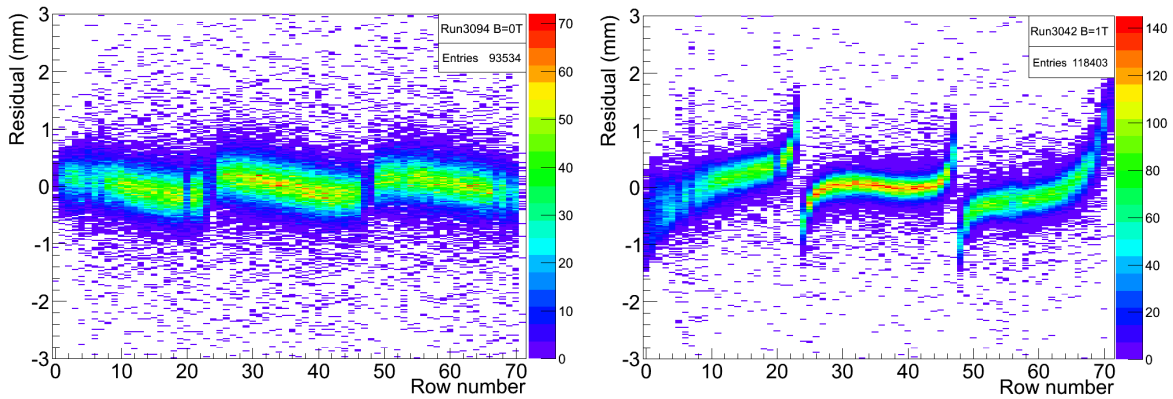


Figure 7-14. Left: the residual versus the row numbers in B=0 T. Right: the residual versus the row numbers in B=1 T. Both are before bias correction.

Figure 7-14 shows the residuals without or with magnetic field before bias correction. The left plot shows the residual versus the row numbers tested without magnet. The beam passes through three modules and each module has 24 rows. The transfer between two modules is clearly seen. The right-hand plot shows the residual versus the row numbers tested in B=1 T magnet. Here the distortion is influenced by  $E \times B$  effect. Compared to the left plot, the transverse diffusion is reduced by the magnetic field and the distortion has ‘S’ shape. The distortions are caused by the misalignment of the position of modules, the misalignment between the axis of the magnetic and electric fields, and the local electric field imperfection at the junction of the modules and the frame of the endplate.

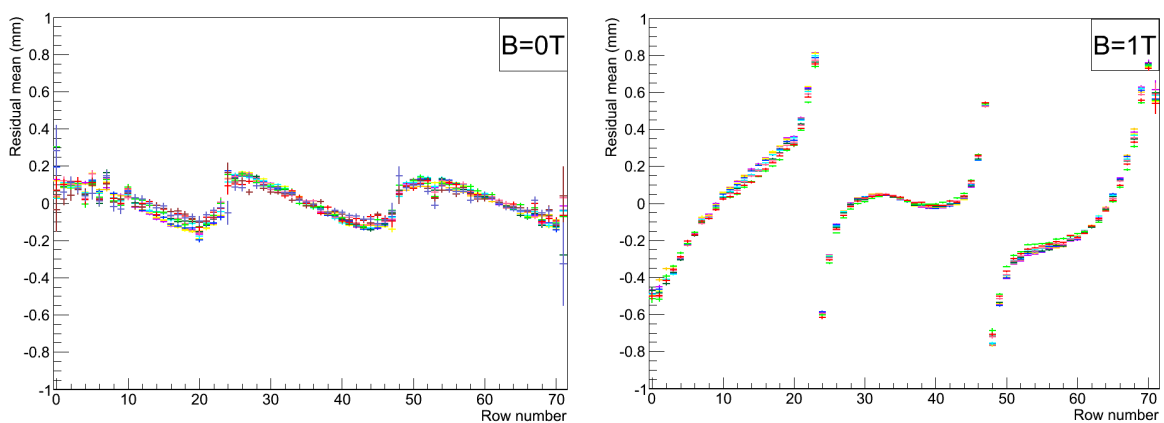


Figure 7-15. Left: the residual mean versus the row numbers in B=0 T. Right: the residual mean versus the row numbers in B=1 T. Different colours respond to different drift distances from 15 cm to 50 cm.



Figure 7-15 shows the average distortions tested at different drift distances in B=0 T and B=1 T magnet. The different colours are for different drift distances. We can see that the distortions are independent on the drift distance.

### 4.3.Spatial resolution study

#### Event selection

To accurately estimate the resolution, a sample of single-track events is selected to use for the analysis. Thanks to the Kalman Filter, the multi-track events can be reconstructed and the number of tracks in one event is obtained. Then only the events with one track are kept. As shown in figure 7-16, the left hand side event is rejected and the right hand side event is kept.

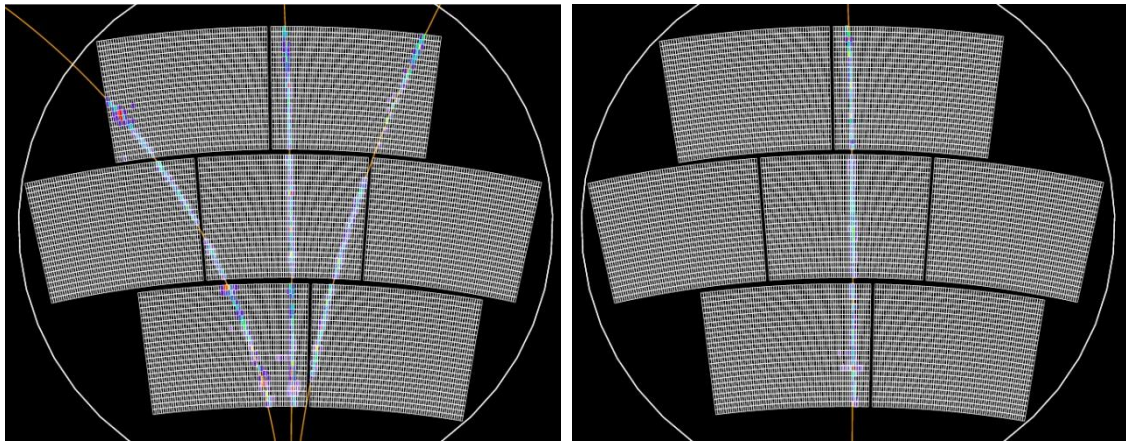


Figure 7-16. Examples of track fitting in one event. Left: multi-tracks in one event; Right: signal track in one event.

#### Track fitting

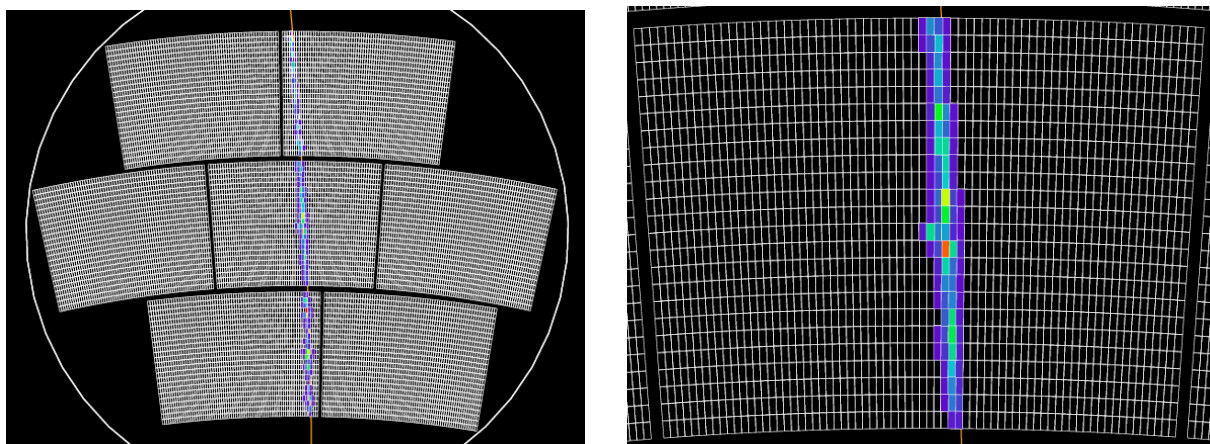


Figure 7-17. Single track event. Left: display with 7 modules; Right: display with the centre module (Zoom).

Figure 7-17 shows only one track (left) in this event, but the hit 35 has very large deviation from the track (right). The fitting track result is shown in figure 7-18 if this hit is used to fit track. It is clear that the track is seriously biased by this hit. To get the right track position, this hit should be removed from track fitting. At the same time, we want to preserve the residual information of this hit. To realize this in the Kalman Filter, these kinds of hits are given a very large error during track fitting. The fitted track in this way is shown in figure 7-19.

The chi-square is calculated by the equation:

$$\chi^2 = \sum_{i=1}^k \left( \frac{x_i - \bar{x}}{\sigma_i} \right)^2 \quad (7-0-3)$$

Since we don't know the  $\sigma_i$  before we get the resolution, a supposed  $\sigma$  is used for all hit points in the fitting calculation in Kalman Filter. The track parameters are updated based on  $\chi_i^2$  when a new hit is added. If the supposed sigma of one hit is given a very large value compared with other hits,  $\chi_i^2 \sim 0$ , then this hit will not influence the track parameters. To check the effectiveness of this way, the fitting track excluding hit 35 is also plotted as shown in figure 7-20.

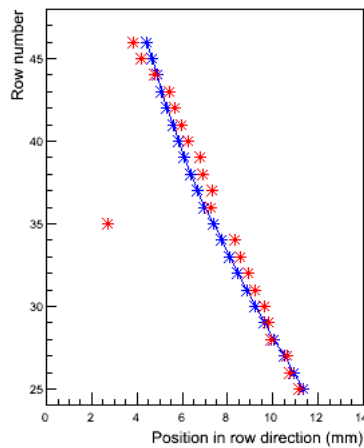


Figure 7-18. Fitting track using all hits in one track. (Red line: hit position; Blue line: fit track)

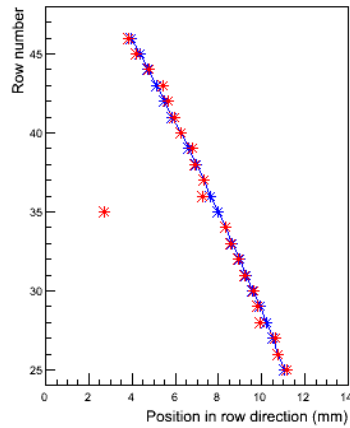


Figure 7-19. Fitting track with the error affected to the hit 35 set to a very large value so that it does not weight in the chi-squared. (Red line: hit position; Blue line: fit track)

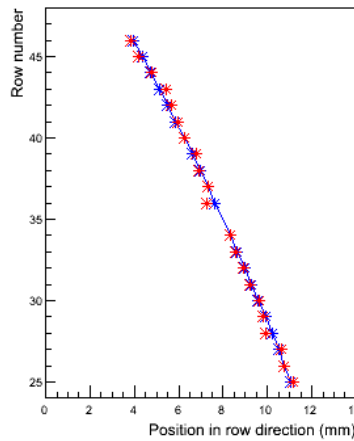


Figure 7-20. Fitting track after removing the hit in row 35 which has large residual. (Red line: hit position; Blue line: fit track)

### Spatial resolution

The spatial resolution of each row is calculated using the geometric mean resolution, where the geometric mean of the standard deviations from Gaussian fit of the residual to a track fitted with and without the specific row is calculated. Figure 7-21 shows the distribution of the residuals obtained from the track fitting including and excluding the specific row at 15 cm drift distance. The standard deviations from Gaussian fit of the distributions are used to estimate the resolution. The geometric mean method [63] as the following formula is used to obtain the spatial resolution of the specific row.

$$\sigma = \sqrt{\sigma_{in} \times \sigma_{ex}}$$

where  $\sigma$  is the spatial resolution of the specific row,  $\sigma_{in}$  is the variance of the residual to the fitting track including the specific row and  $\sigma_{ex}$  is the variance of the residual to the fitting track excluding the specific row.

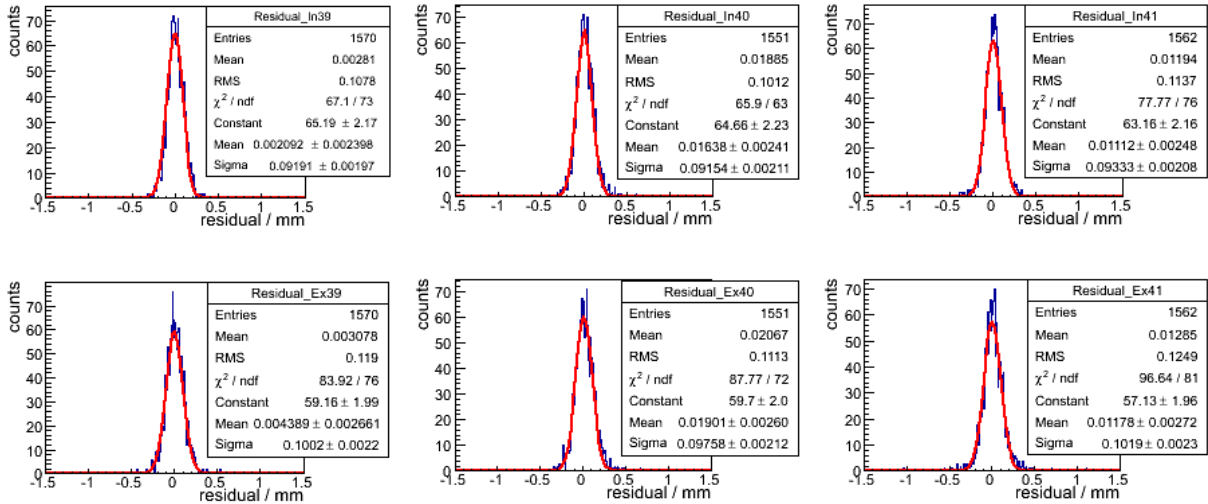


Figure 7-21. Distribution of the residuals at 15 cm drift distance. Top: including the test hit in the track fit; Bottom: excluding the test hit in the track fit. Here only shows 3 rows of 72 rows.

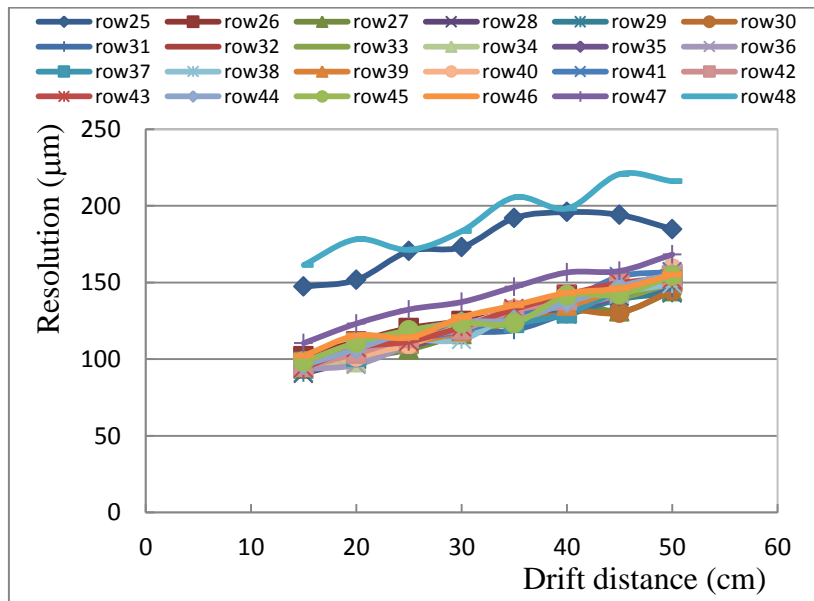


Figure 7-22. Resolution of each row of the central module.

Figure 7-22 gives the spatial resolutions of each row of the central module at different drift distances. It is clear that the spatial resolutions of rows are consistent, except the first and last rows which have larger deviation. To get the general evaluation of the resolution of a detector,

the first row and the last row are removed when the track is fitted and the weight average of 22 rows as the equation 6-0-12 in Chapter 6 is used as the resolution of the detector.

- **Z Scan**

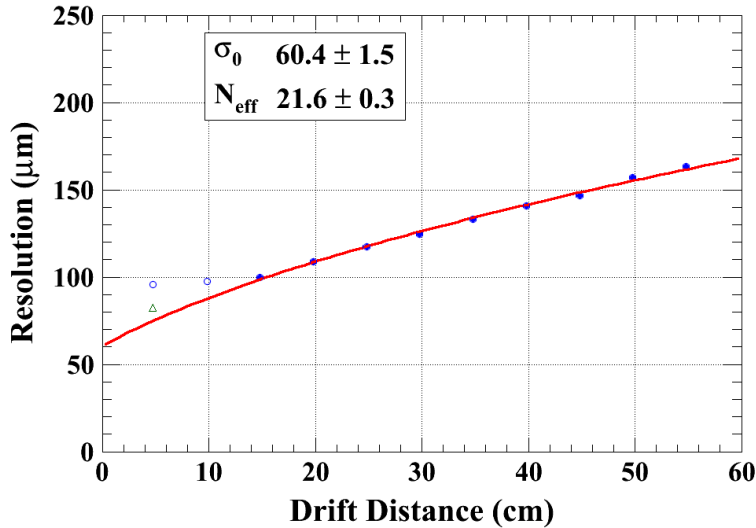


Figure 7-23. Spatial resolution of the central module at B=1 T. Data with seven modules taken in 2013.

Figure 7-23 gives the spatial resolution of the central module as a function of the drift distance in a B=1 T magnet. At the beginning of the data taking, we do not know the exact drift distance. During the data taking for the set of data with 100 ns peaking time and B=1 T, the beam was only set at drift distance from 14.8 cm to 54.8 cm by step 5 cm each time. Later the data for the drift distances 4.8 cm and 9.8 cm were taken with B=1 T, the resolution of these two data are shown in figure 7-23 with hollow blue circle. Using function 7-0-2 to fit the resolutions obtained from the drift distance 14.8 cm to 54.8 cm, a 60 μm resolution at zero drift distance is obtained. Also, a data point with 400 ns peaking time was taken at a drift distance of 4.8 cm, the resolution is 82 μm shown in figure 7-23 with green hollow point. Hollow points are not included in the fit. A possible explanation for these points lying out of the resolution curve is low signal on the side pads for this particular module.

Extrapolating the results using the equation 7-0-2, the spatial resolution will be about 108 μm at 2 m drift distance in a 3.5 T magnetic field as shown in figure 7-24 ( $C_D$  is about 30 μm/√cm and  $N_{\text{eff}}$  is assumed about 22). The extrapolating results of Asian GEMs using the resolution results from different rows [64] are also shown in the same figure. Both

Micromegas and GEM seem to be close the goal for the ILD-TPC detector. But the GEM module has 1 mm wide pads, this requires three times more channels of the electronics.

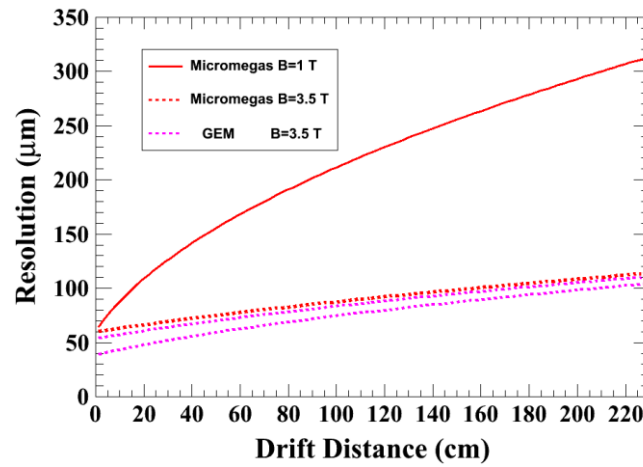


Figure 7-24. Extrapolation of the spatial resolutions of Micromegas and GEM to the ILD-TPC.

#### - Phi Scan

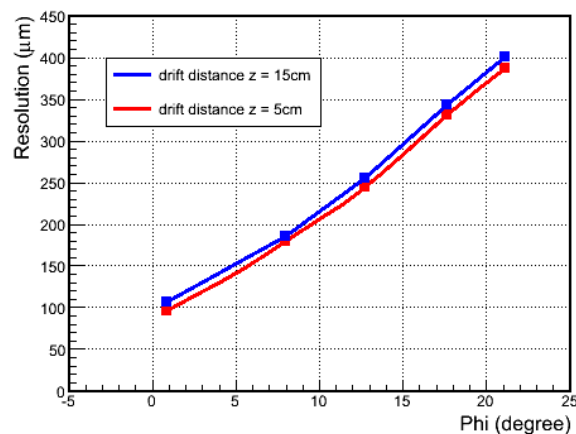


Figure 7-25. Resolution as a function of the crossing angle at different drift distances in B=1 T.

The data also were taken at different crossing angles. The crossing angle is the angle between the particle momentum and the perpendicular direction of pad rows of the Micromegas module. When a track crosses the pad row of Micromegas modules at large angle, it deposits ionization on more pads compared with the track which passes the modules perpendicularly to the pad row. Figure 7-25 shows the resolution as a function of the angles with B=1 T magnetic field.



# Conclusion





In this thesis, a TPC prototype with a Micromegas amplification stage has been built and successfully tested.

From 2008 to 2010, five different bulk Micromegas-TPC detector modules were studied without or with  $B=1$  T magnetic field at DESY. Thanks to the charge spreading technique, the resolution is measured to be about  $60\ \mu\text{m}$  at zero drift distance with 3 mm wide pads. This extrapolates to be about  $100\ \mu\text{m}$  at the nominal ILD field of 3.5 T and at the maximum drift distance of about 2 m. It validates the resistive layer technique to obtain charge dispersion. The module with resistive polyimide anode shows better uniformity compared to resistive ink module.

Since 2012, nine modules (seven modules plus two spare ones), using a quasi-industrial production chain, were produced. Seven modules mounted at the endplate of TPC prototype simultaneously, which fully covered the present endplate, have been taking data. The spatial resolution has been studied in detail. This confirms the technology potential of the resistive anode for a Micromegas TPC.

To save space and equip the endplate of our TPC prototype with seven modules at the same time, a miniaturization of the front-end electronics and a backend readout system with multi-module capabilities have been developed without protection circuit. The new integrated electronics has been tested in the beam. Thanks to the resistive layer, the new electronics could not be damaged by discharges that normally occur in common Micromegas detectors. It can be flat at the back of the detector module. The material budget is homogeneous and less than 25% of a radiation length, which meets the requirement of the endplate of the ILD-TPC.

To calibrate the characteristic of the modules, a test-bench using a  $^{55}\text{Fe}$  source has been built and was operated in a clean room at CERN. The  $^{55}\text{Fe}$  source is held in an aluminum collimation tube and fixed on a set of two mechanical arms, which moves the source for the scanning of the pads. The energy resolution, gain, and stability with time have been studied on a module-by-module basis.

Analysis software based on a standard ILC analysis package, MarlinTPC, has been developed. It can deal with multiple readout modules and fit multiple tracks in one event, using a Kalman-filter algorithm. This makes codes and results more exchangeable and comparable among different research groups (Micromegas, Asian GEMs, German GEMs and pixels).

Distortions have been observed without or with magnetic field at the level of 600-700  $\mu\text{m}$  at most near the edge of the modules. To better understand the E effect and  $E \times B$  effect requires further simulation studies. Their detailed study will allow these effects to be corrected and the design to be improved to minimize them.

A 2-phase  $\text{CO}_2$  circulation cooling system is presently under test at NIKHEF and will be installed at DESY. A problem in the robustness of the connection of the pads to electronics has shown up and will be solved. These are expected to be available for the next beam test foreseen at DESY early 2014.

In the future, a new field cage with improved fabrication will be built, two-track separation will be studied, and the energy loss ( $dE/dx$ ) could be tested at CERN using high-energy hadron test beam.

## Chapter 8

# **Other Micromegas TPC application: imaging by neutrons**



Radiography by neutron is of interest as the interaction cross section is large for light materials. This allows hydrocarbons to be seen through a metal container for instance. In view of its insensitivity to gamma-rays under certain conditions, neutron detectors based on the Micromegas detector concept with a converter layer were also developed and studied in the last ten years [65][66][67]. The detailed physics process of the neutron Micromegas detector using polyethylene as the converter layer has been simulated by the group of Lanzhou University [68][69]. The Fast Neutron Imaging (FNI) detector was developed under a collaboration between Lanzhou University and CEA-Saclay. It is based on the Bulk Micromegas technology. The polyethylene is chosen as the converter layer of the FNI detector. The characteristics of the detector were studied using X-rays and neutrons data taken in China. Experimental results are reported here.

## 1. Detector description

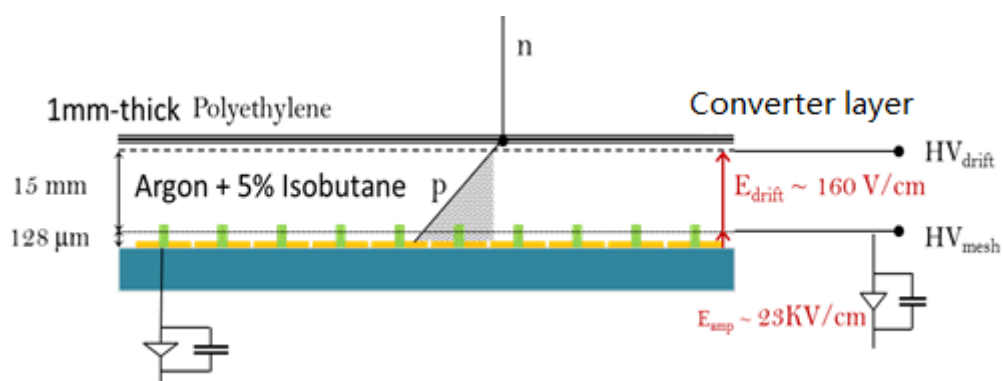


Figure 8-1. Sketch of the FNI detector.



Figure 8-2. The PCB of the neutron detector (sensitive area: 57.4 mm × 88.6 mm).

The mechanics of the FNI detector is sketched in figure 8-1. The bulk Micromegas technology is used. A 1 mm thick aluminized polyethylene layer is formed between 2 layers (0.5  $\mu\text{m}$  thick) of Al as the conversion layer and the cathode. The 15 mm drift gap and 128  $\mu\text{m}$  amplification gap are separated by the micromesh. The readout PCB is composed of 1728 ( $36 \times 48$ ) pads as shown in figure 8-2. The pad size is 1.75 mm  $\times$  1.50 mm and the sensitive area of the detector is 57.4 mm  $\times$  88.6 mm. By setting the proper voltage, a 160 V/cm electric field in the drift gap and a 23 kV/cm electric field in the amplification gap are established. When a neutron enters the detector, it will bounce a proton in the conversion layer. If the energy of the recoil proton is high enough, it will fly into the drift gap and induce the gas ionization. Under the influence of the electric field, the ionization electrons pass through the micromesh and trigger an avalanche in the amplification gap. The proton track can be obtained by the collection of signals. The starting position of the track is approximately the position of the incident neutron. During the test, the AFTER-based electronics, developed for T2K experiment, was used as the readout electronics [70]. It has 1728 channels and is composed of 6 Front-End Cards (FEC) read out by a Front-End Mezzanine (FEM). The electronics has been described in detail in Chapter 3.

## 2. The characteristics measurements

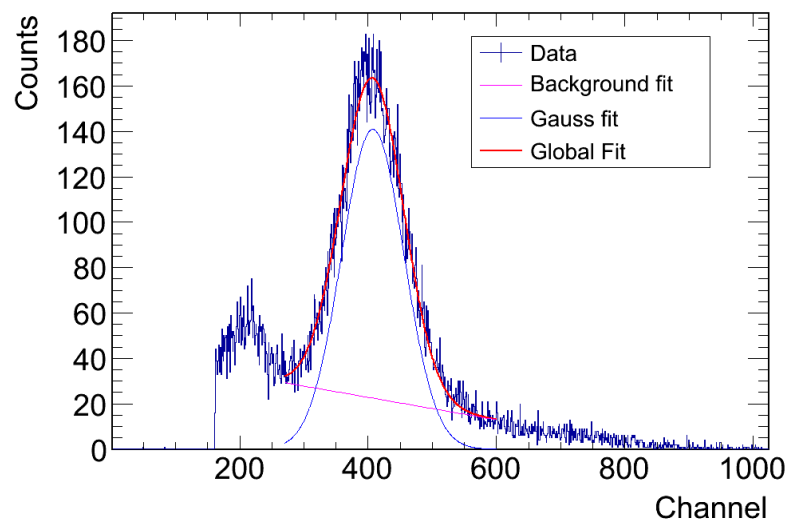


Figure 8-3. Energy resolution of the  $^{55}\text{Fe}$  spectrum.

To study the characteristics of the detector, it was tested with 5.9 keV X-rays from a  $^{55}\text{Fe}$  source. The gaseous mixture was 95% Ar+5% isobutane at atmospheric pressure and room temperature. The signals were read out from the mesh by a charge preamplifier linked to an

amplifier/shaper. A multi-channel analyzer was used for spectrum recording. The energy resolution was measured. A 12% r.m.s. at 5.9 keV and a well separated escape peak at 3 keV were obtained as shown in figure 8-3. Compared to the best energy resolution (7% r.m.s.) obtained from a bulk Micromegas detector, this value is not very good due to the detector's capacitance and the noise. The gas gain curve as a function of the mesh voltage is obtained by fitting a Gaussian function to the  $^{55}\text{Fe}$  spectrum and shown in figure 8-4. The voltage of the mesh was increased during the test and the drift electric field was kept at the same value. The gain of the detector reaches  $10^4$ .

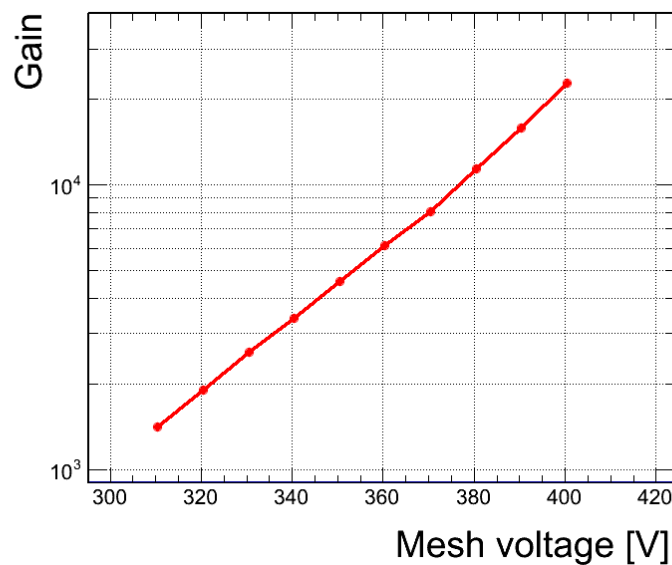


Figure 8-4. Gas gain as a function of the mesh voltage in 95% Ar+5% isobutane.

### 3. The neutron tests

The detector took data using an  $^{241}\text{Am}-^9\text{Be}$  neutron source. For the track of a particle, a cluster is found using the signal collected on the PCB and the difference of pads' time ( $\Delta T$ ) in one cluster is obtained. According to the simulation analysis, the recoiling proton liberates electrons along its trajectory in the whole drift gap. Using a method of time coincidence, the starting point of the proton track is derived. This position is counted as the position of the neutron. In this way, the spatial resolution is expected to be better than the pad size.

#### 3.1. $^{241}\text{Am}-^9\text{Be}$ neutron source

To obtain the best efficiency for the detection of the proton induced by the neutron in a polyethylene layer, the conversion efficiency was studied first for different thicknesses of the polyethylene layer using a Geant4 simulation. The  $^{241}\text{Am}-^9\text{Be}$  source spectrum was taken



according to the ISO 8529 standard as shown in figure 8-5 [71]. The converter efficiency as a function of the thickness of polyethylene in figure 8-6 shows that around several mm thickness polyethylene gives the best conversion efficiency. If the thickness of the converter foil is more than 1 cm, the converter efficiency will decrease with the thickness of polyethylene. In our test, a 1 mm thick aluminized polyethylene was chosen as the converter layer.

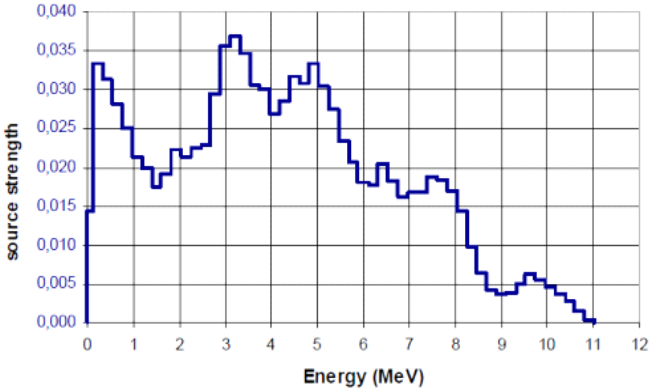


Figure 8-5.  $^{241}\text{Am}$ - $^9\text{Be}$  source spectrum according to ISO 8529 standard.

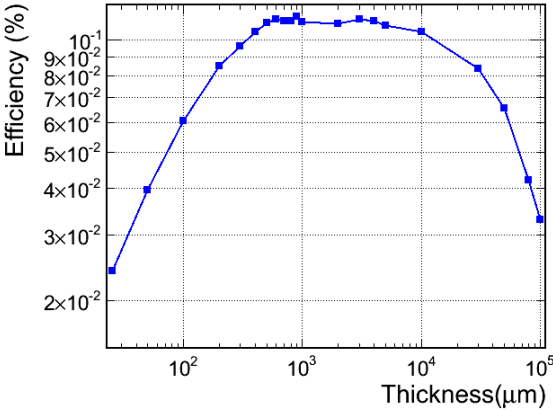


Figure 8-6. The conversion efficiency as a function of the thickness of the polyethylene  $([\text{C}_2\text{H}_4]_n)$  layer simulated by Geant4.

### 3.2. Neutron imaging

Figure 8-7 shows the setup for the neutron imaging. The neutron detector was put vertically to face the neutron source. The tested mask was put in front of the cathode of the detector, and between the FNI detector and the neutron source. Different masks with different letters as shown in figure 8-8 were tested respectively. According to the simulation, the proton recoiled

by neutron will deposit its energy along its track in all 15 mm drift space. The electrons which have the maximum drift time in one cluster are ionized near the converter foil and its position is nearly considered as the position of the neutron. Using the time information of the cluster, the neutron imaging is reconstructed.

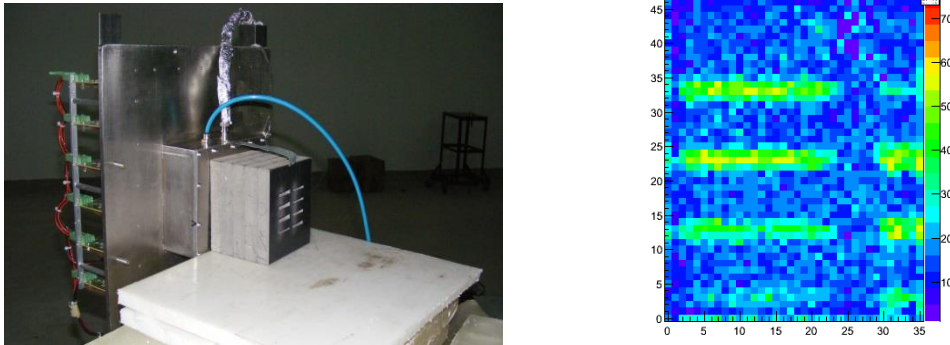


Figure 8-7. Left: the setup of the neutron imaging test. Right: the corresponding imaging.



Figure 8-8. Polyethylene masks used for the neutron imaging.

To obtain the imaging, firstly the pads signals are extracted. The maximum ADC and the corresponding time bin are extracted as the amplitude and time of the pad. Then, clusters in one event are studied. If the pads which have signal are neighbor in row or column, they are considered as one cluster. The times in one cluster are compared and the maximum time is drawn. Figure 8-9 shows a typical neutron event with the time information. In this cluster, the maximum drift time is recorded at bin 226, which gives the time of arrival of the ionization electron near the cathode of the detector. The position of the pad which has the maximum time in one cluster approximates the position of the neutron. The maximum time-difference in one cluster represents the drift time of electrons which come from near the converter foil as shown in figure 8-10.

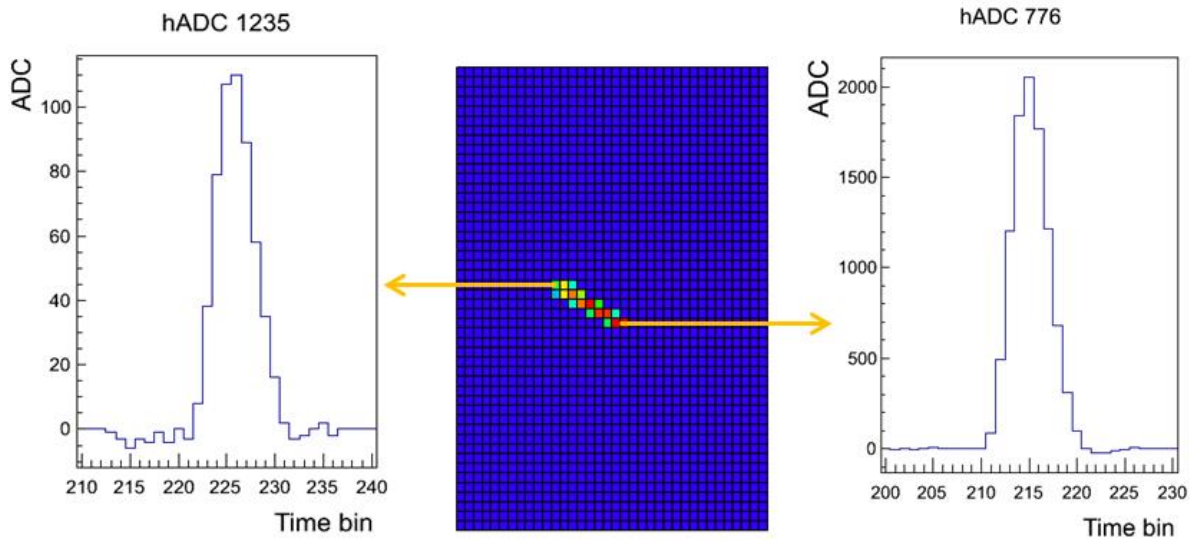


Figure 8-9. A typical neutron event with the maximum time and the minimum time in this cluster.

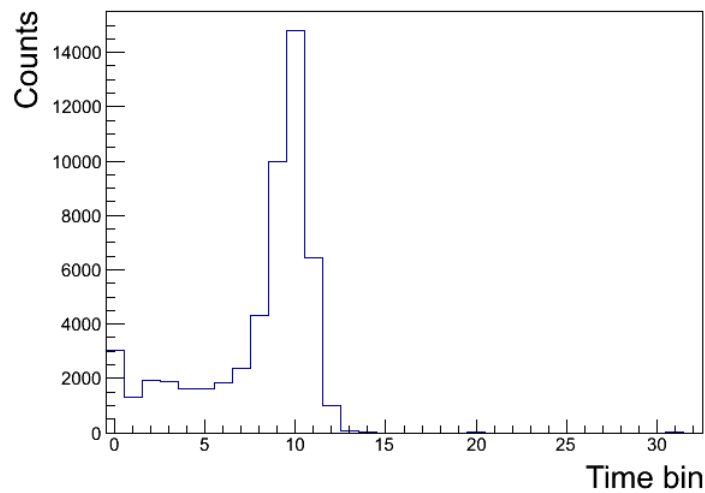


Figure 8-10. Maximum time-difference in one cluster in 40 ns time bin.

To check the resolution of the detector, the detector was tested with a 10 cm thickness polyethylene mask carved with different width slots as shown in the figure 8-7 (left). The corresponding imaging is shown in the figure 8-7 (right). In the left side of the imaging, four slots imaging correspond to the slots with 2.5 mm, 3 mm, 3.5 mm, and 4 mm width in the mask respectively. From the reconstructed imaging result, the slot with 3 mm width is already seen.

Figure 8-11 shows the imaging tested with an 8 cm thickness polyethylene mask carved with 4-4.5mm width letters “CEA” or “LZU”. Figure 8-11 (a) is the imaging integrating the ADC

of all events in one pad. Figure 8-11 (b) shows the imaging reconstructed using the time information. Only the positions of the pad which has the maximum time in one cluster are filled in the histogram. The imaging is greatly improved as shown in Figure 8-11 (b).

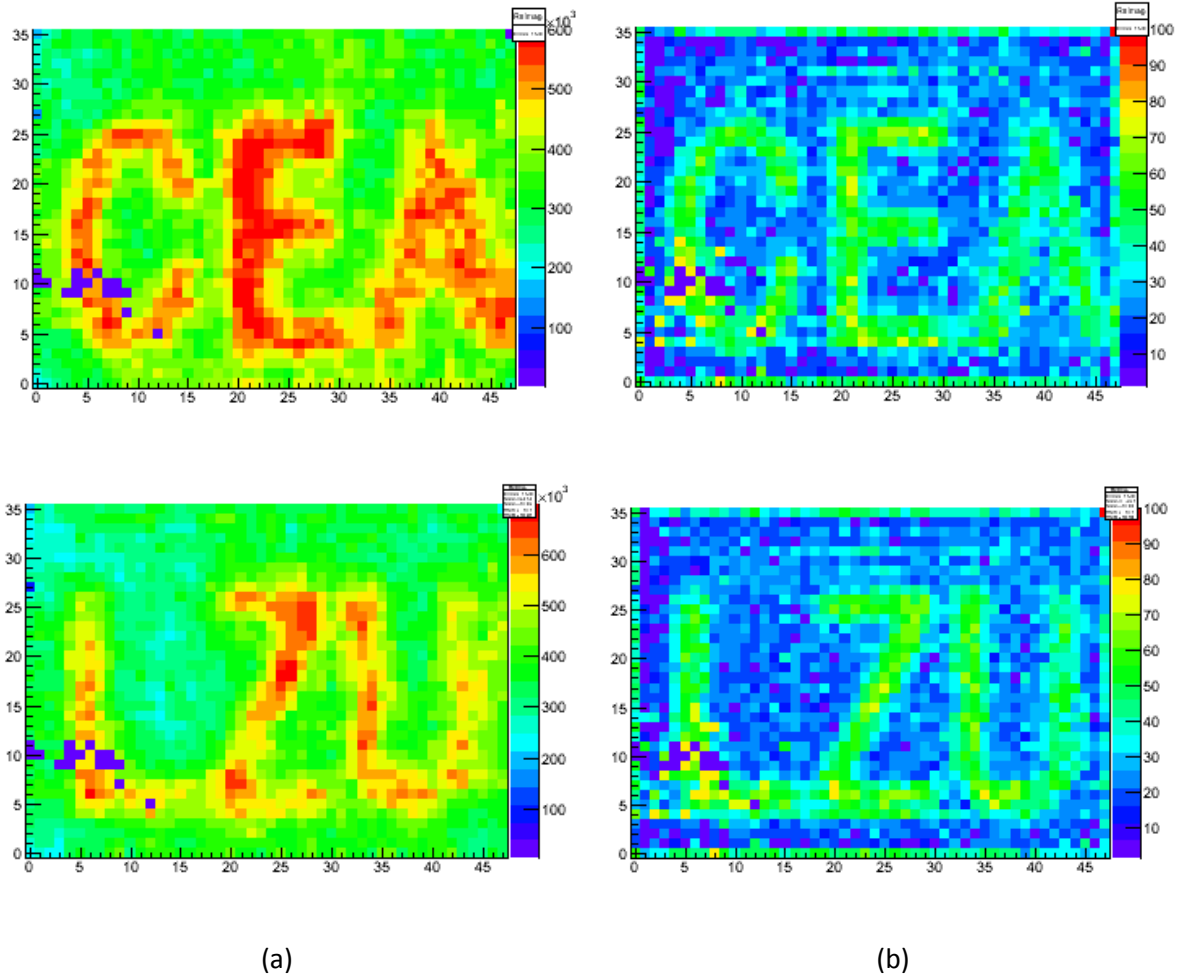


Figure 8-11. Neutron imaging. (a) Integrating the ADC of all events in one pad. (b) Reconstructed using the time information.

#### 4. Conclusion

Based on the bulk Micromegas technology, a fast neutron imaging detector has been built. The aluminized polyethylene was chosen as a converter layer due to its cheap price and as it gives rise to proton recoils only. Data have been taken using x-rays and neutrons. The detector worked well during the test. The analysis results show that the imaging is significantly improved by the time extrapolation technology.



APPENDIX

**Kalman Filter in ILCSOFT**



# 1. The principle of Kalman Filter

To describe the evolution of the measurement state  $\bar{a}_k$  at site ( $k$ ) from the previous measurement state  $\bar{a}_{k-1}$  at site ( $k-1$ ), the evolution equation is as follows:

$$\bar{a}_k = f_{k-1}(\bar{a}_{k-1}) + w_{k-1} \quad (0-1)$$

where  $\bar{a}_k$  is a state vector which means the state of the system at the site ( $k$ ), where the suffix  $k$  denotes the site at which the state is given and the bar over  $a$  means that it is the true value.  $f_{k-1}(\bar{a}_{k-1})$  is a state propagator in the ideal case that the random disturbance due to the process noise,  $w_{k-1}$ , were absent. If the process noise has no bias:  $\langle w_{k-1} \rangle = 0$ , a covariance can be given by

$$Q_{k-1} \equiv \langle w_{k-1} w_{k-1}^T \rangle \quad (0-2)$$

A measurement vector  $m_k$  is used to describe the observed values at site ( $k$ ). The relation between the measurement vector and the state vector can be written in the following form, named measurement equation:

$$m_k = h_k(\bar{a}_k) + \epsilon_k \quad (0-3)$$

where  $m_k$  is the measurement vector measured by a position sensitive detector, and  $h_k(\bar{a}_k)$  is the projector, which is the true measurement vector if the random error due to the measurement noise,  $\epsilon_k$ , were absent. If the random measurement noise has no bias:  $\langle \epsilon_k \rangle = 0$ , a covariance can be given by

$$V_k \equiv (G)^{-1} \equiv \langle \epsilon_k \epsilon_k^T \rangle \quad (0-4)$$

To effectively estimate the state of the system using the measurement vectors, the following processes need to be done.

- Prediction:

Before the observation at site ( $k$ ) is done, the random process noise for this site is not known. To extrapolate the state vector from the site ( $k-1$ ) to the site ( $k$ ), only the first term of equation 0-1 is used:

$$a_k^{k-1} = f_{k-1}(a_{k-1}^{k-1}) = f_{k-1}(a_{k-1}) \quad (0-5)$$

By definition, the covariance matrix (error matrix) for  $a_{k-1} \equiv a_{k-1}^{k-1}$  is given by



$$C_{k-1} = C_{k-1}^{k-1} \equiv \langle (a_{k-1} - \bar{a}_{k-1})(a_{k-1} - \bar{a}_{k-1})^T \rangle \quad (0-6)$$

The covariance matrix for the predicted state vector ( $a_k^{k-1}$ ) is expressed as

$$C_k^{k-1} = F_{k-1} C_{k-1} F_{k-1}^T + Q_{k-1} \quad (0-7)$$

where  $F_{k-1} \equiv \frac{\partial f_{k-1}}{\partial a_{k-1}}$  is called a propagator matrix.

- Filtering:

This is to get the optimal estimate of the state vector at current site ( $k$ ) based on the information of all sites up to site ( $k$ ). The goal here is to formulate this as a recurrence formula.

The filtered state vector ( $a_k$ ) at site ( $k$ ) is

$$a_k = a_k^{k-1} + K_k(m_k - h_k(a_k^{k-1})) \quad (0-8)$$

The corresponding filtered covariance matrix is

$$C_k = [(C_k^{k-1})^{-1} + H_k^T G_k H_k]^{-1} \quad (0-9)$$

where  $H_k = \left( \frac{\partial h_k}{\partial a_k^{k-1}} \right)$ , is called a projector matrix, which is the derivative of the projector with respect to the track parameter vector.

$K_k = C_k^{k-1} H_k^T (V_k + H_k C_k^{k-1} H_k^T)^{-1} = C_k H_k^T G_k$ , is called Kalman Gain Matrix and represents how the state vector at site ( $k$ ) is improved by the new measurement vector at site ( $k$ ).

- Smoothing:

After more information at subsequent sites: ( $k+1$ ) to ( $n$ ) are collected, the state vector at site ( $k$ ) can be re-evaluated and further improved. This process is called smoothing. The goal here is to work out an inverse recurrence formula that gives the smoothed state vector at site ( $k$ ) based on the smoothed state vector at site ( $k+1$ ) and the filtered state vectors at sites ( $k$ ) and ( $k+1$ ). The smoothed state vector at site ( $k$ ) is

$$\begin{cases} a_k^n = a_k + A_k(a_{k+1}^n - a_{k+1}^k) \\ A_k = C_k F_k^T (C_{k+1}^k)^{-1} \end{cases} \quad (0-10)$$

The smoothed covariance matrix for  $a_k^n$  is

$$C_k^n = C_k + A_k (C_{k+1}^n + C_{k+1}^k) A_k^T \quad (0-11)$$

- Inverse Kalman Filter:

In the case if we want to exclude a site in the middle, like site ( $k$ ), after the filtering process from site (1) to site ( $n$ ) and smoothing process from site ( $n$ ) to site (1) performed, the processor named inverse Kalman Filter is called to realize this function. Of course, we can always redo Kalman Filter without using the information of site ( $k$ ). But a better way is that makes full use of the previous results with site ( $k$ ). The following formulae for the inverse Kalman Filter are used to realize this.

$$\begin{aligned}
 a_k^{n*} &= a_k^n + K_k^{n*}(m_k - h_k(a_k^n)) \\
 K_k^{n*} &= C_k^n H_k^T (-V_k + H_k C_k^n H_k^T)^{-1} \\
 C_k^{n*} &= (1 - K_k^{n*} H_k) C_k^n = [(C_k^n)^{-1} - H_k^T G_k H_k]^{-1}
 \end{aligned} \tag{0-12}$$

Compared with the formulae of the processor of Filtering, we can see that the difference is the sign in front of  $G_k$  or  $V_k$ , which indicates the negative weight due to the eliminated information of site ( $k$ ).

Here, only the final formulae for each processor are enumerated. For the mathematic formula derivation in detail, the further information can be found in [59].

## 2. Kalman Filter in ILC SOFT

Since the data were taking using 5 GeV electron beam without magnetic field or with 1 T magnetic field in our beam test. The trajectory of the particle is a straight line or a helix. If the charged particle passes a uniform magnetic field and the direction of the magnetic field is along the  $z$ -axis, the track of this particle can be approximated by a helix [59]:

$$\begin{cases}
 x = x_0 + d_\rho \cos \phi_0 + \frac{\alpha}{\kappa} (\cos \phi_0 - \cos(\phi_0 + \phi)) \\
 y = y_0 + d_\rho \sin \phi_0 + \frac{\alpha}{\kappa} (\sin \phi_0 - \sin(\phi_0 + \phi)) \\
 z = z_0 + d_z - \frac{\alpha}{\kappa} \tan(\lambda \cdot \phi)
 \end{cases} \tag{0-13}$$

where  $\mathbf{x}_0 = (x_0, y_0, z_0)^T$  represents a measurement site ( $k$ ) and  $\phi$  is the deflection angle measured from this site. At a given site, the helix can be expressed by a parameter vector  $\mathbf{a}_k = (d_\rho, \phi_0, \kappa, d_z, \tan \lambda)^T$ . Here these five parameters are:

$$\left\{ \begin{array}{l} d_\rho : \text{the distance between the helix and the site in the x-y plane} \\ \phi_0 : \text{the azimuthal angle of the site with respect to the center of the helix} \\ \kappa : \equiv Q/p_t \text{ the charge in units of the proton/the transver semomentum} \\ d_z : \text{the distance between the helix and the site in the z direction} \\ \tan\lambda : \text{the dip angle between the helix to the x-y plane} \end{array} \right.$$

Figure 0-1 shows the helix parameters. The signed radius  $\rho$  of the helix is related to the parameter  $\kappa$  through  $\rho = \alpha/\kappa$ , here  $\alpha$  is a constant given by  $\alpha \equiv 1/cB$ .  $C$  is the speed of light and  $B$  is the magnetic field.

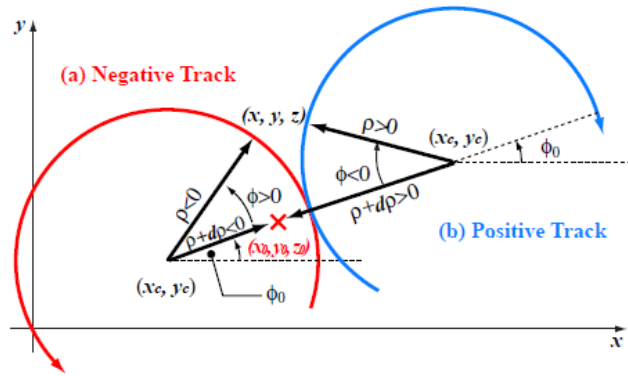


Figure 0-1. Geometric interpretation of the helix parameters for (a) negatively and (b) positively charged tracks [59].

To fit the track of the charged particle, the Kalman Filter is already realized as one of the packages framework of ILCSoft now. It includes KalDet and KalTest two packages and developed independence of MarlinTPC. The KalTest is a root-based package and includes basic libraries for track fitting using Kalman Filter technique [72]. It provides three basic classes: KalLib, KalTrackLib and GeomLib. The KalLib provides a library of generic abstract base classes that implement the genetic algorithm of the Kalman Filter. The KalTrackLib provides a Kalman-filter-based track fitter library for tracking fitting purpose and is independent of any particular track model or coordinate system. The GeomLib is a geometry library that provides the track models and surfaces. To implement these libraries in the KalTest, at last the information of measurement layer, the geometry of the detector, and the hit coordinate vector need to be defined. The KalDet provides these user-defined classes, which gives the geometry components and material of the detector description for KalTest. For the specific application required by LC-TPC, a directory named lctpc in KalTest provides these required classes, named EXTTPCKalDetector, EXTTPCMeasLayer, and EXTTPCHit respectively. The EXTTPCKalDetector class gives the detector description and the

corresponding geometry parameters of the detector which are defined in a GEAR xml file outside the KalDet package. This class gives the user-defined measurement layer with particular shape and coordinate system, and the material distributions. The EXTPCMeasLayer class describes a measurement layer that multiple inherits from an abstract measurement layer class defined in KalTrackLib and a shape class defined in GeomLib. The EXTPCHit class provides a measurement vector as defined by EXTPCMeasLayer.



# Bibliography

- 
- 1 <http://www.lhc.ac.uk/>
  - 2 <http://cms.web.cern.ch/>
  - 3 <http://atlas.web.cern.ch/>
  - 4 "CERN experiments observe particle consistent with long-sought Higgs boson". CERN. 4 July 2012. Retrieved 4 July 2012.
  - 5 Howard Baer *et al.*, "Physics at the International Linear Collider" Physics Chapter of the ILC Detailed Baseline Design Report (2013)
  - 6 G.Weiglein *et al.*, "Physics Interplay of the LHC and the ILC" arXiv:hep-ph/0410364, 2004
  - 7 M.Thomson, "ILD Detector Optimisation", ILD-UK, Cambridge, 21/9/2007
  - 8 A.Koya *et al.*, "Linear Collider for TeV Physics", KEK-Report-2003-7, 2003
  - 9 T.Behnke, (ed.) *et al.*, The International Linear Collider Technical Design Report. Volume 1: Executive Summary (2013).
  - 10 A.Vogel, Beam-induced backgrounds in detectors at the ILC, PhD these, Hamburg University, 2008, DESY-THESIS-2008-036
  - 11 G.A.Moortgat-Pick *et al.*, The role of polarized positrons and electrons in revealing fundamental interactions at the linear collider, Phys. Rept. 460, 131–243 (2008), hep-ph/0507011.
  - 12 International Large Detector web site (LOI), ILD Concept Group: Letter of Intent, (2009), <http://www.ilcild.org/documents/ild-letter-of-intent/LOI.pdf/view>.
  - 13 ILD Concept Group "INTERNATIONAL LARGE DETECTOR: DBD" 2012
  - 14 K.Abe *et al.* GLD Concept Study Group. arXiv:physics/0607154, 2006.
  - 15 D.Kisielewska *et al.* LDC Working Group. 2006, <http://www.ilcldc.org/documents/dod/>.
  - 16 International Large Detector web site (LOI), ILD Concept Group: Letter of Intent, (2009), <http://www.ilcild.org/documents/ild-letter-of-intent/LOI.pdf/view>.
  - 17 R.L.Gluckstern, Uncertainties in track momentum and direction, due to multiple scattering and measurement errors, Nucl. Instrum. Meth. 24, 381–389 (1963).
  - 18 Report to the Desy RPC 2010- The LCTPC Collaboration- ILC-NOTE-2012-063
  - 19 D.Nygren, PEP note 144 (1974).
  - 20 Blum W., Riegler W. and Rolandi L. 2008 "Particle Detection with Drift Chambers" 2nd edit (Berlin: Springer)
  - 21 C.K.Hargrove "The Time Projection Chamber (TPC) an overview" 1984
  - 22 H.J.Hilke "Time projection chamber" Rep. Prog. Phys.73 (2010) 116201 (36pp)

- 
- 23 T.Lohse and W.Witzeling, “The Time projection chamber”, Adv. Ser. Direct. High Energy Phys. 9, 81–155 (1992).
- 24 Y.Giomataris *et al.* “MICROMEAS: a high-granularity position-sensitive gaseous detector for high particle-flux environments” Nucl. Instr. and Meth. A 376 (1996) 29
- 25 I.Giomataris “MICROMEAS: results and prospects”, ICFA Instrumentation Bulletin, Volume 19, Fall 1999.
- 26 I.Giomataris *et al.* “Micromegas in a bulk”. NIM A, 560:405–408, 2006. 45, 46
- 27 M.S.Dixit, J. Dubeau, J.-P.Martin, and K.Sachs, “Position sensing from charge dispersion in micro-pattern gas detectors with a resistive anode”, Nuclear Instruments and Methods in Physics Research A518 (2004) 721.
- 28 M.S.Dixit “Charge dispersion MPGD Readout & ILC-TPC Prototype Test Beam Studies” TPC Applications Workshop Berkeley 7 April, 2006
- 29 Memorandum of Agreement on the Formation of the LCTPC Collaboration, October 2007, <http://www.lctpc.org/e9/e56939/>
- 30 <http://www.lctpc.org/>
- 31 <http://www.eudet.org/>
- 32 S.Biagi <http://magboltz.web.cern.ch/magboltz/>
- 33 T.Chaminade *et al.*, “A High-tech Trigger hodoscope with MPPC and Peltier devices” TIPP Poster 2009
- 34 [http://www.lepp.cornell.edu/~dpp/linear\\_collider/LargePrototypeDrawings2008.htm](http://www.lepp.cornell.edu/~dpp/linear_collider/LargePrototypeDrawings2008.htm)
- 35 D.Calvet “T2K TPC Read-out Electronics Digital Front-end Mezzanine Card Design Notes” 2007
- 36 P.Baron “AFTER user manual” 2006
- 37 E.Delagnes *et al.* “AFTER, an ASIC for the Readout of the Large T2K Time Projection Chambers”
- 38 D.Attie *et al.*, “The readout electronics of the Micromegas-based large time projection chamber prototype for the international linear collider” Real Time Conference (RT), 2012 18th IEEE-NPSS
- 39 M.Gupta. “Calculation of radiation length in materials” PH-EP-Tech-Note-2010-013
- 40 <http://pdg.lbl.gov/2012/AtomicNuclearProperties/>
- 41 S. Eidelman et al. Particle Data Group, Review of particle physics, Phys. Lett. B 592 (2004)
- 42 Report to the Desy RPC 2010- The LCTPC Collaboration- ILC-NOTE-2012-063
- 43 Personal communication with P.Colas.
- 44 P.Colas *et al.*, “Ion backflow in the Micromegas TPC for the future linear collider” Nucl. Instr. and Meth. A 535.1 (2004): 226-230.
- 45 M.Chefdeville’s thesis “Development of Micromegas-like gaseous detectors using a pixel readout chip as collecting anode” 2009
- 46 M.S.Dixit’s talk. “Development of high resolution Micro-Pattern Gas Detectors (MPGD) with wide readout pads”, Kolkata, 2010

- 
- 47 N.Shiell “A New Analysis Technique to Improve Spatial Resolution for a Resistive Anode Time Projection Chamber” Msc thesis 2012
- 48 M.Kobayashi *et al.* “Cosmic ray tests of a GEM-based TPC prototype operated in Ar–CF<sub>4</sub>–isobutane gas mixtures” Nucl. Instr. and Meth. A 641 (2011) 37–47
- 49 [http://ilcsoft.desy.de/portal/software\\_packages/lcio/](http://ilcsoft.desy.de/portal/software_packages/lcio/)
- 50 [http://ilcsoft.desy.de/portal/software\\_packages/gear/index\\_eng.html](http://ilcsoft.desy.de/portal/software_packages/gear/index_eng.html)
- 51 Dan Petersen, Technical Drawings of the LP1 End Plate  
[http://www.lepp.cornell.edu/~dpp/linear\\_collider/images/LargePrototype/20080312-6080-102-Endplate-drawing.pdf](http://www.lepp.cornell.edu/~dpp/linear_collider/images/LargePrototype/20080312-6080-102-Endplate-drawing.pdf)
- 52 [http://ilcsoft.desy.de/portal/software\\_packages/marlin/](http://ilcsoft.desy.de/portal/software_packages/marlin/)
- 53 F.Gaede. Marlin and LCCD: Software tools for the ILC. Nucl. Instr. and Meth. A559:177–180, 2006.
- 54 [http://ilcsoft.desy.de/portal/software\\_packages/marlintpc/](http://ilcsoft.desy.de/portal/software_packages/marlintpc/)
- 55 J.Abernathy *et al.*, “MarlinTPC: A Marlin based common TPC software framework for the LC-TPC collaboration” arXiv:0709.0790v1 [physics.ins-det]
- 56 R.E.Kalman, J.Basic Eng. 82 (1961) 34.
- 57 R.Frühwirth, Nucl. Instr. and Meth. A262 (1987) 444.
- 58 E.J.Wolin and L.L.Ho, Nucl. Instr. and Meth. A219 (1993) 493.
- 59 K.Fujii, “Extended Kalman Filter” Reference Manual.
- 60 <http://heed.web.cern.ch/heed/>
- 61 Personal communication with H.Schindler.
- 62 T.Matsuda *et al.*, “LP1 Beam Test with Three Asian GEM Modules”. EUDET Annual Meeting 2010, DESY
- 63 D.C.Arogancia *et al.*, “Study in a beam test of the resolution of a Micromegas TPC with standard readout pads” Nucl. Instr. and Meth. A **602** (2009) 403-414
- 64 R.Yonamine’s reports in the 8<sup>th</sup> and 9<sup>th</sup> LCTPC Analysis meeting.
- 65 S.Andriamonje *et al.*, Nucl. Intsr. and Meth. A 481(2002) 120.
- 66 M.Houry *et al.*, Nucl. Intsr. and Meth. A 557(2006) 648.
- 67 J.Pancin *et al.*, Nucl. Intsr. and Meth. A 524(2004) 102.
- 68 Y.Zhang *et al.*, Chinese Physics C (January 2009), 33 (1), pg. 42-46
- 69 W.Wang *et al.*, Chinese Physics C (January 2009), 33 (2), 110
- 70 P.Baron *et al.*, IEEE Transactions on Nuclear Science, Vol. 55, No. 3, June 2008
- 71 INTERNATIONAL STANDARD ISO 8529. Reference neutron radiations – Part 1: Characteristic and methods of productions. International Standard ISO 8529-1 (2001).
- 72 <http://www-jlc.kek.jp/subg/offl/kaltest/>